Label-Free Optical Imaging and Quantitative Algorithms

to Assess Living Biological Systems

by

Leng-Chun Chen

A dissertation submitted in partial fulfillment
of the requirements for the degree of
Doctor of Philosophy
(Biomedical Engineering)
in The University of Michigan
2014

Doctoral Committee:

Professor Mary-Ann Mycek, Chair
Professor Stephen E. Feinberg
Professor Cynthia L. Marcelo
Professor Jan P. Stegemann

2014

Acknowledgements

First and foremost, I would like to thank my advisor, Professor Mary-Ann Mycek, for giving me the opportunity and freedom to conduct this novel research. I cannot complete this work without your insightful guidance and patient instruction. Your kindness and support encouraged me to complete my graduation studies. I owed many thanks to Professor Stephan Feinberg and Professor Cynthia Marcelo for your great support and precious comments on my research throughout these years. I would also like to thank my committee member Professor Jan Stegemann for your support on my work.

I thank all the people who have helped me to reach this point: Dr. Shiuhyang Kuo, Dr. H. Myra Kim, Dr. Ching-Wei Chang, Dr. Robert Wilson, Dr. William Lloyd, Dr. Malavika Chandra, Dr. Hiroko Kato, Dr. Roderick Kim, Dr. Jim Scheiman, Dr. Dennis Claflin, Sakib Elahi, Seung Yup Lee, Emma Salomonsson, Kehan Zhang, and Wenbo Wang. You all taught me and helped me a lot.

Lastly, I would like to express the deepest gratitude to my parents and my sisters for their love and support to let me chase my dream in the States. I would also like to thank all the friends in Ann Arbor for your company these years.

Thank you all from the deep of my heart.

Table of Contents

List of Figures

Figure 3.1 Histology scoring was performed by three expert readers. (a) Each of the 1 cm diameter EVPOMEs was assessed at Day 11 post-seeding. A section was sliced for H & E and the remainder of the EVPOME was used for the nonlinear optical molecular imaging. (b) Histology assessment based on the three criteria: (1) structural quality of the keratin layer, (2) cellular organization of the construct, and (3) health of the basal cell layer.

Figure 3.2 Measuring glucose consumption on day 11 for 5 batches in the thermal stress experiment.

Figure 3.3 Label-free nonlinear optical molecular imaging non-invasively interrogated a living EVPOME construct in three dimensions, measuring cross-sectional (middle) and *en-face* (right) images. Fluorescence intensity, fluorescence lifetime, and SHG microscopic images were acquired to quantitatively assess EVPOME viability (right). Three-dimensional spatially-localized optical measurements interrogated cellular metabolic function and spatial organization (steady-state imaging) as well as cellular microenvironment (FLIM).

Figure 3.4 Non-invasive optical characterization of tissue structure. Cross-sectional fluorescence images of EVPOME constructs from NAD(P)H (first row, cyan) and FAD (second row, green) channels with overlaid corresponding SHG images (blue) were compared to sample histology. Control and thermally-stressed (left columns) and metabolically-stressed (right columns)) EVPOMEs exhibit the layered tissue structure, consisting of a top keratin layer (K) ~10-20 μm thick, a middle living cellular layer (LC) ~20-30 μm thick, and a bottom dermal equivalent layer (DE) ~400 μm thick (a portion is shown). While fluorescence images quantitatively and non-invasively characterized EVPOME's layered structure, histology destroyed the EVPOME constructs. Scale bar: 50 μm.

Figure 3.5 *En-face* images were acquired to localize living cells from the living EVPOME. The movie introduces tissue constituents, keratin, NAD(P)H, FAD, and collagen, in each EVPOME layer. The endogenous biomolecules were employed for non-invasive, label-free quantification of tissue spatial organization, cellular metabolism, and tissue microenvironment.

Figure 3.6 Label-free optical spatial analysis characterized cellular organization in EVPOME constructs and reliably distinguished control from stressed constructs. (a) *En-face*, optically sectioned NAD(P)H images revealed cellular organization of the EVPOME constructs. In control constructs, differentiating cells (top) were characterized by large, loosely packed cells. Alternatively, basal layer cells (bottom) were characterized by small, closely packed cells. In thermally-stressed constructs, cell morphologies appeared disorganized in both layers. In metabolically-stressed constructs, EVPOMEs grew thin cellular layers (no distinct differentiating and basal layers). Therefore, only the basal layer image was acquired, which appeared disorganized. Scale bar: 20 μm. (b) Cellular organization was quantified by spatial analysis of optical images to extract a Hurst parameter (H). For both stressing experiments, the Hurst parameter significantly distinguished between stressed and control EVPOMEs. (*after employing the step (1) exclusion criteria, for 4 control with 11 H value differences and 3 thermally-

stressed batches with 8 H value differences, *P*-value = 0.004; **for 4 control with 12 H values and 3 metabolically-stressed batches with 10 H values, *P*-value <0.001)

Figure 3.7 Label-free optical redox ratio mapping characterized cellular metabolism in EVPOME constructs and reliably distinguished control from stressed constructs. (a) The top row shows cross-sectional EVPOME redox ratio maps; the bottom row shows *en-face* EVPOME redox ratio maps. Control constructs had a lower RR (deeper blue) than stressed constructs, indicative of viable and actively metabolizing cells. (K: keratin; LC: living cellular; DE: dermal equivalent) Scale bar: 25 μm. (b) An average RR for each image was extracted to quantify cellular viability of thermally-stressed (left) and metabolically-stressed (right) EVPOMEs. Control EVPOMEs had significantly lower RR than stressed EVPOMEs in both experiments. (For 5 batches with 30 control and 30 thermally-stressed images analyzed, **P*-value = 0.004; ** *P*-value <0.001).

Figure 3.8 Label-free fluorescence lifetime analysis successfully distinguished control from thermally-stressed EVPOMEs. (a) Representative *en-face,* optically sectioned NAD(P)H fluorescence intensity images and corresponding FLIM maps for an analyzed region-of-interest in control (left) and thermally-stressed (right) EVPOMEs. Larger mean fluorescence lifetime τ was observed in FLIM maps of thermally-stressed constructs relative to controls. (b) Mean of normalized fluorescence decays from regions-of-interest support the observation from FLIM maps that thermally-stressed constructs exhibited greater mean NAD(P)H fluorescence lifetimes than controls. Error bars represent s.e.m. (c) NAD(P)H fluorescence decays measured from constructs were best fit to a two-exponential decay model. Model fits revealed that the percent contribution of τ_1 (attributed to bound NAD(P)H) to the measured fluorescence decay was significantly higher in thermally-stressed EVPOMEs than in controls (for 5 batches with 58 control and 33 thermally-stressed regions analyzed, *P*-value < 0.001).

Figure 3.9 Phasor plot distinguished between control and thermally-stressed cells in EVPOMEs (for 5 batches with 31 control and 18 thermally-stressed FLIM images analyzed, *P*-value of the s coordinate = 0.048).

Figure 3.10 Histology scores assigned by a panel of blinded expert readers and percent glucose consumption measures did not reliably distinguish control and compromised EVPOMEs. Histology scores (with higher scores indicating greater perceived viability; 5 being the most viable) and glucose readings (percent error = 15%) compare control constructs to (a) thermally-stressed and (b) metabolically-stressed EVPOMEs prepared for the fluorescence intensity experiment, and (c) thermally-stressed EVPOMEs prepared for the fluorescence lifetime experiment (for 5 batches, *(a) *P*-value = 0.002; **(b) *P*-value < 0.001; (c) *P*-value = 0.03).

Figure 3.11 Non-invasive optical metrics obtained from label-free (a) redox ratio (RR) and (b) fluorescence lifetime (FLIM) images reliably identified all experimentally stressed tissue constructs, whereas histology scores assigned by a panel of blinded expert readers could not. (a) Mean redox ratio was compared to mean panel histology score for control (10 batches), thermally-stressed (5 batches), and metabolically-stressed (5 batches) EVPOME constructs. (b) FLIM analysis was compared to mean panel histology score for control (5 batches) and thermally-stressed (5 batches) EVPOME constructs. A FLIM

threshold (dashed black line) distinguished all 5 stressed constructs from the 5 controls. Error bars are standard deviation of all measurements from one EVPOME.

Figure 3.12 In the study for monitoring graft success after implantation, pre-implantation and post-implantation histology scores were compared. The plot shows that the pre-implantation viability monitoring successfully predicted the graft success (21 mice from 5 batches). Pre-implantation histology scores were rounded to the nearest integer. *n* is 6, 2, 0, 4, and 9 for the score of 1-5 respectively. Error bars are standard deviation of all EVPOMEs in the same category.

Figure 4.1 Tissue-engineered constructs were developed with varying viability and evaluated with histology, WST-1 assay, and label-free optical molecular imaging. A tissue construct of approximately 1 cm in diameter was sectioned and/or punch biopsied by histology and the WST-1 assay.

Figure 4.2 Tissue viability was assessed by quantitative histology scoring and WST-1 assay. The plot shows that the two metrics had a significant positive correlation (*P*-value = 0.015 for 5 batches with 16 tissue constructs).

Figure 4.3 Histology of two representative batches of tissue-engineered constructs: one in well-growing culture (left) and one in poorly-growing culture (right). The well-growing and the poorly-growing were defined by their control histology scores. A control score > 3 is defined as well-growing. A control score <= 3 is defined as poorly growing. Scale bar: 100 μm.

Figure 4.4 Ki-67 immunohistological staining was performed to characterize rapamycin-treated tissue-engineered construct's functionality for one batch in well-growing culture (left) and one batch in poorly-growing culture (right). Scale bar: 100 μm.

Figure 4.5 Label-free optical molecular imaging non-invasively characterized local engineered tissue viability, correlating to WST-1 assay. (a) The optical images show intracellular NAD(P)H and dermal equivalent fluorescence in cyan, and SHG collagen signals in blue. The RR maps excluded dermal equivalent signals, assessing cellular metabolism by quantifying the relative amount of NAD(P)H and FAD in cells. The rapa+c construct had lower RRs than the control construct, indicating its higher metabolic activity. (b) RR metrics significantly correlated to the WST-1 measures (*P*-value < 0.001 for 5 batches with 16 constructs and 88 optical measurements). The higher the WST-1 measure, the lower the RR metrics. Error bars show standard deviations.

Figure 4.6 Rapamycin treatment during the cell culture stage improved the tissue viability of poorly-growing batches measured by WST-1 (***P*-value < 0.001 for 2 batches with 4 measurements from the control and 3 measurement from the rapa+c constructs), optics (***P*-value < 0.001 for 3 batches with 23 measurements from the control and 24 measurements from the rapa+c constructs), and histology (**P*-value = 0.002 for 3 batches with 5 measurements from the control and 4 measurement from the rapa+c constructs) .

Figure 4.7 Histology and label-free optical molecular imaging characterized tissue morphology, demonstrating their advantage of spatial selectivity. (a) In a poorly-growing

culture, a control construct would have inhomogeneous tissue growth. (b) For the same batch, the rapa+c construct shows a well-growing tissue with intact layered structure in the histology section and in the optical images. Two optical channels were overlaid: the cyan channel for tissue fluorescence and the blue channel for dermal equivalent collagen. K: keratin layer; LC: living cellular layer; DE: dermal equivalent layer. Scale bars: 100 μm.

Figure 4.8 Optical metrics were compared to histology scores. The two metrics show a negative correlation (P-value = 0.007 for 10 batches with 30 tissue-engineered constructs and 166 optical measurements).

Figure 5.1 Phasor plots (a,b) without and (c) with error analysis characterized TCSPC FLIM images of (a) cells in standard culture and (b,c) engineered tissues.

Figure 5.2 Phasor error analysis of FLIM images acquired from (a) free NADH and (b) free FAD solutions. The bottom two panels are magnified from the top two panels.

Figure 5.3 (a) Single optical intensity images and the fast FLIM map cannot distinguish different tissue constituents. (b) Phasor error analysis distinguished tissue constituents in the engineered tissues with single-channel NAD(P)H FLIM image.

Figure 5.4 Phasor error analysis improved the FLIM assessments of cellular viability. (left) The analysis isolated collagen and keratin signals in the purple region. Signals lying outside the purple region (cyan region) are from cells. (right) 24 phasor points lying inside the purple region were averaged and plotted as extracellular matrix and 31 phasor points lying in the cyan region were averaged and plotted as cells. Error bars represent standard deviations.

Figure 5.5 Phasor error analysis distinguished between the control and the thermally-stressed constructs shown by (a) the phasor plot and the (b) box plots (**P-value < 0.001, For 5 batches with 30 control (blue) and 18 thermally-stressed for all the three parameters).

Figure 6.1 Time-gated FLIM concept of (left) separate gating ($g < \Delta t$), (center) continuous gating ($g = \Delta t$), and (right) overlapped gating ($g > \Delta t$).

Figure 6.2 Four-gate time-gated phasor plot map. The map demonstrates $g/\Delta t$ (reddish curves) & g/τ (underlying color map) of the single-exponential fluorescence decay model. The black semicircle indicates the phasor plot of the whole single-exponential fluorescence decays with no gating. Color bars are in the logarithm scale.

Figure 6.3 Artificial images mimicking the geometry that may be encountered in living-cell FLIM experiments. τ_1 values are in ns; α_1 values are in arbitrary unit. The table shows the parameter setting in the artificial image.

Figure 6.4 Time-gated phasor plots for the undenoised and the denoised FLIM images. The denoised phasor plots show decreased lifetime distributions.

Figure 6.5 Lifetime maps of the undenoised and denoised living cell FLIM images (values in ns). TV denoising was applied to each of the four intensity images before

lifetime reconstruction. The images were acquired with living HCT-116 cells stained with BCECF. Scale bar: 40 μm.

Figure 6.6 Phasor plots of the undenoised and the denoised time-gated FLIM images of living cells. The pseudocolored map of UWTV *w/gain* phasor plots shows intracellular lifetime variation.

List of Tables

Abstract

Non-perturbing tools that provide reliable, information-rich assessments of living biological systems can inform clinical practice and improve patient health. In this dissertation, we developed label-free nonlinear optical molecular imaging to provide spatially-resolved, non-perturbing, quantitative functional assessments of 1) living cell lines, 2) primary human cells, and 3) tissue-engineered constructs manufactured with primary cells. Quantitative analytic methods were developed to account for the high inter-patient variability in primary human cells freshly harvested from distinct donors.

The FDA strictly regulates the manufacture of tissue-engineered constructs, requiring assessment of product effectiveness and safety prior to release for patient treatment. We addressed this clinical need by developing quantitative methods to assess local tissue structure and biochemistry using label-free nonlinear optical molecular microscopy. Optical measures characterized morphologic and functional differences between controls and stressed constructs. Rigorous statistical analysis accounted for variability between patients. The technique reliably differentiated controls from stressed constructs from 10 batches/patients with P-value < 0.01. Further, the optical metrics strongly correlated with a standard WST-1 cell viability assay (P-values < 0.001 for 5 batches/patients). Unlike the standard methods, which are reliable but destructive, label-free optical assessments

are both non-invasive and reliable. Thus, such optical measures could serve as reliable manufacturing release criteria for cell-based tissue-engineered constructs prior to human implantation.

Label-free fluorescence lifetime imaging microscopy (FLIM) images consist of spatial and temporal information. The traditional method to analyze FLIM is iterative fitting, which is time-consuming and requires prior knowledge of the sample. Clinical practitioners require an analytical and simple-to-operate method to interpret FLIM images. Thus, extended phasor analysis algorithms were developed. The algorithms characterized tissue constituents with better differentiation (P-value < 0.001 for 5 batches/patients) than the standard fitting method (P-value = 0.048 for 5 batches/patients). In addition, time-gated FLIM with various gating schemes was analyzed with the developed phasor analysis algorithms to monitor intracellular lifetime variation. In summary, the developed algorithms could advance future FLIM applications in clinic.

Chapter 1 Introduction

1.1. Optical imaging

Optical imaging describes the light coming from the interrogated sample. It provides the information of the light with spatial resolution. Instrumentations were developed to achieve different goals. Instrumentation were developed to detect scattered light, for example, differential interference contrast (DIC) microscopy to enhance image contrast of thin samples with negligible absorption and only phase shifts to a transilluminating light, or optical coherence tomography (OCT) to achieve axial optical sectioning by temporal gating. Alternatively, instrumentations were developed to detect fluorescent light, which is a result of light absorption of the sample and light rerelease with a different energy from the sample. The instrumentation for fluorescence imaging, confocal microscopy, achieves lateral optical sectioning and provides the first 3D imaging by spatial gating. Nonlinear optical molecular microscopy is similar to confocal microscopy in practical implementation, which can achieve lateral optical sectioning and provide 3D imaging, but their fundamental concepts are different. Nonlinear optical molecular microscopy is based on the nonlinear effect rather than linear fluorescence excitation. As a consequence, the size of the 3D probe volume is governed solely by the microscope illumination optics, as opposed to confocal microscopy where it is governed by both the illumination and detection optics with the spatial gating [1].

The dissertation will mainly focus on nonlinear optical molecular microscopy including fluorescence intensity, fluorescence lifetime, and second harmonic generation imaging. In addition, the dissertation will introduce data analysis methods to interpret or visualize the biomedical meanings of the acquired optical images from living biological systems.

1.2. Fluorescence imaging of biological systems

A fluorescence image of biological systems, for example a tissue, is a spatially resolved map of detected tissue fluorescence across a specimen. The resulting 2D (or 3D) image of the tissue is comprised of individual "pixels" of fluorescence information in two (or three) spatial dimensions. Depending on the application, images can be acquired from the tissue surface (e.g., tumor margin detection or endoscopic imaging [2, 3]) or from the bulk sample (e.g., tomographic imaging [4, 5]). Fluorescence images can be acquired with macroscopic (e.g., wide-field whole animal imaging [6, 7]) or microscopic (e.g., imaging of individual cells [6, 8, 9]) spatial resolution. Image contrast can originate from endogenous (e.g., collagen, nicotinamide adenine dinucleotide (NADH), or flavin adenine dinucleotide (FAD [9, 10]) or exogenous (e.g., fluorescent dyes [11, 12]) molecular fluorophores. Fluorescence imaging can be applied to clinical applications (e.g., human [13]) or pre-clinical in small animals (e.g., murine tumor model [6]). Lastly, fluorescence images can spatially map fluorescence intensity [10] or fluorescence lifetime [14] information.

1.2.1. Instrumentation of fluorescence imaging

Fluorescence imaging systems comprise excitation light sources, light delivery and collection optics, filters, and technology for spatially resolved fluorescence detection [6]. Light sources for fluorescence excitation include broad-wavelength sources (e.g., UV or xenon arc lamps [15]) or narrow-wavelength sources (e.g., lasers or LEDs [10]). For a wide-field imaging system, the excitation beam is expanded before illuminating the sample [14] and the fluorescence is detected with a CCD camera [16]. For a point-scanning imaging system, a scanning unit (e.g., a set of mirrors on galvanometers) is employed to translate the focused excitation beam over the imaging field [10] and fluorescence emission is detected from each scanned point with a high-sensitivity photo-multiplier tube or avalanche photodiode to build-up the image pixel-by-pixel. Objective lenses can be used to enhance image resolution, especially at the microscopic level [17]. Thus, fluorescence technologies can be employed to acquire images at the single cell, tissue, or whole-body levels.

1.3. Nonlinear optical molecular microscopy of biological systems

Nonlinear optical molecular microscopy is a type of fluorescence imaging systems that has significant sectioning capabilities due to the nonlinear, two (or three)-photon absorption that is locally confined in space without the use of a spatial pinhole as compared to confocal microscopy [18, 19]. In two-photon absorption, two photons at λ_{MP} are absorbed simultaneously to mimic the energy of one absorbed photon at $\lambda_{MP}/2$. Advantages are that two-photon absorption occurs in a confined sample area, providing high spatial resolution at the focal point and little out-of-focus photobleaching.

Additionally, long-wavelength excitation photons at λ_{MP} cause deeper penetration depth, and they have less energy than single photon excitation, causing less damage to biological samples [20]. Moreover, nonlinear optical molecular microscopy has high sensitivity because all fluorescent photons originating from the sample are detected, including those scattered by turbid biological samples.

Nonlinear optical molecular imaging has advantages in imaging inhomogeneous living biological systems, such as layered tissues, requiring sectioning techniques that preferentially excite fluorophores in a single layer of the tissue, possibly at some preferred depth. Conventional applications to achieve sample sectioning include histology (destructive in nature) or other methods of sample staining. However, living tissues can be analyzed with nonlinear optical molecular microscopy in a nondestructive and non-harming manner. Nonlinear optical molecular microscopy has been employed to optically section thick biological samples down to thicknesses comparable to a cellular layer (a few micrometers) [21-23], thereby reducing the presence of background fluorescence from additional layers [24, 25].

As a complimentary technique for comparison with fluorescence imaging measurements, nonlinear optical molecular microscopy images fluorescence signals as well as second harmonic generation signals. Second harmonic generation (SHG) is a complementary technique. SHG is not a fluorescence process; it is a nonlinear optical process that occurs when two photons interact with a non-centrosymmetric material, combining the energy from the two photons and emitting a single photon with twice the energy, providing strong imaging contrast. The non-centrosymmetric molecular ordered structures include collagen [26], skeletal muscle myosin [27], cellulose [28], and silk [29]. Uses for SHG

signals in tissue-engineered constructs include confirming the presence, location, type, and approximate concentration of non-centrosymmetric material in a specimen.

1.4. Label-free nonlinear optical molecular microscopy to preserve living sample's functionality

The high sensitivity of nonlinear optical molecular microscopy makes it ideal for measuring endogenous tissue fluorophores. That is, the imaging technique is label-free (no chemical staining). Label-free optical imaging has broad biomedical applications because the technique preserves the living sample's functionality. The interrogated samples remain their functionality, which can then be studied with other assays or further, for clinical use. Nonlinear optical molecular microscopy provides high axial (optical sectioning) and lateral resolution, reduced out of focus photobleaching/photodamage, and is optimal for deep tissue imaging [30]. The optical imaging techniques in this dissertation will focus on label-free nonlinear optical molecular microscopy for functional imaging in living biological systems, including single cells and tissues.

1.4.1. Label-free nonlinear optical molecular microscopy to assess living biological systems

Nonlinear optical molecular microscopy has been employed to study layered epithelial tissues, which can contain multiple endogenous fluorophores such as keratin, melanin, NADH, flavoproteins, collagen, and elastin. The fluorescence properties of these

fluorophores have been previously reported [31] and widely studied as a means to noninvasively assess a sample via local endogenous variability [32].

Fluorescence properties of purified keratin under two-photon excitation as compared to one-photon excitation were characterized [33]. Multiphoton excitation was performed using a femtosecond Ti:sapphire laser operating in the 700–1000 nm range. The one-photon absorption spectrum of keratin has a maximum excitation wavelength of ~300 nm. Results show that fluorescence is measured with excitation wavelengths up to 900 nm, and fluorescence emission overlaps with the fluorescence spectra from collagen, NADH, and FAD. These results on keratin are of practical importance when studying human skin, as well as tissue-engineered constructs derived from keratinocytes.

Fluorescence of melanin under multiphoton excitation was characterized [18]. Melanin samples were studied with 800 nm two-photon excitation and were compared to 400 nm one-photon excitation. Similar to the previous measurements on keratin, measurements on melanin showed that the two-photon fluorescence spectra exhibited greater fluorescence at longer wavelengths. Measured synthetic melanin in dimethyl sulfoxide (DMSO) and excised healthy human skin tissue excited at the NIR tail of melanin absorption exhibited melanin fluorescence. Results showed that melanin fluorescence can be selectively excited with femtosecond pulses out of other fluorophores due to its resonant two-photon absorption, a property that may allow for melanin to be used as a means for identifying malignant changes in tissue or applied to tissue-engineered constructs to study similar destructive processes.

1.4.2. Label-free nonlinear optical molecular microscopy to assess cellular metabolism

Endogenous tissue fluorophores such as NAD(P)H, FAD, collagen, elastin, and keratin report on tissue microenvironment [34]. In particular, intracellular NAD(P)H and FAD molecules are involved in mitochondrial metabolic pathways [35]. Therefore, measurements of such endogenous fluorophores are label-free indicators of tissue metabolism.

It has been reported that NADH and FAD are natural biomarkers for cellular metabolism. In addition, a ratiometric method to evaluate cellular metabolism was developed with NADH and FAD fluorescence [35]. Therefore, characterizing the fluorescence properties of these endogenous fluorophores is the first step toward the accurate quantification of cellular viability. Nonlinear optical molecular imaging can optically resolve layered biological samples, allowing a thin cellular layer or even a monolayer of cells at a fixed depth within the sample to be investigated to assess sample viability and metabolic function, both on living tissue-engineered constructs and live tissue.

Two-photon excitation cross-sections of NAD(P)H, FAD, and LipDH were investigated [36]. Reported results showed that below 720 nm excitation, all the molecules have maximal absorptions in the experimental range. Above 800 nm excitation, there is little NAD(P)H absorption while the FAD and LipDH had peak absorption around 900 nm. Living cardiomyocytes were studied with two-photon excitation imaging at 750, 800, and 900 nm to monitor NADH (410–490 nm) and FAD fluorescence emission (510–650 nm), with each fluorophore predominating in its associated wavelength band, indicated by fluorescence changes induced by mitochondrial inhibitor and uncoupler. In addition, the

result of emission spectra of living cardiomyocytes further confirmed that at 750 nm excitation, the cellular spectrum resembled the NADH *in vitro* spectrum except for an enhancement at wavelengths > 490 nm, attributed to the flavoprotein fluorescence; at 900 nm excitation, the cellular spectrum peaked at about the same wavelength as the *in vitro* LipDH spectrum, but it was broader, which was attributed to the complexity of cellular flavoprotein components; at 800 nm excitation, the cellular spectrum resembled that at 900 nm excitation, which was attributed to NADH fluorescence leakage. The potential to assess both NADH and FAD, with highly characterized cellular spectra, shows promise as a future technique in tissue-engineered applications to monitor and quantify cellular metabolism.

1.5. Label-free nonlinear fluorescence lifetime imaging microscopy (FLIM)

Intensity-based measurements are vulnerable to artifacts such as variation in excitation source intensity, detector gain setting, optical loss in the optical path and/or sample, variation in sample fluorophores concentration, photobleaching, and microscope focusing. Further, fluorophores with similar excitation and emission spectra may be impossible to differentiate with steady-state fluorescence intensity imaging. Fluorophore lifetime is the property describing on average how rapidly an excited-state fluorophore decays. Fluorescence lifetime imaging microscopy (FLIM) is a method for measuring fluorophores lifetimes with microscopic spatial resolution, providing an additional source of contrast. FLIM can be performed with the label-free nonlinear optical molecular technique in a similar manner as described previously. The nonlinear, multiphoton excited fluorescence is acquired spatially (fluorescence intensity imaging) and temporally

(fluorescence lifetime imaging), which is most commonly acquired via the time-correlated single photon counting (TCSPC) technique [37].

The electronic excited stat lifetime of a fluorophore is the average time that an excited electron spends in the excited stat, and is typically on the order of picoseconds to nanoseconds in duration. Fluorophore lifetime is an intrinsic property of each individual fluorophores. It is known to be sensitive to the fluorophore's local environment and can reveal information on tissue pH, oxygenation, and temperature [38], while being generally insensitive to fluorescence intensity-based artifacts such as optical scattering from collagen fibers and optical absorption from blood [39, 40]. Relative fluorophore contributions can be resolved from time-resolved fluorescence measurements even if the steady-state spectra of the fluorophores overlap [40, 41].

1.5.1. Label-free nonlinear FLIM to assess cellular microenvironment

In vivo label-free measurements to monitor precancerous epithelia were performed on 22 hamster cheek pouches [42]. A significant decrease in the contribution and lifetime of protein-bound NADH was observed in both low- and high-grade epithelial precancers compared with normal epithelial tissues. In addition, a significant increase in the protein-bound FAD lifetime and a decrease in the contribution of protein-bound FAD were observed in high-grade precancers only. Increased intracellular variability in the NADH and FAD fluorescence lifetimes were observed in precancerous cells compared with normal cells. Label-free multiphoton-FLIM was also employed to characterize normal human epidermis at different skin sites and in patients of different ages [43], monitor metastasis and the tumor microenvironment in tissues [44], and monitor cell viability for

tissue engineering applications [45] via measurements of endogenous tissue fluorophores, demonstrating its potential for future clinical use.

1.6. Data analysis to interpret label-free fluorescence images

Label-free fluorescence signals, *e.g.* intracellular endogenous fluorescence from NAD(P)H and FAD, are usually dim because of their lower quantum yields as compared to exogenous dyes [46]. Thus, imaging setting should be properly designed and performed to increase acquired fluorescence signals while not harming the samples. In addition to controlling the hardware setting, developing image processing techniques is an alternative method to assist in enhancing the image resolution. Further, optical images acquired from biological systems only demonstrate their physical structures. Quantitative algorithms provide precise and objective interpretations of the functionality of the measured living biological systems.

1.6.1. Data analysis of optical intensity images

Image processing algorithms have been extensively studied. Computational algorithms developed mainly focus on increasing the signal-to-noise ratio and provide better pattern recognition of an acquired image. Other algorithms to characterize biological systems were also developed to quantitatively, thus objectively, interpret the acquired images. Tissue structure, such as epithelium layer thickness, cellular organization, cellular metabolism, collagen orientation can be quantified, thus providing biologists to visualize, detect, and investigate structure and function of biological systems.

1.6.2. Data analysis of FLIM

FLIM measures a three-dimensional data cube, containing both spatial and temporal information. Analyzing FLIM measurements is, therefore, more involved than analyzing intensity-based measurements. Analysis methods include rapid lifetime determination and analytical least-squares algorithms, iterative least-squares analysis with multiexponential fitting, phasor plot analysis, and methods for improving precision of fluorescence lifetime maps. These methods were developed for rapid, accurate, and high-throughput FLIM analysis.

An analytic RLD algorithm can be used to analyze time-gated FLIM data [47-49]. Iterative least-squares analysis can be performed to analyze TCSPC-FLIM data. The goal of iterative least-squares method is to minimize goodness of fit by varying the values of model parameters.

Phasor plot was further developed to offer a simple, graphical, and rapid algorithm for interpreting FLIM data that were obtained after single excitation frequency from samples exhibiting more than one fluorescence lifetime [50-52]. Precise fluorophore lifetime mapping was developed to quantify the biological microenvironment. One challenge to precise lifetime mapping is that all measurements must be obtained without perturbing living cells—a difficult task. The experimenter may be tempted to use high power and long measurement times to acquire high-quality images, but such conditions could damage the cells and fluorophores. The opposite can also be true. Low-light and fast measurements will maintain cell viability, but may not produce images with high signal-to-noise ratio. Temporal optimization and spatial denoising methods were developed to address this problem and enhance the precision of acquired FLIM data.

1.7. Dissertation Objective

With the understanding of optical imaging techniques and quantitative data analysis methods for assessing living biological systems, this dissertation details the development of label-free nonlinear optical molecular microscopy and quantitative analysis methods to assess living biological systems including cell lines, primary human cells, and tissue-engineered constructs manufactured with primary human oral mucosa for clinical use.

Specific Aim 1: To assess the viability of living primary human keratinocytes in tissue-engineered constructs by developing and verifying the label-free nonlinear optical molecular microscopy and quantitative methods. Nonlinear optical molecular imaging and quantitative analytic methods will be developed to non-invasively assess the viability of primary human cells in standard cultures and in tissue-engineered constructs. In standard cultures, careful verification of the technique will be performed. In tissue-engineered constructs, label-free optical measures of local tissue structure and biochemistry will characterize morphologic and functional differences between controls and stressed constructs.

Specific Aim 2: To assess tissue-engineered constructs with a range of viability by quantitatively comparing between optics and the traditional procedures. Rapamycin and thermal-stress will be employed to create a range of states of tissue viability. Their viability will be assessed by the standard procedures, quantitative histology scoring and WST-1assay, and optical molecular imaging. The optical measures will be compared to the standard procedures to characterize its potential of serving as noninvasive reliable

manufacturing release criteria for tissue-engineered constructs prior to human implantation.

Specific Aim 3: To distinguish between tissue constituents by one-channel label-free fluorescence lifetime imaging microscopy (FLIM) and developing error propagation analysis for the phasor plot. Tissue-engineered constructs will be imaged by one-channel label-free FLIM. The acquired FLIM images of the engineered tissues will be first processed with the previously developed phasor plot analysis for easy visualization of the lifetime distributions of the tissue constituents. Then, error propagation analysis will be developed for the phasor plot analysis to quantitatively distinguish between multiple constituents.

Specific Aim 4: To enable direct, rapid interpretation and visualization of the time-gated FLIM images by developing the phasor analysis algorithm for time-gated FLIM. A phasor analysis algorithm for time-gated FLIM will be developed for various gating schemes (separate, continuous, and overlapping gates) to provide rapid interpretation and visualization of the time-gated FLIM images.

1.8. Dissertation Overview

Chapter 2 describes the development of nonlinear optical molecular microscopy (fluorescence intensity, fluorescence lifetime, and second harmonic generation imaging) and quantitative algorithms (cellular metabolism, cellular organization, and lifetime characterization) and the verification of the technique with careful examinations.

Chapter 3 describes the viability assessments of tissue-engineered constructs by the developed nonlinear optical molecular microscopy and quantitative algorithms. The results were compared to standard procedures, quantitative histological scoring and biochemical tissue analyses.

Chapter 4 describes the viability assessments of tissue-engineered constructs with a range of states of tissue viability. The assessments were performed with optics and standard procedures, including histology, immunohistology, and the cell viability assay, and compared.

Chapter 5 describes the development of the error propagation analysis for the phasor plot. The developed algorithm was applied to label-free one-channel FLIM images from the engineered tissues to distinguish between tissue constituents. The result was compared to two-channel fluorescence intensity images and the fast FLIM map.

Chapter 6 describes the development of the phasor analysis for time-gated FLIM. Time-gated data from living cells have low fluorescence signals. Thus, the developed time-gated phasor analysis algorithm was combined with the previously developed TV denoising method to demonstrate intracellular features.

Chapter 7 concludes the dissertation, emphasizing the specific contributions described in the dissertation and future directions.

Chapter 2 Quantitative Characterization of Living Primary Human Cells to Verify Label-Free Optical Molecular Microscopy for Viability Assessments

Label-free nonlinear optical molecular imaging and quantitative analytic methods were developed to non-invasively and quantitatively assess the cellular viability. Rather than employing exogenous fluorescent dyes that are bright but invasive to cells, the method described here targets biologically- and metabolically-relevant endogenous tissue fluorophores, primarily nicotinamide adenine dinucleotide (phosphate) (NAD(P)H) and flavin adenine dinucleotide (FAD). NAD(P)H denotes the simultaneous analysis of NADH and NADPH as one fluorophore, grouped because of their similar fluorescence spectrum and their important roles in cellular metabolic function. NADH and FAD are mitochondrial coenzymes that report on cellular metabolism and oxygen consumption, and NADPH is an anabolic coenzyme largely produced by fast growing cells for biosynthesis [53]. Previous studies have shown that the NADH concentration and the quantum yield are greater than NADPH [54, 55]. Thus, it is likely that NADPH is responsible for a low fluorescence background.

NAD(P)H and FAD fluoresce in their reduced and oxidized states, respectively [38, 56]. Therefore, their concentrations typically trend oppositely to one another and their relative concentrations can be assessed with fluorescence intensity measurements characterized

by a redox ratio (RR) metric, defined as [FAD]/([FAD]+[NAD(P)H]) [42]. Intensity ratios like RR enhance the metabolic variations measured while reducing intensity-based artifacts, including signal variations due to optical loss, which may be difficult to quantify or control in tissues. Therefore, RR metric is suitable to characterize cancer cells, in which the cellular metabolism change from normal cells [57]. A complementary approach is fluorescence lifetime imaging microscopy (FLIM). In addition to two-dimensional spatial information, FLIM images contain a third dimension – time [37, 38, 42]. FLIM is advantageous for tissue-based sensing because fluorescence lifetime reveals molecular microenvironment (*e.g.*, temperature, pH, and binding), while being insensitive to intensity-based measurement artifacts. In this chapter, the instrumentations, the quantitative analytical methods, and the verification of the technique will be detailed.

2.1. Nonlinear optical microscopic imaging

Nonlinear optical microscopic imaging were performed with a Leica TCS SP5 microscope equipped with a Ti:Sapphire laser (Mai Tai, Spectra-Physics). The excitation laser source and the emission light were coupled through an inverted microscope with 40x (1.25 NA) / 63x (1.4 NA) oil immersion objective lenses to image oral keratinocytes in culture and a 25x water immersion objective lens (0.95 NA, 2.5 mm working distance) to image tissues. Tissues were imaged from the top surface down (*i.e.* through the topmost keratin layer) to mimic the measurement conditions *in vivo*. Prior to measurement on an inverted microscope, constructs were flipped over onto measurement dishes. This process was not expected to alter cellular viability or layer thickness.

2.1.1. Controlled imaging environment

All measurements were collected in a controlled environment (37°C with 5% CO_2) to mimic cell or tissue culture. Before each measurement, the excitation power at the specimen surface plane at both excitation wavelengths with a 10x objective was calibrated at 20 mW for standard cell cultures and 30 mW for tissue-engineered constructs to limit photobleaching and non-reversible changes in the sample. The laser power was selected after consulting literatures that concluded no short-term cellular damage occurred after 760 or 800 nm exposure with powers of 50 mW (~200 fs pulse width) [58] and 60 mW (~150 fs pulse width) [59], respectively. Currently, there are no FDA approved nonlinear optical microscopy systems for human use. However, a CE-certified device is commercially available in Europe and a preliminary clinical study in the US [60]. *In vivo* human studies have been conducted in recent years with a maximal laser power of 50 mW to assure safety [61-63]. Such imaging technologies will have medical risk profiles similar to FDA approved clinical imaging modalities, including X-ray and computed tomography instruments [64].

2.1.2. Label-free fluorescence intensity imaging

NAD(P)H was excited with excitation at 705 nm; FAD and collagen (to detect SHG) were excited with excitation at 900 nm. For NAD(P)H intensity detection, the backscattered fluorescence was collected through a band pass filter from 435 to 485 nm; for FAD intensity detection, the backscattered fluorescence was collected through a band pass filter from 500 to 550 nm (Leica DAPI/FITC filter cube). Emission light was

collected with short-coupling non-descanned photomultiplier tubes to increase collection efficiency.

The image acquisition settings above were applied for both cross-sectional and *en-face* imaging, except that the cross-sectional images were collected in x-z (vertical) direction and the *en-face* images were collected in x-y (horizontal) direction. Representative cross-sectional fluorescence images were overlaid with their corresponding SHG images, processed via Photoshop Screen function. No other post-processing was performed on representative *en-face* images.

2.1.3. Second harmonic generation imaging

An internal tunable photomultiplier collected SHG emission from 440 to 460 nm. Detector gain and offset were consistent for each measurement to avoid detector saturation. Images (1024 x 1024 pixels, 0.391x 0.391 μm^2 pixel size, 8-bit image depth) were acquired in ~40 seconds with a 200 Hz line scanning speed. The two fluorescence and SHG signals were acquired sequentially, with all three measurements occurring at each site in less than three minutes. To reduce background noise, a line average of eight was employed for all images.

2.1.4. Fluorescence lifetime imaging microscopy

For NAD(P)H FLIM detection, emission light was collected through a tunable monochromator from 410 to 490 nm coupled to a photomultiplier tube and photon counting add-on (HydraHarp TCSPC, Leica). FLIM measurements of cells in monolayer were collected (1024 x 1024 or 512 x 512 pixels, ~265 x 265 μm^2) until 100 counts were

reached in the peak channel, lasting an average of ~2 minutes per FLIM image. FLIM measurements of tissues were collected (512 x 512 or 256 x 256 pixels, ~400x400 μm^2) for 1.5 minutes.

2.2. Quantitative algorithms

Quantitative algorithms were developed to objectively assess cellular metabolism, cellular organization, and intracellular microenvironment.

2.2.1. Spatial intensity analysis for cellular organization

For spatial analysis, each raw NAD(P)H image was split into an 8x8 grid, totaling 64 sub-images. As a demonstration, ¼ of a NAD(P)H image with 16 of the 64 total sub-images was processed (**Fig. 2.1**). Image pre-processing was performed with a 3×3 median filter to reduce noise while preserving edges between the cytoplasm, nuclei, and extracellular components. Background fluorescence was removed with the binary mask containing SHG and keratin regions created as described in the previous section. Therefore, analysis was only performed on binary sub-images with < 10% of pixels signals being 1, indicating a sub-image with < 10% of total pixel fluorescence attributed to collagen, elastin, or keratin. A PSD map was then obtained and filtered with a 5×5 mean filter to reduce noise from each binary sub-image. To quantify the PSD characteristics, radial angle-averaged PSD values (ϕ) were calculated and plotted versus spatial frequency (κ) on a logarithmic scale. In the spatial frequency range of 0.14 – 0.5 μm^{-1}, the PSD curve was modeled with an inverse power law, $\phi(\kappa) \propto \kappa^{-\alpha}$, and was

linearly fit to extract the corresponding power exponent (α). A Hurst parameter (H) was then derived with the equation H = ½(α -1) (**Fig. 2.1b**). Matlab was employed for all post-processing methods described above.

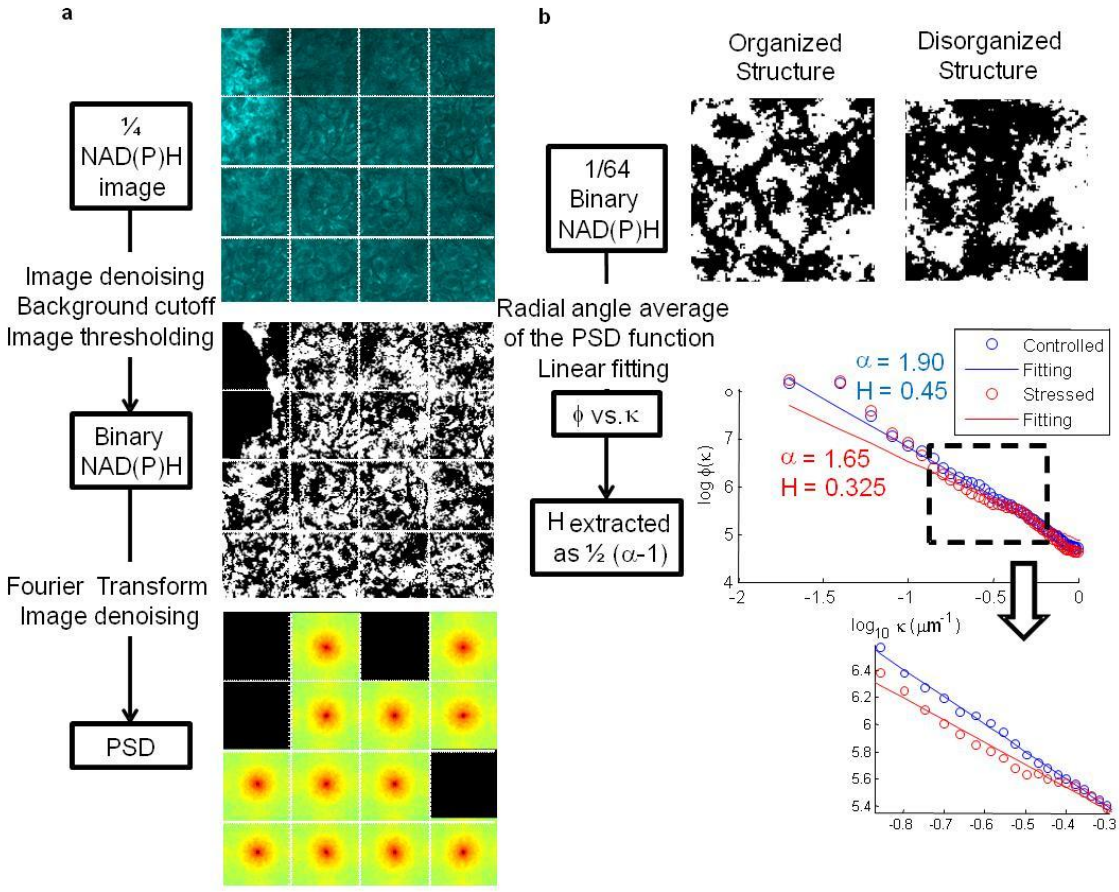

Figure 2.1 Fourier analysis characterized cellular organization. (a) Overall analysis procedure for ¼ of a representative NAD(P)H image. Subimages with excessive SHG signals or keratin signals were excluded from analysis. (b) Demonstration of detailed Fourier analysis of two subimages. Binary images of the organized (left) and the disorganized (right) structures were compared. Images were post processed with the protocol shown in (a). Result shows that as image became disorganized, decreasing α and Hurst parameter H were extracted. The detailed procedure can be found in the Methods.

2.2.2. Redox ratio (RR) map for cellular metabolism

For cells in culture analysis, two raw fluorescence images, one each of NAD(P)H and FAD, were inputs into developed analysis software. Images were pre-processed with a 3 × 3 median filter to increase image contrast. Then, a threshold value was set as the average fluorescence intensity signal from the whole image to create a binary mask which was employed to reduce background fluorescence signals. This binary mask filtered each raw fluorescence image. A redox image was then calculated at each pixel as [FAD]/([NAD(P)H] + [FAD]).

Figure 2.2 shows the method to calculate *en-face* redox ratio maps in an engineered tissue. The first step removed regions with high background identified as pixels with collagen SHG signal. For basal layer images with collagen fluorescence, three 1024 × 1024 images (400 × 400 μm^2), denoised NAD(P)H, denoised FAD, and denoised SHG, were used for analysis. The SHG image, which identified regions with collagen, was further denoised with Markov random field denoising. Markov random field denoising clumped the pixels with strong collagen SHG signals together. Subsequently, pixels having SHG intensity greater than the average SHG signals from the whole image were removed from their corresponding NAD(P)H and FAD fluorescence images. Processed NAD(P)H and FAD fluorescence images were then used to derive a redox ratio at each image pixel.

Image processing was performed in Matlab to remove image pixels with high fluorescence contribution from keratin (attributed to keratin in the keratin layer) in a two-step process. First, images from the differentiating cellular layer that contained keratin fluorescence were processed to create a redox ratio map. Then, Markov random field

denoising was applied to the calculated redox ratio map to exclude the pixels with abnormally high redox ratio (attributed to keratin).

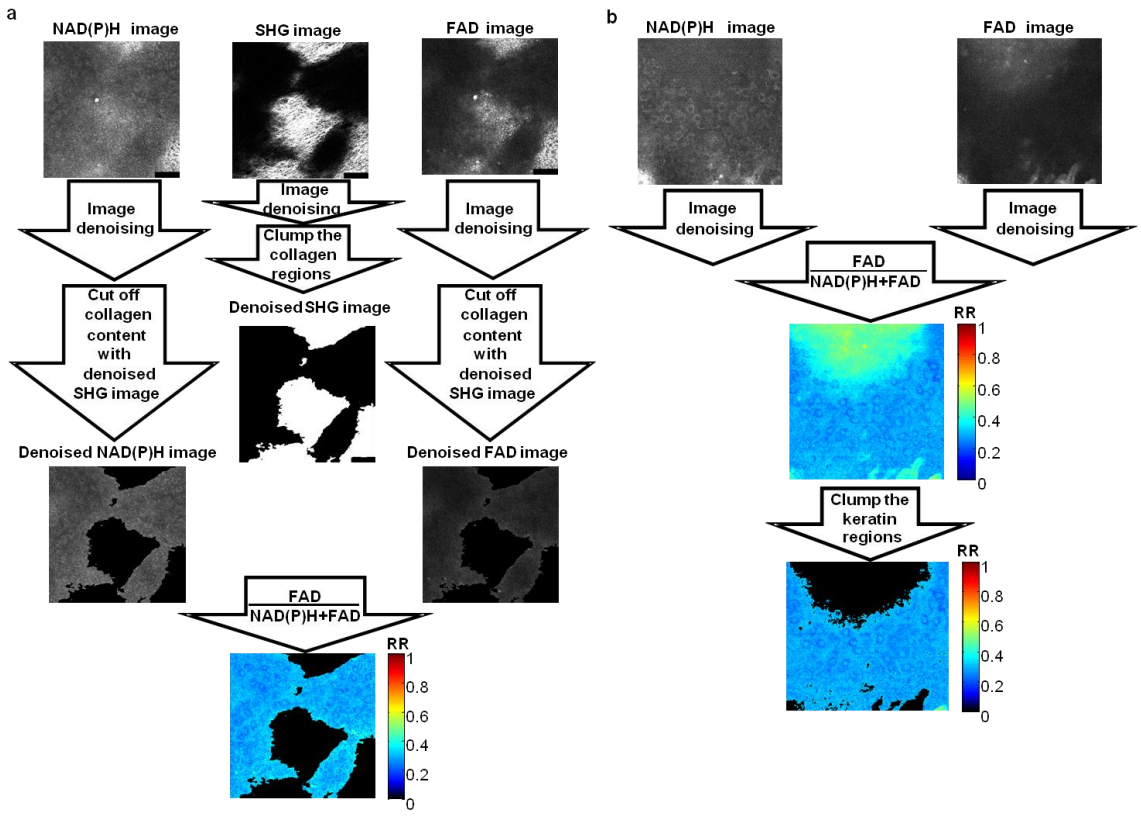

Figure 2.2 Redox ratio map generation flow chart Redox ratio metric protocol for (a) basal cellular layer containing collagen and (b) differentiating cellular layer containing keratin. The detailed procedure can be found in the Methods.

2.2.3. FLIM analysis – exponential fitting

For each FLIM image, methods of analysis were performed to assess intracellular microenvironment. Standard exponential fitting was performed with Leica SymPhoTime software. Composite decays were analyzed after summing all pixels within the defined region. Data was best fit to a bi-exponential decay model, $F(t) = a_1e^{-t/\tau1} + a_2e^{-t/\tau2}$, evaluated by the minimization of the goodness of fit χ^2 parameter. Additionally, the fit reproducibility between sequential fittings of the same fluorescence decay was evaluated to be much stable for two-exponential than three-exponential fits.

For NAD(P)H, lifetimes from two-component exponential fits are attributed to contributions from protein-bound (long-lived τ_1) and free (short-lived τ_1) forms of the molecule. The iterative fitting procedure deconvolved an instrument response function (IRF) from each decay, measured as the second harmonic generated response from a collagen sample. Percent contribution from τ_1 was calculated as $a_1/(a_1+a_2)$. An alternative rapid fluorescence lifetime determination method is so-called fast FLIM images developed by SymPhoTime. The method uses the average arrival time of fluorescence photons after the excitation pulse as a measure for the average lifetime.

2.2.4. FLIM analysis – phasor plot analysis

An alternative to the computationally expensive exponential fitting procedure, phasor plot analysis was applied to FLIM images. Phasor plots enable rapid visualization of lifetime distributions within samples. In phasor analysis, fluorescence decay traces, $F(t)$, were input directly into phasor equations

$$g = \frac{\int_0^\infty F(t)\cos(\omega t)\,dt}{\int_0^\infty F(t)dt}$$

and

$$s = \frac{\int_0^\infty F(t)\sin(\omega t)\,dt}{\int_0^\infty F(t)dt},$$

at each pixel of an image, where ω = laser repetition angular frequency. Each pixel of the image generates the two coordinates (g & s as shown in the equations above) of a point on a phasor plot. Phasor plots will assist in rapidly distinguishing FLIM differences between free and protein-bound NAD(P)H. More details of phasor can be found in Chapters 5&6.

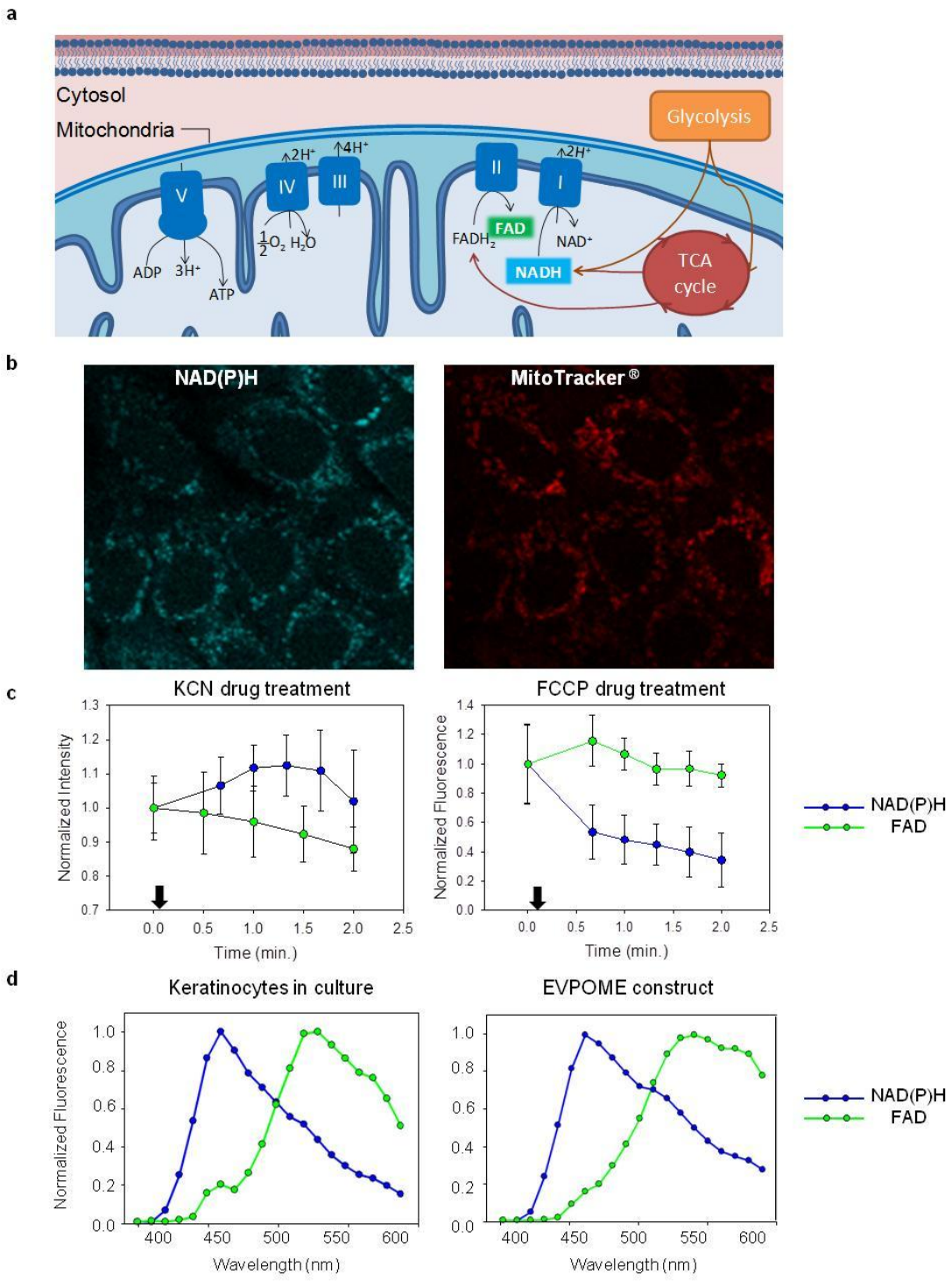

Figure 2.3 Experimental studies performed to demonstrate that the majority detected fluorescence could be attributed to NAD(P)H and FAD.

2.3. Verifications

Rigorous sample testing ensured the preferential detection of NAD(P)H and FAD fluorescence in both primary human oral keratinocytes in culture and in tissue-engineered constructs (**Fig. 2.3**).

2.3.1. Intracellular autofluorescence from mitochondrial metabolic cofactors NAD(P)H and FAD

NADH molecules, the energy source of the electron transport chain when an NADH is oxidized to a NAD+, are a by-product of glycolysis and the tricarboxylic acid (TCA) cycle. Alternatively, FAD molecules are a by-product of ATP generation when $FADH_2$ molecules become oxidized. **Figure 2.3a** shows simplified mitochondrial pathway to generate adenosine triphosphate (ATP).

MitoTracker®, an exogenous fluorescence dye that only fluoresces within mitochondria, stained the cell culture samples for co-localized fluorescence from both MitoTracker® and NAD(P)H. Images of primary human oral keratinocytes in culture demonstrate the co-localization of endogenous fluorescence to cellular mitochondria from ~10 cells (**Fig. 2.3b**). NAD(P)H image shows cellular morphology with endogenous fluorescence which is co-localized to the MitoTracker® image. MitoTracker® image was acquired by exciting an exogenous contrast agent, MitoTracker®, which fluoresced when oxidized by and sequestered in the active mitochondria. The two images represent areas of the cells with active mitochondria. Areas within the dark circular regions are the cell nuclei.

2.3.2 Drug treatments to alter metabolic pathways

The metabolic inhibitor, 4 mM KCN, and the uncoupler, 0.5 μM FCCP, (both from Sigma-Aldrich, St. Louis, MO) were employed to vary cellular metabolism. The variation was monitored for two minutes. KCN/FCCP was administered immediately after acquiring the first image.

Metabolic NAD(P)H and FAD were shown to be main fluorophores through adding potassium cyanide (KCN) and carbonyl cyanide p-trifluoromethoxy phenyl hydrazone (FCCP) to human oral keratinocytes in culture. KCN inhibits complex IV of the electron transport chain, promoting reduction of NAD+ molecules and thus increasing NAD(P)H concentration while concurrently decreasing FAD concentration. FCCP uncouples electron transport, driving the metabolic pathway into oxidation, reducing NAD(P)H concentration while concurrently increasing FAD concentration. KCN and FCCP were administered immediately after the acquisition of the first image (**Fig. 2.3c**, black arrows). Fluorescence images were acquired over two minutes. In the post-processing, fluorescence intensity was integrated over individual cells (15 cells for KCN experiment and 10 cells for FCCP experiment) at each time point, and normalized to the maximal intensity over the time course for each cell. The overall average fluorescence was then normalized to the first time point and plotted. The error bars represent standard deviation.

2.3.3 Spectroscopic analysis

Spectroscopic analysis was performed for (**Fig. 2.3d,** left) primary human oral keratinocytes in culture and (**Fig. 2.3d**, right) in tissue-engineered constructs with two excitation wavelengths, 705 and 900 nm, to preferentially excite NAD(P)H and FAD,

respectively. Measured fluorescence spectra were similar between samples and the pure NAD(P)H and FAD spectrum. Keratin content, however, was observed from fluorescence spectrum of engineered tissues. At 705 nm excitation, the measured fluorescence spectrum of human oral keratinocytes in culture peaked at 460 nm and decreased ~0.6 fold at 500 nm, while that of engineered tissues decreased ~0.7 fold; at 900 nm excitation, the measured fluorescence spectrum of human oral keratinocytes in culture decrease ~0.8 fold at 550 nm, while that of engineered tissues decreased ~0.9 fold. This increase in measured fluorescence was attributed to increased keratin content in differentiating tissues, estimated at ~17% based on our measurements. However, this keratin content is hypothesized to be relatively consistent between control and compromised constructs and therefore have little impact on our measurements. An additional fluorophore that may be present is lipofuscin, a biomarker for aging cells [65]. However, we did not find a relationship between patient age and fluorescence intensity of human oral keratinocytes, which would have indicated the presence of lipofuscin.

2.4. Label-free nonlinear optical molecular microscopy and RR maps quantitatively assessed cellular metabolism in standard culture

Fluorescence images of NAD(P)H and FAD (**Fig. 2.4**) demonstrated the size and shape of living primary human keratinocytes. Keratinocytes had a well-defined shape surrounding a roughly circular, non-fluorescent cellular nucleus region. These cells were homogenously distributed across the entire site.

RR maps provide a quantitative metric to compare relative metabolic rates of measured samples. A lower RR corresponds to relatively lower FAD fluorescence and/or higher

NAD(P)H fluorescence, indicating a higher cellular metabolic rate [42]. The RR metric assessed local cellular metabolism (**Fig. 2.4, right**). Proliferating cells were spatially separated (**Fig. 2.4a**) as compared to differentiating cells (**Fig. 2.4b and c**), which tended to crowd together. Shown in (**b**) and (**c**) are images of two layers at the same site, and the bottom layer is 9 μm deeper than the top. Both proliferating and differentiating keratinocytes exhibit high NAD(P)H fluorescence but low FAD fluorescence, resulting in a low RR (noted as blue pixels in the RR maps). In particular, proliferating keratinocytes in (**a**) have low perinuclear RR because highly metabolic mitochondria gathered around the nuclei, shown as the dark blue rings in the binary RR map. Differentiating keratinocytes in (**c**), on the other hand, homogeneously exhibit dark blue pixels over the binary RR map. In addition, as keratinocytes differentiated upwards, some cells had slightly higher average RR seen as the appearance of light blue pixels in the differentiating layer RR map, indicating their decreasing metabolic activity.

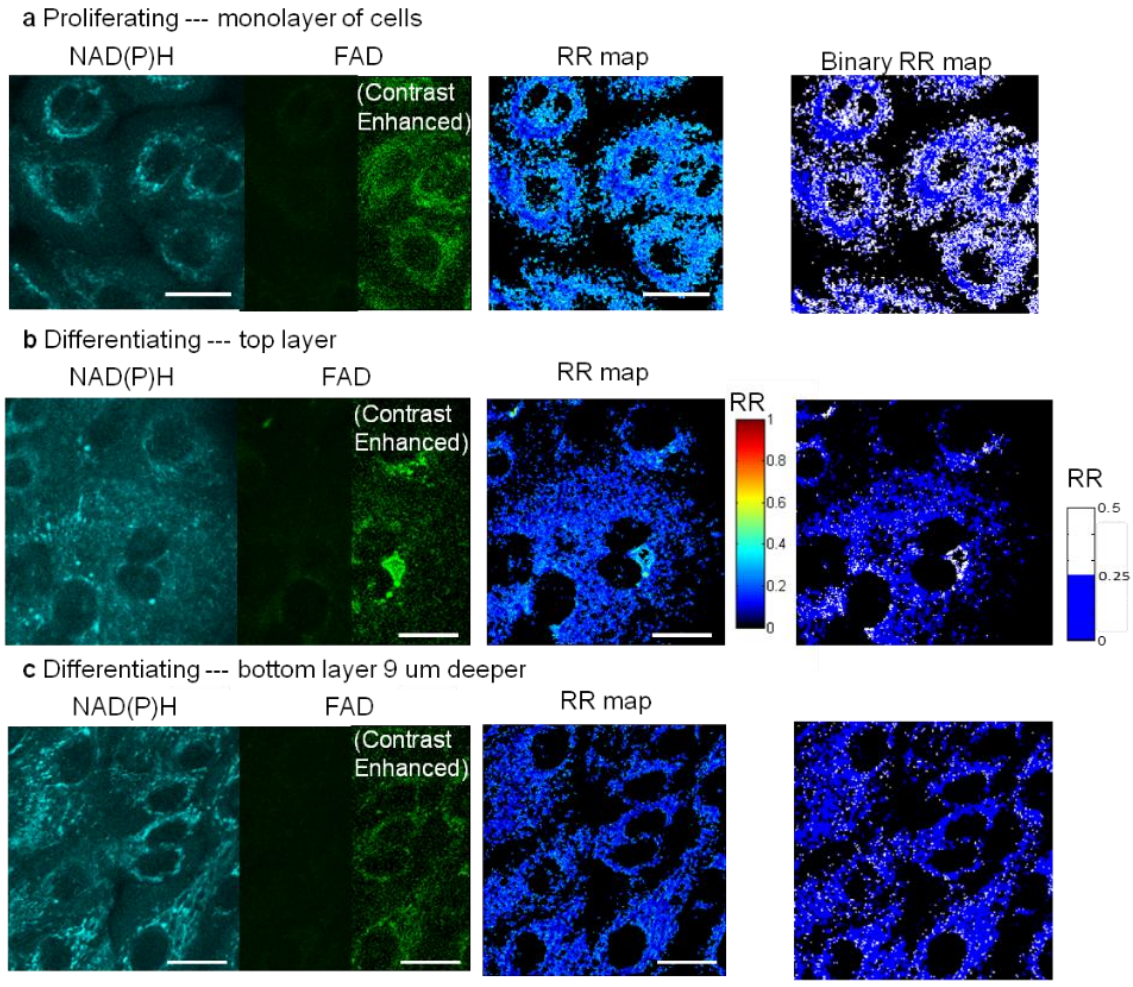

Figure 2.4 Label-free optical microscopy imaged (section thickness < 1 μm) a single layer of primary human oral keratinocytes in culture. (a) In low-calcium (0.06 mM) medium, keratinocytes proliferated, forming a cellular monolayer. (b) In high-calcium medium (1.2 mM), keratinocytes differentiated into a layered structure, which was sectioned by nonlinear optical microscopy. Note: For display, contrast enhancement on half of the dim panels was performed by setting image minimum at 10 and maximum at 100 in a scale of 0-255. Scale bars: 20 μm.

2.5. Redox Ratio distinguished thermally-stressed primary human oral keratinocytes from control in standard culture

En-face fluorescence images were employed to quantify the relative local metabolic rate via analysis of intracellular autofluorescence variations. The RR metric assessed local cellular metabolism in primary human oral keratinocytes in culture (**Fig. 2.5**). Cell culture samples with high proliferation and differentiation were assessed with high resolution fluorescence images and redox ratio maps (**Fig. 2.5a**). The greenish colors indicate a relatively high RR, signifying low metabolic activity (top row, thermally-stressed), while the blue color indicates a relatively low RR, signifying high metabolic activity (bottom row, control). Thermal stressing was applied to the cell culture samples from 4 patients to incorporate patient-dependent cellular metabolic variability. A linear mixed effect model was employed to account for intrapatient variability (detailed in Chapter 3, Sec 3.2.4.).

Two culture conditions were achieved by controlling Ca^{2+} culture medium concentrations to yield proliferating (P) or differentiating (D) cells. For each batch, a control and a thermally-stressed sample were cultured. For each cell culture sample, two sites were randomly measured and analyzed. Lower RR was extracted from control compared to thermally-stressed keratinocytes (**Fig. 2.5b&c**, for 4 batches with 8 control and 8 thermally-stressed sites analyze, *P*-value = 0.004). The single-channel (NAD(P)H or FAD alone) fluorescence intensity imaging cannot distinguish between the control and the thermally-stressed cells, as discussed in Sec.3.3.5.

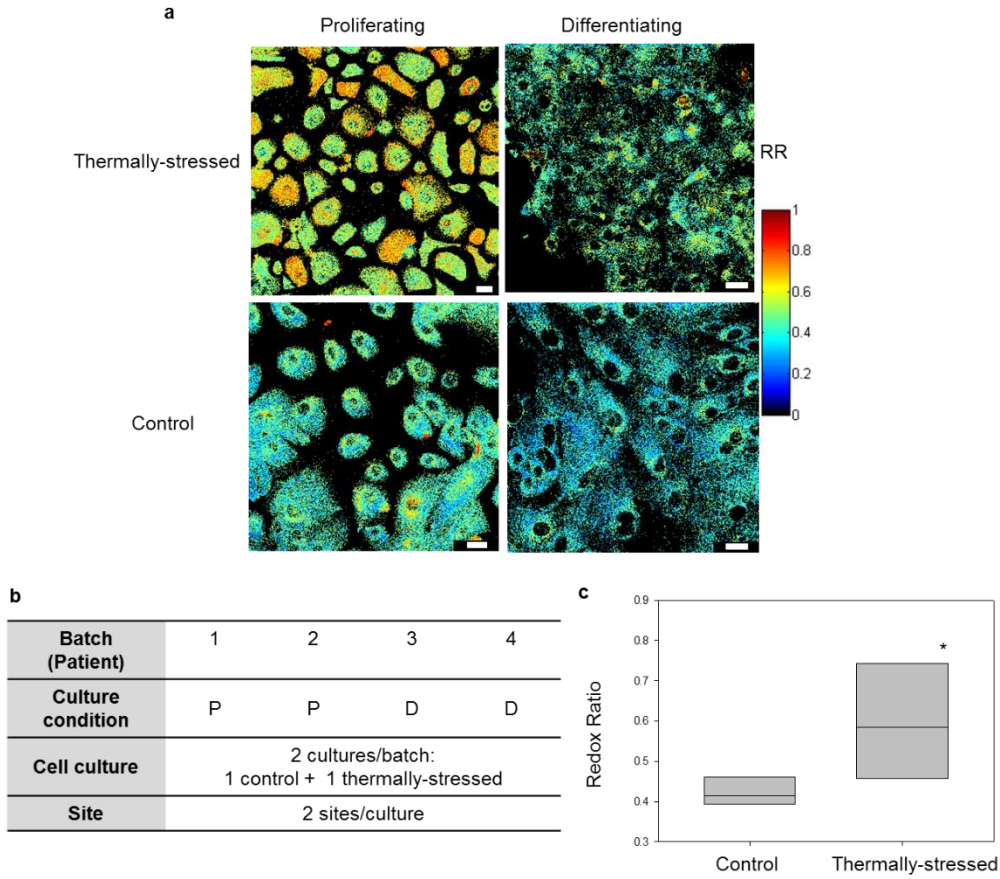

Batch (Patient)	1	2	3	4
Culture condition	P	P	D	D
Cell culture	2 cultures/batch: 1 control + 1 thermally-stressed			
Site	2 sites/culture			

Figure 2.5 (a) Representative RR maps of control and thermally-stressed proliferating and differentiating keratinocytes. Scale bar: 25 μm. (b) Table shows the experiment design. (c) Cell culture samples showed significantly increased RRs for thermally-stressed cells as compared to control cells, indicating decreased cellular viability (* For 4 batches with 8 control and 8 thermally-stressed sites analyzed, *P*-value = 0.004).

2.6. FLIM quantitatively distinguished thermally-stressed primary human oral keratinocytes from control in standard culture

Individual cells were randomly selected for FLIM analysis with two component exponential fitting. Fluorescence decays from the control and thermally-stressed keratinocytes were compared. Control keratinocytes has a narrower fluorescence decay relative to the stressed keratinocytes. This result indicates that control keratinocytes have a lesser contribution from bound NAD(P)H as compared to thermally-stressed keratinocytes. It is noted that since FLIM is sensitive to environmental changes, careful control of sample microenvironment as described in Sec.2.1.1. is important to ensure the origin of changes observed in lifetime measurements between samples (*e.g.* control versus stressed).

Batch (Patient)	1	2	4
Dish culture	2 control + 1 stressed	1 control + 1 stressed	1 control + 1 stressed
Measured site	4 control + 2 stressed	5 control + 3 stressed	2 control + 2 stressed
Analyzed cell	41 control + 14 stressed	67 control + 33 stressed	22 control + 24 stressed

Table 2.1 Number of cells analyzed from 3 batches of human primary keratinocytes from 3 individual patients.

Extracted lifetime fitting parameters from each bi-exponential fit were employed to quantitatively assess local cellular viability. The two extracted lifetimes were interpreted as the contributions from free and bound NAD(P)H, as our extracted fitting parameters were consistent with previously reported literature studies [42]. The fitting amplitude

parameters extracted were employed to calculate the percent contribution from the slow tau component, quantifying the relative concentration of bound to free NAD(P)H. Control cells had a lower percent contribution from τ_1 compared to thermally-stressed cells (*P*-value < 0.001 for 3 batches with 130 control and 71 thermally-stressed cells analyzed as shown in **Table 2.1**), indicating a lower concentration of bound NAD(P)H (relative to free NAD(P)H).

Rapid data analysis methods, fast FLIM and phasor plot analysis, was performed to analyze the FLIM images. **Figure 2.6a** shows fast FLIM images from one control and one thermally-stressed dish culture. The thermally-stressed cells had a longer average lifetime (green to yellow) than the control cells (blue), consistent with the standard exponential fitting results. Phasor plot analysis transformed fluorescence decays of the 130 control and 71 thermally-stressed cells from 3 batches to the phasor plot (**Fig. 2.6b**). The blue points represent the control cells and the red points represent the thermally-stressed cells. Phasor plot significantly distinguished control and thermally-stressed cells (For 3 batches, *P*-value = 0.024 for the g coordinate, *P*-value = 0.053 (marginal) for the s coordinate, and *P*-value = 0.001 for the g/s).

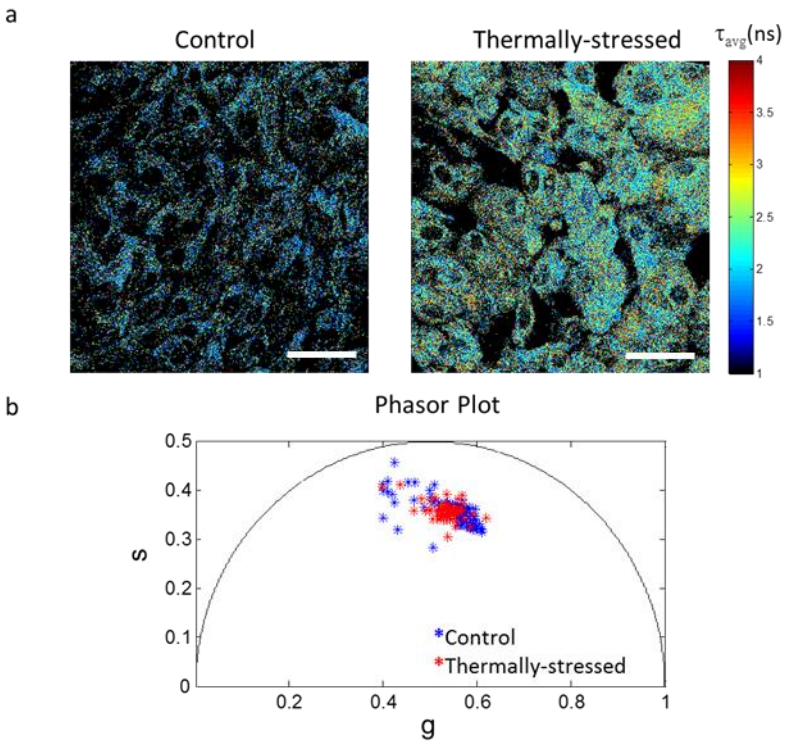

Figure 2.6 Raid FLIM data analysis methods: (a) fast FLIM images and (b) phasor plots, distinguished between control and thermally-stressed human oral keratinocytes in standard cultures. The fast FLIM images show longer average lifetimes in the thermally-stressed cells as compared to the control cells. The phasor plot significantly distinguished between control (blue points) and thermally-stressed (red points) cells. Scale bars: 40 μm.

2.7. Conclusions

To the best of our knowledge, this is the first report employing label-free nonlinear optical microscopy to characterize *in vitro* cell-based devices manufactured with primary human cells. Cellular viability information, primarily contained within fluorescence signals from metabolic co-factors NAD(P)H and FAD, was obtained by optically sectioning thin cellular layers via nonlinear optical microscopy. The acquired optical signals enabled tissue viability assessment via spatial, optical redox ratio (RR), and FLIM analysis. Importantly, nonlinear optical imaging with FLIM provided contrast using only

a single detection channel (NAD(P)H), unlike RR which required two detection channels (NAD(P)H and FAD).

The chapter described the development of label-free optical molecular imaging and quantitative algorithms. The technique was first verified by careful characterization of primary human cells from multiple patients in standard culture. In the next chapter, the technique will be employed to assess the viability of living tissue-engineered constructs manufactured with patient's freshly-harvested primary cells.

Chapter 3 Label-Free Nonlinear Optical Molecular Microscopy to Assess Engineered Tissue Viability

Recent advances in tissue engineering and regenerative medicine (TERM) have become an integral part of reconstructive surgery and tissue/organ regeneration. One such advance is the development of tissue-engineered constructs, which are classified by the United States Food and Drug Administration (FDA) as combination products comprised of an engineered extracellular matrix and a biological component. Biological device manufacturing is strictly regulated by the FDA prior to product release for patient treatment to assure effectiveness and safety. It is essential that the device is objectively (*i.e.*, quantitatively) and non-invasively (*i.e.*, without sectioning or staining) evaluated in real-time to assess cellular viability [66, 67], which is the significant technical challenge we address here by developing quantitative methods for tissue-based, label-free nonlinear optical molecular microscopy.

Sensitive, spatially-resolved measures of NAD(P)H and FAD in unstained tissue constructs were achieved by developing quantitative nonlinear optical molecular microscopy methods to optically (non-invasively) section tissue samples into layers as thin as 1 μm [32, 36, 68, 69]. Such image resolution enabled the detection of optical signals from a single cellular layer of a three-dimensional engineered tissue. In addition,

nonlinear optical techniques enable specific measurements of collagen molecules through second harmonic generation (SHG). Because extracellular collagen and intracellular NAD(P)H and FAD have similar fluorescence characteristics, measuring collagen via SHG enables the spatial separation of intracellular (NAD(P)H and FAD) and extracellular (collagen) fluorescence via image post-processing. Therefore, by combining optical sectioning with fluorescence and SHG measurements, tissue fluorescence arising from cells can be analyzed to quantitatively characterize cellular metabolism and cellular organization for tissue viability assessment from a single cellular layer [42, 70].

As a model system for our studies, we employed the engineered cell-based device EVPOME (*Ex Vivo* Produced Oral Mucosa Equivalent) [66]. EVPOMEs are manufactured by culturing primary human oral keratinocytes atop a dermal equivalent scaffold for tissue formation. EVPOMEs, developed for intraoral grafting procedures for reconstructive surgery of oral and dental soft tissues, were demonstrated to reduce patients' wound healing time by half [71]. In addition, EVPOMEs were implanted successfully in humans during an FDA approved Phase I clinical trial [72].

3.1. The model system: *Ex Vivo* Produced Oral Mucosal Equivalent (EVPOME)

The EVPOME manufacturing process takes 11 days. On day 11, EVPOME construct is a 3-dimensional thick tissue with a surface layer of keratin (~10-20 μm thick), a subsurface layer of keratinocytes (~40 μm thick), and a base that contains collagen (~400-500 μm thick).

3.1.1. Procurement of human oral mucosal tissues

Discarded keratinized oral mucosa was collected from patients undergoing minor oral surgical procedures at the University of Michigan (UM) hospital. The UM Medical School Institutional Review Board approved use of the mucosa and patients provided informed consent for research use. The study adhered to the Declaration of Helsinki Guidelines.

3.1.2. Standard protocols for culturing human oral keratinocytes and manufacturing EVPOMEs

Primary human oral mucosal tissues were harvested from procured discarded keratinized oral mucosa and cultured according to previously described protocols [66]. Briefly, primary human oral keratinocytes were enzymatically dissociated from the tissue samples. Oral keratinocyte cultures were established in a chemically-defined, serum-free culture medium (EpiLife and EDGS, Invitrogen/Life Sciences, Carlsbad, CA). The medium contained 0.06 mM calcium, 25 μg/ml gentamicin, and 0.375 μg/ml fungizone (both from Sigma, St.Louis).

For cell culture studies, the oral keratinocytes were seeded onto a 3.5 cm glass bottom dish (MatTek Corp., Ashland, MA) coated with collagen. Calcium concentration in the growth medium was controlled at 0.06 mM for cell proliferation and 1.2 mM to induce cell differentiation.

For EVPOME studies, EVPOME constructs were manufactured by first seeding 200,000 cells/cm^2 on 1 cm^2 acellular cadaver skin (AlloDerm®, LifeCell, KCI, Branchburg, NJ)) that was pre-soaked in 0.05μg/μL human type IV collagen at 4°C overnight (Sigma-

Aldrich, St. Louis, MO). Resulting keratinocytes and AlloDerm® were submerged in medium containing 1.2 mM calcium for 4 days and then raised to an air-liquid phase for an additional 7 days to induce cell stratification and differentiation. Control constructs were cultured in 100 mm dishes (for thermally-stressed) or in 6-well plates (for metabolically-stressed) with inserts in incubators at 37°C with 5% CO_2 for all culture days.

Stressing conditions (N_I = batches with fluorescence intensity data) (N_L = batches with fluorescence lifetime data) (Number of batches) / (Number of observations)				Gold standard		Potential release criteria							
						Fluorescence Intensity						Fluorescence Lifetime	
						Intensity			Spatial analysis				
		N_I	N_L	Histology	Glucose	NADH	FAD	RR	*En face* organization	Cross sect. thickness		(A1) NADH	NADH Avg Tau
										K	LC		
Thermal	Control	5	5	5/5	5/5	5/30	5/30	5/30	5/11	5/7	5/7	5/58	5/58
	Thermally-stressed			5/5	5/5	5/30	5/30	5/30	5/8	5/8	5/8	5/33	5/33
Metabolic	Control	5	2	5/5	5/5	5/30	5/30	5/30	5/12	5/6	5/6	2/24	2/24
	Starved			5/5	5/5	5/26	5/26	5/26	5/9	5/8	5/8	2/20	2/20
Drug-treated	Control	3	1	3/3	3/3	3/18	3/18	3/18	3/9	1/1	1/1	1/6	1/6
	$[Ca^2]$ = 2.4 mM			3/3	3/3	3/17	3/17	3/17	3/9	1/1	1/1	na	na
	$[Ca^2]$ = 3.6 mM			2/2	2/2	2/8	2/8	2/8	1/4	1/2	1/2	1/6	1/6
	$[Ca^2]$ = 4 mM			2/2	2/2	2/9	2/9	2/9	1/3	1/1	1/1	1/4	1/4
	Control	5	2	5/7	5/7	3/17	3/17	5/35	2/6	3/7	3/7	2/11	2/11
	C+Rapa			3/3	3/3	2/9	2/9	3/15	1/3	2/2	2/2	2/12	2/12
	Rapa+C			5/6	5/6	3/24	3/24	5/36	3/12	3/6	3/6	2/9	2/9
	Rapa+Rapa			4/4	4/4	2/9	2/9	4/21	1/3	2/2	2/2	2/8	2/8

Table 3.1 Table shows study design with multiple stressing mechanisms, multiple assessment tools, multiple assessment metrics, number of batches (patients), and number of measurements

3.2. Study Design

Table 3.1 shows experiments designed to vary EVPOME's viability and the tools and metrics employed to assess the tissue viability. Four stressing conditions were applied to the EVPOME constructs including extreme cases, thermal and metabolic stress, and drug treatments, various concentrations of calcium and rapamycin treatment during different culture stage. In Chapter 3, studies of thermal stressing and metabolic stressing will be discussed. In Chapter 4, the rapamycin treatment studies will be discussed.

Also shown in the table are the number of patients included and the number of measurements performed and analyzed. Since primary human cells were investigated with high variability between patients, multiple patients were included in the study. Statistical analysis was performed rigorously on the patient level instead of on the measurement level to avoid the incorrect significant results due to the increased statistical power resulted from the large number of measurements.

In the dissertation, a batch is defined as primary cells harvested from one individual patient. Take the thermal stress experiment for example, 5 batches means that 5 control constructs and 5 thermally-stressed constructs were manufactured for the viability assessments. That is, in 1 batch with cells from 1 patient, 2 constructs (1 control and 1 thermally-stressed) were manufactured.

3.2.1. Histology assessment

Prior to optical measurements on day 11 post-seeding, a piece of the EVPOME was removed (~20% of total construct area), fixed in 10% formalin, washed with PBS (phosphate buffered saline), and then placed in 70% ethanol solution. All specimens were

processed by the histology core at the UM Dental School, cut into 5μm sections and stained with hematoxylin and eosin (H&E). The processed H&E histology slides were assessed by a panel of three blinded expert readers, each with several years' experience in working with EVPOME constructs. Each histology slide had two to three slices sectioned from one EVPOME. For two of the five batches for FLIM analysis, histology and glucose readings were not directly obtained from the measured constructs, but instead from concurrently cultured constructs from the same primary human cells.

Classification criteria were developed by the expert readers prior to evaluation, where a viability score of 1 (least viable), 2, 3, 4, or 5 (most viable) was used. The classification criteria included the basal cell layer health, the construct cellular organization, and the keratin layer structural quality (**Fig. 3.1**). The classification criteria are defined as follows.

1: AlloDerm® with few to no cells, no cellular organization, and an unstructured keratin layer

2: AlloDerm® with a thin basal layer of cells and sporadic nuclei, flaky separation between the cell layer and keratin layer, and a keratin layer with wispy, not compacted structure

3: AlloDerm® with a thin basal layer of cells and sporadic nuclei, thin superficial layers with gradually flattening cells, and a top layer of pink, compacted keratin.

4: AlloDerm® with moderate basal layer of cells with nuclei and rounded cells, moderate superficial layers with gradually flattening light blue cells, and a top layer of pink, compacted keratin.

5: AlloDerm® with thick basal layer of cells with many nuclei and rounded cells, thick superficial layers with many gradually flattening cells, and a top layer of pink, tightly compacted keratin.

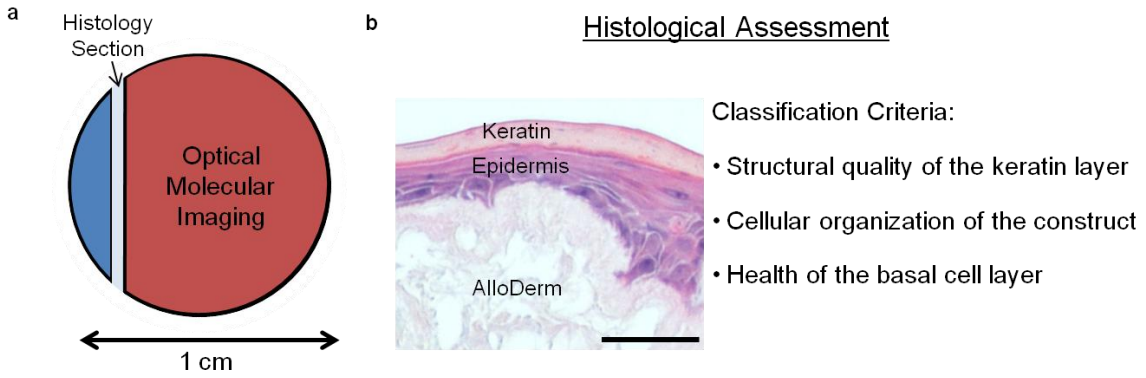

Figure 3.1 Histology scoring was performed by three expert readers. (a) Each of the 1 cm diameter EVPOMEs was assessed at Day 11 post-seeding. A section was sliced for H & E and the remainder of the EVPOME was used for the nonlinear optical molecular imaging. (b) Histology assessment based on the three criteria: (1) structural quality of the keratin layer, (2) cellular organization of the construct, and (3) health of the basal cell layer.

Definitions were agreed upon by all readers. Several representative histology images from each group were selected as a baseline to calibrate readers. The readers then individually assigned a score to each EVPOME histology slide, while blinded to the EVPOME stressing condition and to the other readers' scores.

The representative histology images were acquired with a Nikon Eclipse Ti inverted microscope. A 10x objective (0.25 NA, air) was employed to capture 8-bit bright-field images, resulting in histology images of 2560 x 1920 (pixel size of 0.481 μm) or 1280 x 960 pixels (pixel size of 0.971 μm).

3.2.2. Glucose

The glucose consumption was analyzed as the consumption from day 10 to day 11. On day 11, the glucose concentration of the culture medium was read by a glucose meter (ACCU-CHEK®, Aviva, Roche, Indianapolis, IN). Measuring glucose consumption during manufacture is non-destructive, but is unreliable: **Figure 3.2** shows vastly different glucose readings taken from control and stressed EVPOMEs for five batches, illustrating the inconsistency of the glucose assay as a release criterion

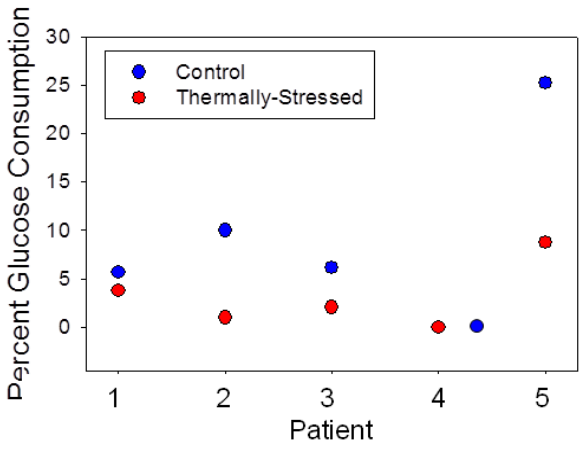

Figure 3.2 Measuring glucose consumption on day 11 for 5 batches in the thermal stress experiment.

3.2.3. Thermal and metabolic stressing protocols

Thermally-stressed constructs were cultured at 43°C for 24 hours beginning on day 9 post-seeding and were returned to normal culture conditions starting day 10. To create metabolically-stressed constructs, constructs received no fresh culture medium for 6 days beginning on day 4 post-seeding and were returned to normal culture conditions starting

day 10. We note that for the first batch of the metabolic-stress experiment, the construct was starved from day 4 to day 11. As a result, there is no glucose consumption measurement for this patient. In this study, we have grouped optical results from both metabolic-stress protocols because there were no observed differences from construct histology results. For two batches measured in the FLIM thermal stressing study, we note that two of the five batches had no histology or glucose samples measured. Their reported glucose and histology metrics were measured from constructs cultured in parallel with the same primary human cells.

3.2.4. Statistical analysis

Statistical analysis was performed with a test based on fitting a linear mixed-effects model [73]. The analysis uses stringent criterion to account for the data hierarchical nature where, for optics data, measures were taken from multiple sites per EVPOME, and multiple EVPOMEs obtained per patient, and for histology data, multiple histology samples were sectioned per patient and each section was read by four expert readers. For example, for the analysis of standard cell culture data, the mixed-effects model used with patient and cell culture as random intercepts to account for the two levels of nesting where sites were sampled within cultures, and cultures were sampled from within patients. Using these models, we also tested for any differences associated with the differentiated versus proliferated cells or the top versus bottom layer, and when we did not find any differences associated with these with respect to not only the associated statistical significance, but also the magnitude of the associated difference estimate, we dropped these variables from the models. For each parameter, we estimated the mean difference

and the corresponding 95% confidence intervals (CI) between stressed versus control conditions based on these models. All tests were conducted using a significance level of 0.01.

3.3. Label-free optical molecular imaging to assess tissue engineered constructs

Optical release criteria were developed from nonlinear optical molecular microscopy images in cross-sectional and *en-face* geometries. Measured cross-sectional images were non-invasive analogues to a histology section, while measured *en-face* images preferentially isolated a single cellular layer (**Fig. 3.3**). EVPOME's layered structure is evident in the histology (**Fig. 3.3,** left) and in the cross-sectional image (**Fig. 3.3,** middle) of cellular autofluorescence (NAD(P)H, cyan) with overlaid scaffold SHG (collagen, blue). EVPOMEs were composed of (1) a stratified cellular layer with > 3 cellular layers, including proliferative basal cells and differentiating cells, (2) attachment of basal cells to the dermal equivalent, and (3) a well-defined keratin layer. These three criteria were employed later for histological evaluation of construct viability. For each study (RR, spatial, and FLIM), EVPOMEs were cultured from 5 distinct primary human patient donors to account for intrapatient variability.

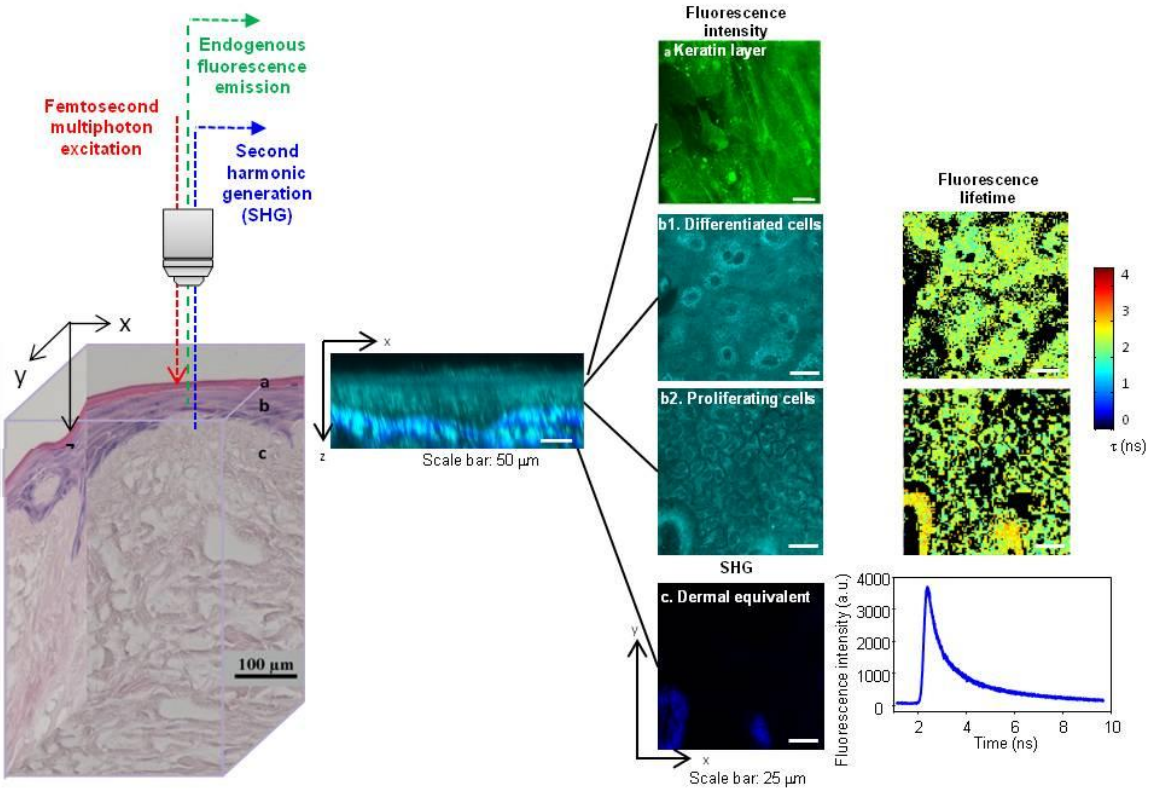

Figure 3.3 Label-free nonlinear optical molecular imaging non-invasively interrogated a living EVPOME construct in three dimensions, measuring cross-sectional (middle) and *en-face* (right) images. Fluorescence intensity, fluorescence lifetime, and SHG microscopic images were acquired to quantitatively assess EVPOME viability (right). Three-dimensional spatially-localized optical measurements interrogated cellular metabolic function and spatial organization (steady-state imaging) as well as cellular microenvironment (FLIM).

3.3.1. Non-invasive optical characterization of tissue structure

Control EVPOMEs were compared to stressed EVPOMEs subjected to sub-optimal culture conditions to reduce their viability (5 batches were thermally-stressed for intensity and FLIM studies, 5 batches were metabolically-stressed for intensity studies). The data collected from the EVPOME constructs are summarized in **Table 3.1**. Optical microscopy captured the layered structure of a living EVPOME construct with cross-sectional NAD(P)H (cyan: greenish-blue) and FAD (green) images overlaid with SHG images (blue) (**Fig. 3.4**), in good agreement with histology sections. As expected, strong fluorescence signals in the NAD(P)H and FAD channels were detected from the top keratin layer and the bottom dermal equivalent layer (*i.e.* extracellular matrix). The top layer fluorescence was attributed to keratin, and the bottom layer fluorescence was attributed to collagen and elastin, since each of these species is known to produce strong fluorescence cross-talk in the emission wavelengths ranges studied [74]. The presence of collagen and elastin in the dermal equivalent layer was confirmed previously with a biochemical assay [75].

Representative control and stressed construct images are shown from (left two columns) the thermal-stress experiment and (right two columns) the metabolic-stress experiment (**Fig. 3.4**). Consistent with the culture protocols, thermally-stressed EVPOMEs did not always have underdeveloped cellular layer thickness (stratification began after constructs were raised to an air-liquid interface on day 4, stressing starting on day 9), while metabolically-stressed EVPOMEs consistently lacked cellular layer formation (stressing starting on day 4).

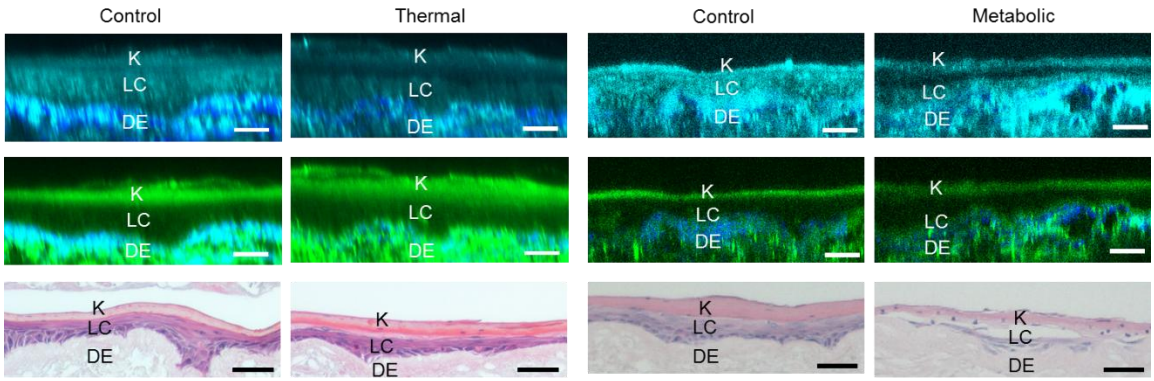

Figure 3.4 Non-invasive optical characterization of tissue structure. Cross-sectional fluorescence images of EVPOME constructs from NAD(P)H (first row, cyan) and FAD (second row, green) channels with overlaid corresponding SHG images (blue) were compared to sample histology. Control and thermally-stressed (left columns) and metabolically-stressed (right columns)) EVPOMEs exhibit the layered tissue structure, consisting of a top keratin layer (K) ~10-20 μm thick, a middle living cellular layer (LC) ~20-30 μm thick, and a bottom dermal equivalent layer (DE) ~400 μm thick (a portion is shown). While fluorescence images quantitatively and non-invasively characterized EVPOME's layered structure, histology destroyed the EVPOME constructs. Scale bar: 50 μm.

3.3.2. 3D imaging of the tissue-engineered construct

A movie was made with optical images acquired from a day 11 living EVPOME. The healthy EVPOME was non-invasively optically sectioned in 3D via label-free nonlinear optical molecular microscopy. 91 *en-face* images with a step size of 1.01 μm were acquired to render the 3D image shown in **Figure 3.5**. The 3D image demonstrates the EVPOME construct from the top side down. The cyan color is from keratin (the bright cyan signals on top of the EVPOME) and NAD(P)H (the dim cyan signals embedded in between the bright keratin signals) and the blue color is from the bottom collagen SHG signals.

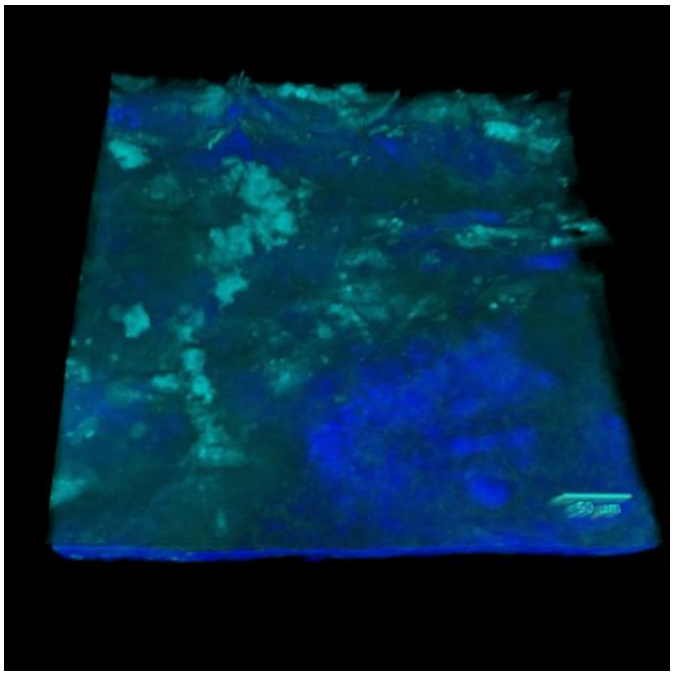

Figure 3.5 *En-face* images were acquired to localize living cells from the living EVPOME. The movie introduces tissue constituents, keratin, NAD(P)H, FAD, and collagen, in each EVPOME layer. The endogenous biomolecules were employed for non-invasive, label-free quantification of tissue spatial organization, cellular metabolism, and tissue microenvironment.

3.3.3. Spatial assessment of local cellular organization

Spatial assessment consisted of two steps: (1) measurements of cellular layer thickness and (2) quantification of cellular organization. EVPOMEs with average cellular layer thickness less than 15 μm (the average thickness of a cellular monolayer) were not candidates for analysis in step (2) and were excluded from further study. (This included three constructs, one control and two stressed, in each of the thermal-stress and the metabolic-stress experiments. Naturally, the absence of cells detected in step (1) is itself a metric of a construct's poor viability.) EVPOMEs with a cellular layer > 15 μm were further analyzed in step (2), where cellular organization was quantified via NAD(P)H

fluorescence images (**Fig. 2.1**). NAD(P)H *en-face* fluorescence images were employed for organizational analysis rather than FAD because of their higher signal intensity and contrast. Spatial intensity analysis employed a point spread density (PSD) map of each image to extract a Hurst parameter (H), related to the cellular organization [70]. The PSD map suggested that the self-affine fractal structure [76] of EVPOMEs was between 2.00 - 7.14 μm, a range consistent with cellular mitochondrial size.

Cellular organization of the differentiating and basal layers of EVPOMEs is shown (**Fig. 3.6**). In the basal layer of control constructs, keratinocytes were closely packed. As basal cells proliferated and some cells differentiated to the upper keratin layer, keratinocytes became less tightly packed with an irregular cellular organization. Disorganized cells were observed in basal layers of both metabolically-stressed and thermally-stressed EVPOMEs.

Smaller H values corresponded to increased cellular disorganization with non-distinguishable cell-to-cell or cell-to-nucleus borders. In control EVPOMEs, the differentiating layer had a smaller H value than the basal layer. Alternatively in thermally-stressed EVPOMEs, both basal and differentiating layers had small H values. The H value difference between the differentiating and the basal layer was found to be significantly larger in control than in thermally-stressed EVPOMEs (**Fig. 3.6b**, after employing the step (1) exclusion criteria above, for 4 control with 11 H value differences and 3 thermally-stressed batches with 8 H value differences, *P*-value = 0.004). In metabolically-stressed EVPOMEs, the H value of the basal layer was significantly lower than that of the basal layer of a control EVPOME (**Fig. 3.6b**, after employing the step (1)

exclusion criteria above, for 4 control with 12 H values and 3 metabolically-stressed batches with 10 H values, *P*-value < 0.001).

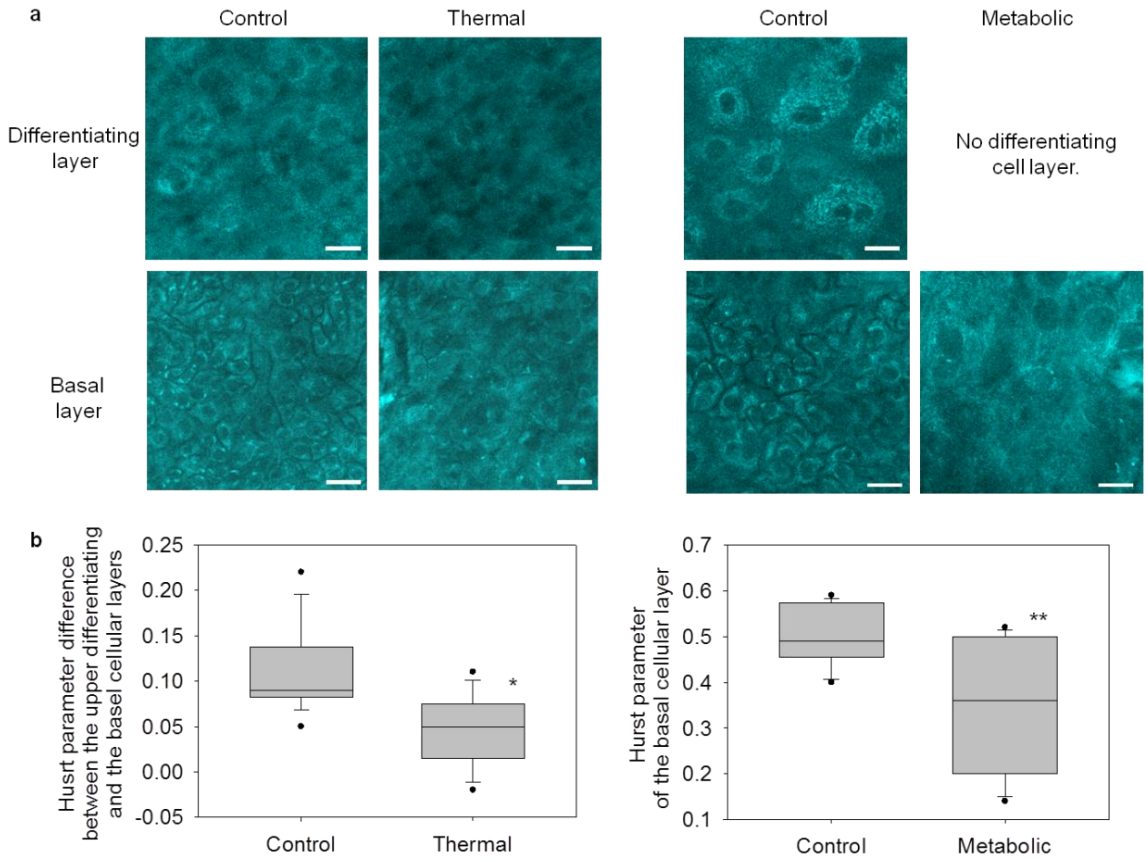

Figure 3.6 Label-free optical spatial analysis characterized cellular organization in EVPOME constructs and reliably distinguished control from stressed constructs. (a) *En-face*, optically sectioned NAD(P)H images revealed cellular organization of the EVPOME constructs. In control constructs, differentiating cells (top) were characterized by large, loosely packed cells. Alternatively, basal layer cells (bottom) were characterized by small, closely packed cells. In thermally-stressed constructs, cell morphologies appeared disorganized in both layers. In metabolically-stressed constructs, EVPOMEs grew thin cellular layers (no distinct differentiating and basal layers). Therefore, only the basal layer image was acquired, which appeared disorganized. Scale bar: 20 μm. (b) Cellular organization was quantified by spatial analysis of optical images to extract a Hurst parameter (H). For both stressing experiments, the Hurst parameter significantly distinguished between stressed and control EVPOMEs. (*after employing the step (1) exclusion criteria, for 4 control with 11 H value differences and 3 thermally-stressed batches with 8 H value differences, *P*-value = 0.004; **for 4 control with 12 H values and 3 metabolically-stressed batches with 10 H values, *P*-value <0.001)

3.3.4. Redox ratio metric assessment of local cellular metabolism

A redox ratio, defined as ([FAD] / ([NAD(P)H] + [FAD]), provides a quantitative metric to compare relative metabolic rates of measured samples. A lower RR corresponds to relatively lower FAD fluorescence and/or higher NAD(P)H fluorescence, indicating a higher cellular metabolic rate [42].

En-face fluorescence images were employed to quantify the relative local metabolic rate via analysis of intracellular autofluorescence variations. The RR metric assessed local cellular metabolism in EVPOME constructs (**Fig. 3.7**). **Figure 3.7a** shows cross-sectional RR maps which exhibit the layered EVPOME structure. Construct metabolic function was assessed via the RR of the cellular (middle) layer. Control constructs had lower RRs than stressed constructs, corresponding to higher cellular metabolic rate. After either thermal or metabolic stressing was applied, RRs of stressed EVPOMEs were higher than RRs of control EVPOMEs. The average redox ratio of control and stressed EVPOMEs was compared (**Fig. 3.7b**). The RR was significantly higher in the thermally-stressed EVPOMEs than in control EVPOMEs (For 5 batches with 30 control and 30 thermally-stressed images analyzed, *P*-value < 0.001). In addition, the RR was significantly higher in the metabolically-stressed EVPOMEs than in the control EVPOMEs (For 5 batches with 30 control and 30 thermally-stressed images analyzed, *P*-value = 0.004). The observations are consistent with previous studies [42].

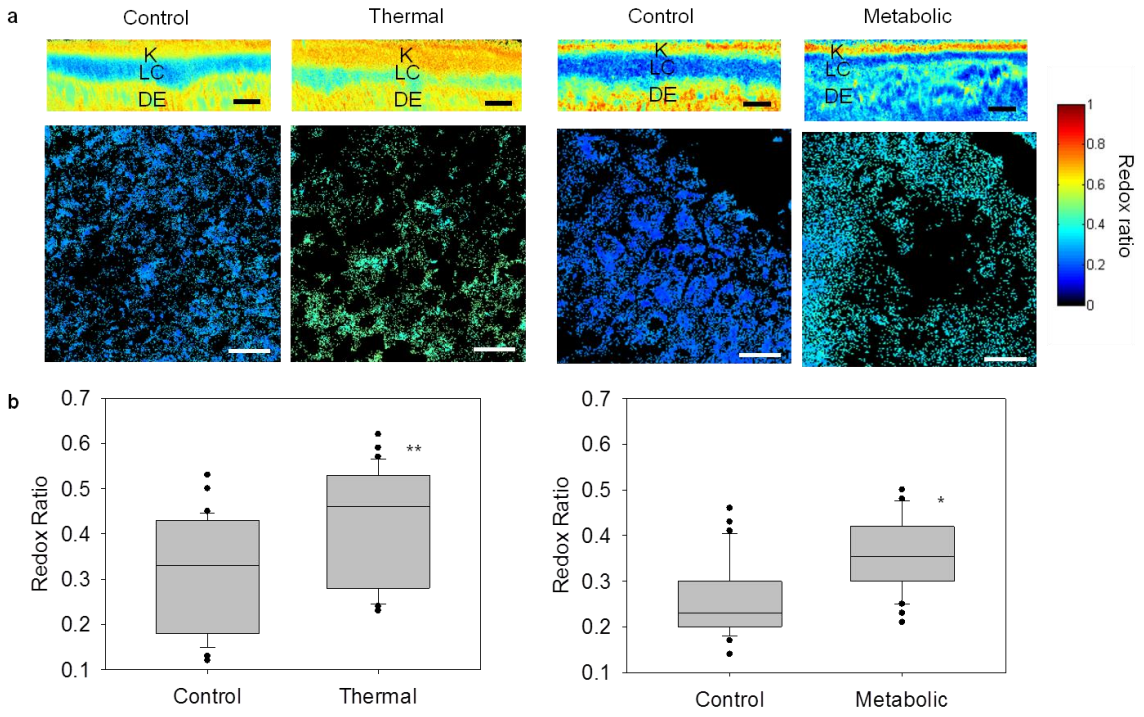

Figure 3.7 Label-free optical redox ratio mapping characterized cellular metabolism in EVPOME constructs and reliably distinguished control from stressed constructs. (a) The top row shows cross-sectional EVPOME redox ratio maps; the bottom row shows *en-face* EVPOME redox ratio maps. Control constructs had a lower RR (deeper blue) than stressed constructs, indicative of viable and actively metabolizing cells. (K: keratin; LC: living cellular; DE: dermal equivalent) Scale bar: 25 μm. (b) An average RR for each image was extracted to quantify cellular viability of thermally-stressed (left) and metabolically-stressed (right) EVPOMEs. Control EVPOMEs had significantly lower RR than stressed EVPOMEs in both experiments. (For 5 batches with 30 control and 30 thermally-stressed images analyzed, **P*-value = 0.004; ** *P*-value <0.001).

3.3.5. Single-channel fluorescence intensity imaging

We note that NAD(P)H or FAD fluorescence images alone cannot significantly distinguish either thermally-stressed (For 5 batches, NAD(P)H *P*-value = 0.43, FAD *P*-value = 0.02) or metabolically-stressed (For 5 batches, NAD(P)H *P*-value = 0.001, FAD *P*-value = 0.14) from control EVPOMEs, as shown in **Table 3.2.**

			Gold Std.	Potential Release Criteria				
Stressing Condition	Sample	N (Batches)	Histology	Glucose	Fluorescence Intensity			
					Intensity			Spatial analysis
					NAD(P)H	FAD	RR	*En face* organization
Thermal	Cells	4	n/a	n/a	0.02	0.03	**0.004**	n/a
	EVPOME	5	**0.002**	0.10	0.43	0.02	**<0.001**	**0.004**
Metabolic	EVPOME	5	**<0.001**	0.03	**0.001**	0.14	**0.004**	**<0.001**

Table 3.2 Summary of statistical tests evaluating the gold standard histology and the potential release criteria: glucose, fluorescence intensity from cells in culture and in EVPOME constructs.

Statistical testing was performed with a linear mixed effects model as described previously. In **Table 3.2**, *P*-values smaller than 0.01 were colored in blue, indicating the metrics significantly distinguished between the control and the stressed EVPOME. *P*-values larger than 0.01 were colored in red, indicating the metrics were not sufficient to distinguish between the control and the stressed EVPOME. Also summarized in **Table 3.2** are the results from cells in standard culture (corresponding to Sec.2.5). The table shows that single-channel fluorescence intensity imaging is not sufficient to distinguish between viable and non-viable cells.

Glucose consumption readings and single channel intensity images were mostly not sufficient to distinguish between control and compromised constructs. This can be attributed to inherent differences between human primary cell donors and their metabolic variability, which are greatly influenced by a variety of factors, including a patient's age, health, and individual metabolic rate. Manufacturing constructs from primary cells creates a wider range of cellular viabilities studied than if immortalized cell lines were employed. This inherent difference can lead to constructs with varying properties, including wider ranges of cell and keratin layer thickness. This variability of tissue layer thicknesses could result in differences in photon delivery and collection that may have impacted intensity measurements.

3.3.6. FLIM assessment of local cellular viability

Figure 3.8a shows representative NAD(P)H intensity and corresponding FastFLIM images of control and thermally-stressed EVPOMEs. While intensity images appear comparable in intensity and spatial organization, the average fluorescence lifetimes measured via FLIM are greater for thermally-stressed constructs compared to controls. The average of all time-resolved fluorescence decays analyzed from thermally-stressed constructs is longer than that from control constructs (**Fig. 3.8b**), similar to results from primary human oral keratinocytes in culture. From each acquired FLIM image, up to two regions void of collagen and keratin were selected and analyzed with bi-exponential fitting. Fitting data to bi-exponential decays yielded two primary fluorophore populations, attributed to free (τ_2, fast lifetime) and bound (τ_1, slow lifetime) NAD(P)H. The percent contribution of τ_1 to the measured fluorescence decay was significantly lower in control

than in thermally-stressed constructs (**Fig. 3.8c**, for 5 batches with 58 control and 33 thermally-stressed regions analyzed, *P*-value < 0.001), consistent with the result after applying oxidative stress to cells [77].

The rapid data analysis method for FLIM, phasor plot, was employed to analyze the FLIM images acquired from control and thermally-stressed EVPOMEs (**Fig. 3.9**). Phasor plot analysis was applied to a whole FLIM image without selecting regions of interest. Thus, one FLIM image results in one point on the phasor plot. The result shows that phasor plot analysis distinguished between thermally-stressed cells (red dots) and control (blue dots) cells (for 5 batches with 31 control and 18 thermally-stressed FLIM images analyzed, *P*-value of the s coordinate = 0.048). It is noted that only the s coordinate showed statistical significance. Neither the g coordinate nor the g/s parameter showed statistical significance. This is because phasor plot analysis was performed without excluding the collagen and keratin contents. Later in Chapter 5, an algorithm employing the error propagation analysis to assist phasor plot analysis will be introduced. The developed algorithm enables automatic exclusion of the signals from the extracellular matrix (keratin and collagen).

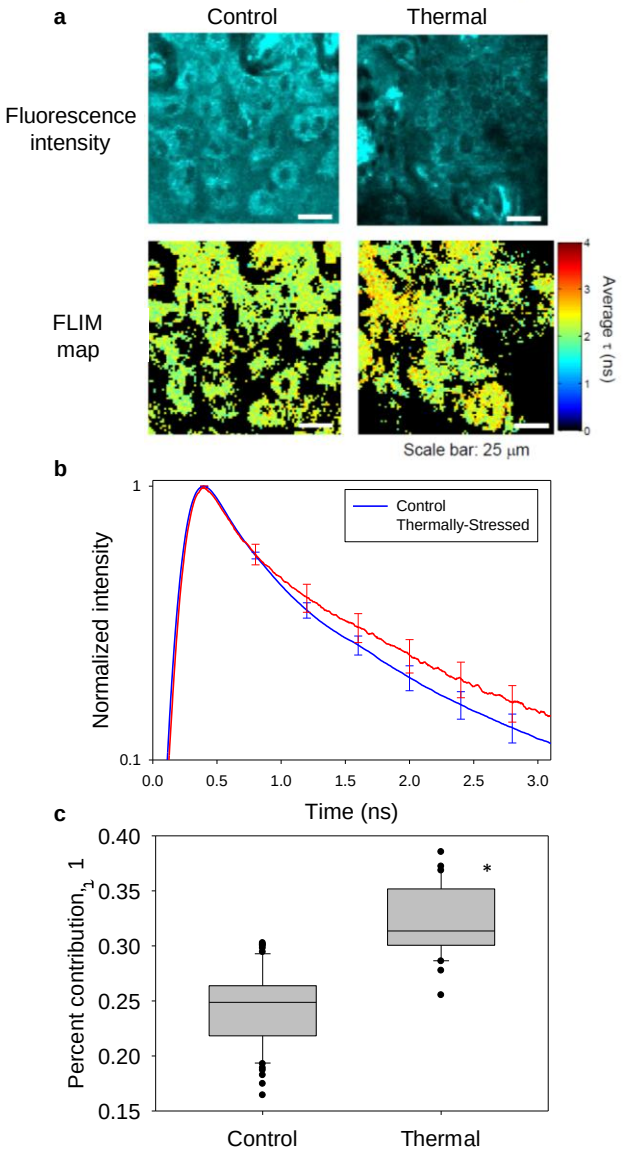

Figure 3.8 Label-free fluorescence lifetime analysis successfully distinguished control from thermally-stressed EVPOMEs. (a) Representative *en-face*, optically sectioned NAD(P)H fluorescence intensity images and corresponding FLIM maps for an analyzed region-of-interest in control (left) and thermally-stressed (right) EVPOMEs. Larger mean fluorescence lifetime τ was observed in FLIM maps of thermally-stressed constructs relative to controls. (b) Mean of normalized fluorescence decays from regions-of-interest support the observation from FLIM maps that thermally-stressed constructs exhibited greater mean NAD(P)H fluorescence lifetimes than controls. Error bars represent SEM (c) NAD(P)H fluorescence decays measured from constructs were best fit to a two-exponential decay model. Model fits revealed that the percent contribution of τ_1 (attributed to bound NAD(P)H) to the measured fluorescence decay was significantly higher in thermally-stressed EVPOMEs than in controls (for 5 batches with 58 control and 33 thermally-stressed regions analyzed, *P*-value < 0.001).

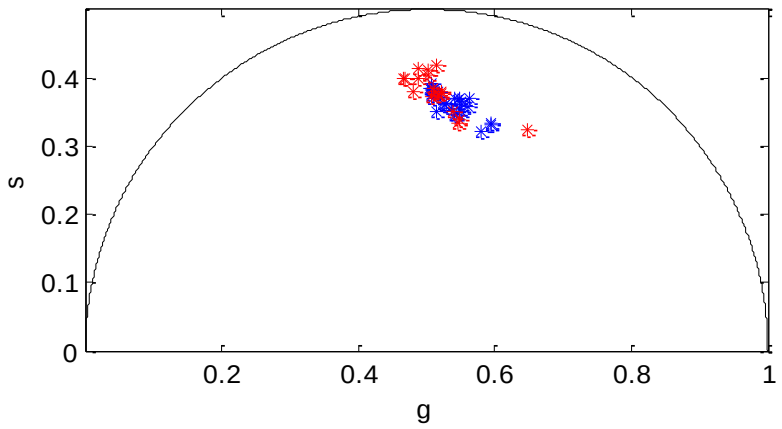

Figure 3.9 Phasor plot distinguished between control and thermally-stressed cells in EVPOMEs (for 5 batches with 31 control and 18 thermally-stressed FLIM images analyzed, *P*-value of the s coordinate = 0.048).

3.4. Optical assessments of differentiation and basal cell layers

In control constructs, optical measures of cellular spatial organization (the Hurst parameter (H)) detected notable differences between living cells populating the basal layer and those populating the differentiating layer (**Fig. 3.6**), whereas optical measures of cellular metabolic function (RR and FLIM metrics) did not detect differences between those layers. Metabolic differences between differentiating and basal cell layers might have been anticipated in cultured constructs because of their different functionalities. However, EVPOMEs are produced *in vitro* in 11 days by seeding hundreds of thousands of proliferating cells (sufficient to create a continuous basal layer) onto the dermal equivalent and the short culture period may be insufficient to produce measurable differences in metabolic function between cell layers. Future optical studies could examine EVPOMEs cultured for longer periods, which exhibit increased cellular maturity

(defined as the number of cell layers/increase in stratification) and amplified differences between the differentiating and basal cells layers [1].

3.5. Assessment via histology and glucose consumption assay

Traditional assessment methods, histology and glucose consumption assay, analyzed the control and stressed EVPOMEs studied (**Fig. 3.10**). Due to the high patient variability, histology could not distinguish stressed from control EVPOMEs in some cases. Histology assessment showed that thermal stressing and metabolic stressing created two different outcomes, with thermally-stressed EVPOMEs having greater perceived viability than metabolically-stressed EVPOMEs (**Fig. 3.4**). However, glucose consumption readings could not distinguish between stressed and control EVPOMEs as shown in **Figure 3.2**.

Histology scores distinguished stressed from control EVPOMEs in some experiments (for 5 batches, (a) P-value = 0.002; (b) P-value < 0.001; (c) P-value = 0.03), but histology is a destructive method for tissue assessment. Percent glucose consumption measures did not well distinguish stressed from control constructs in any experiment ((a) for 5 batches, P-value = 0.1; (b) for 4 batches, P-value = 0.03; (c) for 5 batches, P-value = 0.04). The reading is highly variable as compared to optical metrics and histology scores. The percent glucose consumption measures from the metabolic-stress experiment were larger than those from the thermal-stress experiment because the metabolic-stress culture dishes were smaller.

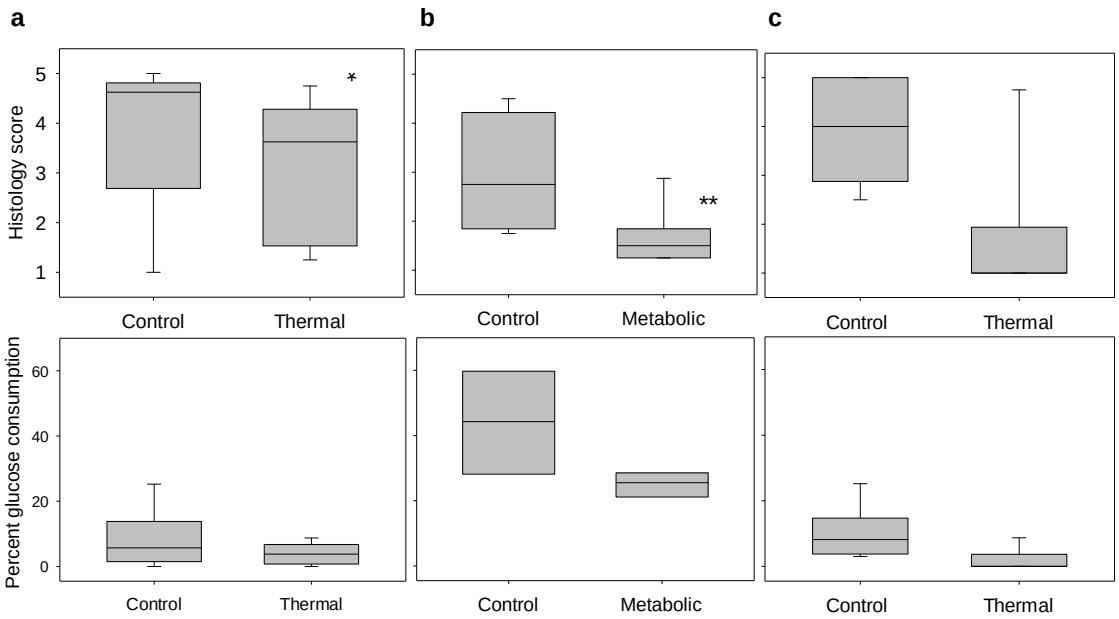

Figure 3.10 Histology scores assigned by a panel of blinded expert readers and percent glucose consumption measures did not reliably distinguish control and compromised EVPOMEs. Histology scores (with higher scores indicating greater perceived viability; 5 being the most viable) and glucose readings (percent error = 15%) compare control constructs to (a) thermally-stressed and (b) metabolically-stressed EVPOMEs prepared for the fluorescence intensity experiment, and (c) thermally-stressed EVPOMEs prepared for the fluorescence lifetime experiment (for 5 batches, *(a) *P*-value = 0.002; **(b) *P*-value < 0.001; (c) *P*-value = 0.03).

3.6. Optical measures non-invasively identified stressed engineered tissues

A robust manufacturing release criterion would identify and eliminate any stressed constructs. Optical redox ratios were compared to histology scoring for the 10 control and 10 stressed constructs assessed by fluorescence intensity (**Fig. 3.11a**, 5 thermally-stressed, 5 metabolically-stressed). A RR threshold value of ~0.23 (dashed black line) successfully distinguished all 10 stressed EVPOMEs, whereas no such threshold value was possible for histology scoring, indicating that redox ratio is a robust release criterion. A comparable histology score threshold capable of distinguishing stressed from control constructs was impossible to define. We note that 3 control constructs with poor mean

histology score (< 2) were also identified by the optical RR threshold. Therefore, excluding these 3 poorly growing EVPOMEs, the non-invasive optical RR metric successfully identified 5 out of 7 remaining control from all 10 stressed constructs.

Similarly, an optical FLIM measure (the percent contribution of τ_1) was compared to histology scoring for the 5 control and 5 thermally-stressed constructs assessed by fluorescence lifetime (**Fig. 3.11b**). A percent contribution of τ_1 threshold of ~0.28 (dashed black line) differentiated all thermally-stressed from all control EVPOMEs, which was not possible using histology scoring. In the *in vivo* study detailed in Sec. 3.7., the histology score > 3 in pre-implant assessment of constructs reliably predicted *in vivo* graft success after 1 week.

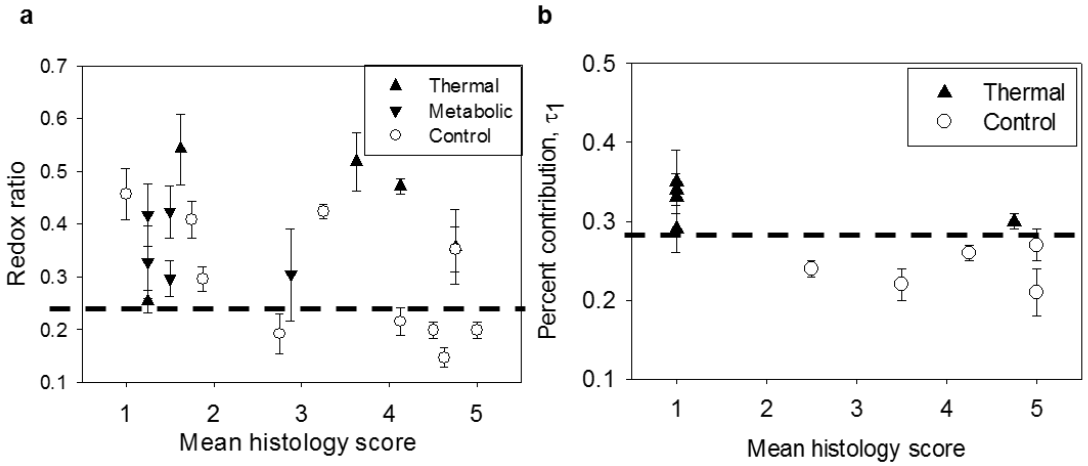

Figure 3.11 Non-invasive optical metrics obtained from label-free (a) redox ratio (RR) and (b) fluorescence lifetime (FLIM) images reliably identified all experimentally stressed tissue constructs, whereas histology scores assigned by a panel of blinded expert readers could not. (a) Mean redox ratio was compared to mean panel histology score for control (10 batches), thermally-stressed (5 batches), and metabolically-stressed (5 batches) EVPOME constructs. (b) FLIM analysis was compared to mean panel histology score for control (5 batches) and thermally-stressed (5 batches) EVPOME constructs. A FLIM threshold (dashed black line) distinguished all 5 stressed constructs from the 5 controls. Error bars represent standard deviation of all measurements from one EVPOME.

3.7. Pre-implantation construct viability to predict post-implantation graft success

Perhaps the best indicator of tissue-engineered construct viability is post-implantation graft integration and vascularization [78-80]. A study on EVPOME constructs implanted in humans [23] indicate that successful grafts are achieved *in vivo* when Day 11 EVPOME constructs are viable, i.e., they contain a well-organized stratified epithelial layer with differentiated cells and a proliferating basal cell layer, as assessed by histology. The *in vitro* work demonstrated the ability of both label-free optical molecular imaging and histological assessments to reliably identify viable constructs prior to implantation. In the following study, EVPOME constructs were implanted into 21 mice for 1 week to further assess the graft success post-implantation.

3.7.1. Study design

On day 11 manufacturing process prior to construct implantation, EVPOMEs were characterized by histological scoring and biochemical assays prior to implantation. Quantitative histological scoring was performed according to the methods described in Sec. 3.2.1. The biochemical assays, ELISA analysis, were performed using the spent culture medium on Day 11. The three constitutively-secreted cytokines of interests were IL-8, hBD-1 and VEGF and were analyzed to characterize pre-implantation construct health.

Five batches of control and thermally-stressed Day 11 EVPOMEs were manufactured with primary human oral keratinocytes from five distinct patients. The EVPOME constructs were implanted into 21 (10 control and 11 thermally-stressed EVPOME

constructs) 7 to 8-week old female severe combined immunodeficient (SCID) mice according to a previously developed protocol [81] for one week. The UM Committee on Use and Care of Animals approved the study protocols. The procedures to implant constructs were reported [82]. Briefly, mice were anesthesized before an incision was made down to the panniculus carnosus to create a skin pouch. The skin pouch house an EVPOME construct with its dermal equivalent side placed onto the animal's muscular fascia. The top keratin layer of the construct was covered with a thin silastic sheet to prevent adherence with the animal skin. The skin pouch was then secured for 1 week.

After one week post-implantation, the skin pouch was opened for optical characterization of graft success [82]. EVPOME constructs were then removed from the mice for the post-implantation histological assessments to determine the graft success.

3.7.2. Post-implantation assessments of the graft success

In the study, both histological assessment (**Fig. 3.12**) and cytokine secretion measures of tissue-engineered constructs prior to implantation in 21 mice reliably predicted graft success *in vivo*, as assessed by post-implantation histology after 1 week. These studies indicate that viable pre-implantation grafts initiate continuous tissue development and successful integration and vascularization at the implant site, underscoring the importance of reliable pre-implantation assessment tools.

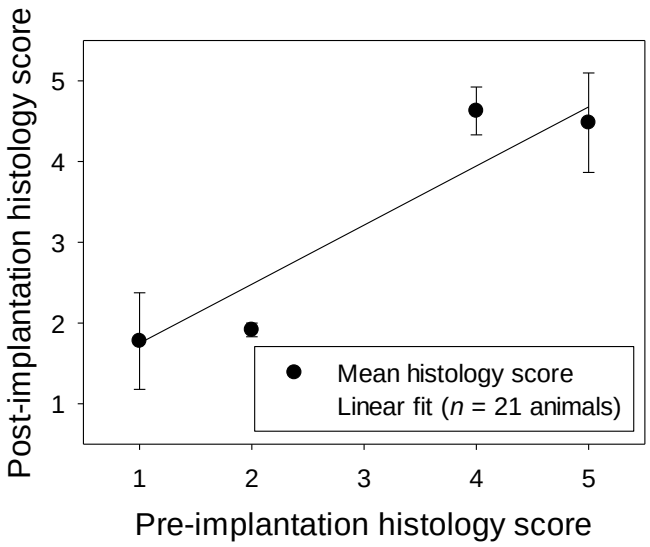

Figure 3.12 In the study for monitoring graft success after implantation, pre-implantation and post-implantation histology scores were compared. The plot shows that the pre-implantation viability monitoring successfully predicted the graft success (21 mice from 5 batches). Pre-implantation histology scores were rounded to the nearest integer. *n* is 6, 2, 0, 4, and 9 for the score of 1-5 respectively. Error bars represent standard deviation of all EVPOMEs in the same category.

3.8. Discussion: the needs of TERM

Importantly, histological examination of thin fixed tissue sections obtained from punch biopsies and read by an expert histology panel is destructive, subjective, and labor intensive [83]. Non-invasive biomolecular assays like glucose consumption and cytokine secretion are global measures that do not provide spatially localized tissue assessment and, in the case of glucose consumption, may be unreliable. In contrast, optical molecular imaging provides a non-invasive assessment tool capable of mapping viability across the engineered construct prior to implantation.

To assure tissue-engineered construct effectiveness and safety, the FDA-approved investigational new drug protocol requires specific and rigorous cell testing and monitoring on the day of product release to assess cell viability [71, 72]. Therefore, the development of reliable, label-free technologies that allow real-time, non-invasive assessment on the tissue, cellular, and molecular levels is required to provide a more complete and accurate description of construct viability both *in vitro* and *in situ*. Nonlinear optical molecular imaging with quantitative analysis provides a rapid, non-destructive, non-invasive, objective, label-free, and spatially-resolved assessment of tissue-engineered construct viability [46, 84-87]. The constructs employed here, EVPOMEs, contained multiple endogenous sources of molecular optical contrast (including keratin, NAD(P)H, FAD, and collagen) that provided cellular and extracellular information on tissue morphology and function for viability assessments.

3.9. Conclusions

Non-invasive optical techniques show the potential to provide manufacturing release criteria that are more robust than the glucose consumption assay. Importantly, the optical methods described for quality control of EVPOME could be of value for other TERM applications. Nonlinear optical microscopy has an intrinsic ability to optically section tissues up to depths of ~1 mm (for near-infrared wavelengths). Therefore, the approach is not limited to EVPOME, but is suitable for other engineered cell-based devices, including engineered skin, heart and bladder tissues [88]. Further, a similar approach could be developed to assess *in situ* the viability and maturation of implanted tissues actively undergoing wound healing.

This work demonstrates that technologies based on label-free nonlinear optical molecular imaging could significantly advance TERM applications by enabling non-invasive analysis of engineered tissues in real-time. Using this approach, reliable adjunctive tools could be developed to provide clinicians with quantitative feedback on engineered construct viability, enabling clinicians to select the healthiest engineered constructs for implantation, thereby improving TERM therapy and enhancing patient care.

Chapter 4 Label-Free Optical Metrics to Assess Rapamycin-Treated Tissue-Engineered Oral Mucosa

Label-free nonlinear optical molecular imaging and quantitative metrics were demonstrated to noninvasively and reliably assess living tissue-engineered human oral mucosa. In this chapter, in addition to applying thermal-stress to severely compromise engineered tissues, we added rapamycin to the medium used to grow the cells that formed one group of engineered tissue constructs and/or the EVPOME constructs. Rapamycin, a specific inhibitor of the mammalian target of rapamycin, maintains primary human oral keratinocytes as an undifferentiated cell population capable of retaining their proliferative capacity [13, 89]. Rapamycin treatment at different culture stages, thus, controls cellular proliferation, thereby creating a range of states of tissue viability (**Table 4.1**). The viability difference between control and rapamycin treated engineered tissues was smaller than that induced by the extreme treatments of thermal and metabolic stress, thus challenging and testing the sensitivity of our detection technology. The viability of control, rapamycin-treated, and thermally-stressed tissues was assessed by quantitative histology scoring, WST-1assay, and label-free optical metrics.

4.1. Study design

A total of ten batches of tissue-engineered constructs manufactured with oral keratinocytes harvested from ten independent patients were included in the study: five batches for the rapamycin experiment and five batches for the thermal-stress experiment. For each batch, one to two constructs were manufactured for each experimental condition. Some experimental conditions, rapa+rapa and c+rapa, could not culture viable constructs, *i.e.* no cells were observed on top of the dermal equivalents by optics and histology, thus excluded from the analysis. The detailed definitions of c+rapa, rapa+c, and rapa+rapa are in Sec. 4.1.1. Tissue-engineered constructs were sectioned for histological assessment. Three batches of the rapamycin experiment and two batches of the thermal-stress experiment were randomly selected for the punch biopsies for the WST-1 assay analysis (**Fig. 4.1**). For each construct, three sites were randomly selected for optical imaging. For each site, one to two optical images were measured at lower and upper depths for the proliferating basal layer and the differentiating cellular layer respectively. Some sites only had one depth imaged because the sites did not grow analyzable upper cellular layers. The study design was expected to create a range of states of tissue viability.

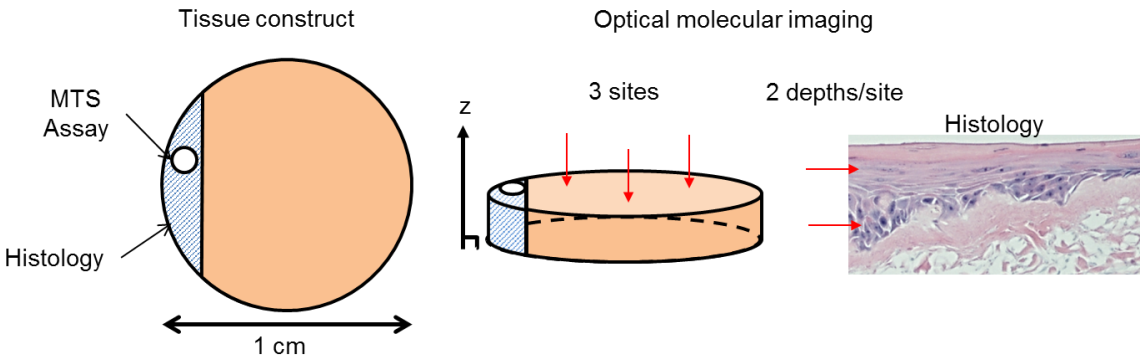

Figure 4.1 Tissue-engineered constructs were developed with varying viability and evaluated with histology, WST-1 assay, and label-free optical molecular imaging. A tissue construct of approximately 1 cm in diameter was sectioned and/or punch biopsied by histology and the WST-1 assay.

Viability Gradient

Experimental Condition	control	*rapa+c	*rapa+rapa	*c+rapa	thermally -stressed
Number of batches	10	5	5	5	5
Number of constructs/ histology	12	6	4	3	5
Number of WST-1 measurements	7	4	2	1	2
Number of optical measurements	64	36	21	15	30

Table 4.1 Experimental design. The color bar indicates the viability gradient. From left to right represents viable (blue) to non-viable (red). *c+rapa: control cultured cells and rapamycin treated engineered tissues; rapa+c: rapamycin pretreated cells and control cultured engineered tissues; rapa+rapa: rapamycin pretreated cells and rapamycin treated engineered tissues. Their details are in Sec. 4.1.1.

4.1.1. Rapamycin treatment protocols

The manufacturing procedure (detailed in Sec. 3.1.2) can be split into two main stages: (1) the cell culture stage and (2) the tissue culture stage. During the cell culture stage, culture medium with 0.06mM calcium was supplied for cellular proliferation. During the tissue culture stage, culture medium with 1.2mM calcium was supplied to induce cellular differentiation. 2nM rapamycin treatment was done at either the cell culture stage, the tissue culture stage, or both, resulting in 4 experimental conditions as shown in **Table 4.1** and below:

1. control: no rapamycin was added to the cultures during the two stages.

2. c+rapa: no rapamycin was added to the first cell culture stage medium; rapamycin was added to the second tissue culture stage medium.

3. rapa+c: rapamycin was added to the first cell culture stage medium; no rapamycin was added to the second tissue culture stage medium.

4. rapa+rapa: rapamycin was added to the medium used in both the culture stages.

4.1.2. WST-1 cellular viability assay protocols

As shown in **Figure 4.1**, a punch biopsy of approximately 3 mm in diameter was taken from the 1 cm in diameter tissue-engineered construct for the WST-1 assay. A section was sliced across the construct, near the edge, fixed in 10% phosphate buffered formalin, and embedded in paraffin for H&E histology and Ki-67 immunofluorescence (IF) imaging. The remainder of the construct was used for assessment by the optical metrics.

The cell proliferation assay was performed by adding 10 μl/well cell proliferation reagent WST-1 to the punch biopsied engineered tissues and incubated for 4 hours at 37°C and 5% CO_2. Then, the sample was shook thoroughly for 1 min on a shaker. The absorbance of the samples was measured against a background control as blank using a EPOCH Biotech microplate reader. The reference wavelength was more than 600 nm.

4.1.3. Immunofluorescence imaging protocols

Paraffin sections of the engineered tissues were first cut on a microtome and heated for 20 minutes at 65^{o}C. Slides were deparaffinized in Xylene with three changes of 2 minutes each. Slides were then rehydrated through graduated alcohols of 2 minutes each and end in tap water (100% alcohol, 95% alcohol, 70% alcohol, water). Slides were then placed in buffer until ready to begin IF staining.

Antigen retrieval (AR) steps were performed in the Biocare Decloaking Chamber before the staining**:** the slides was placed in Citrate Buffer (pH = 6.0) at 125^{o}C for 40 seconds, 95^{o}C for 10 seconds, and 10 minute of cool down in solution on countertop.

Immunoperoxidase staining was performed on the DAKO AutoStainer at room temperature with the following steps:

1. Peroxidase block for 5 minutes
2. Buffer rinse
3. Primary Antibody: Ki67 (dilution: 1:200, ab16667, Abcam) for 1 hour
4. Buffer rinse
5. Secondary antibody (rabbit HRP polymer, #RMR622, Biocare) for 30 minutes
6. Buffer Rinse
7. DAB Chromagen for 5 minutes
8. Sparkle DAB enhancer (#DS830G, Biocare) for 1 minute
9. Water rinse

10. Hematoxylin Counterstain (dilution: 1:10, #CATHE-M, Biocare) for 1 minute
11. Water Rinse
12. Dehydrate slides for 2 minutes at each step of 70% alcohol, 95% alcohol, and 100% alcohol
13. Xylene with three changes for 2 minutes each.
14. Coverslip

Antigen retrieval, antibody concentration, antibody incubation time and DAB incubation time directly affect the stain intensity. Changing any or all will alter the staining specificity. The IF stained sections were sent to University of Michigan Unit for Laboratory Animal Medicine Pathology Cores for Animal Research for the IF imaging.

4.2. Histological assessment correlated to the WST-1 measures

Histological assessments assessed tissue morphology, reliably evaluating engineered tissue viability for the extreme cases [90]. WST-1 assay directly evaluates tissue's functionality by measuring cellular mitochondrial activity. The two methods were employed and compared to characterize tissue-engineered constructs with a range of states of tissue viability. The viability difference between tissue-engineered constructs is expected to be smaller than the extreme cases.

Figure 4.2 shows the comparison between the histology scores and the WST-1 measures, independent of experimental conditions. The plot demonstrates a positive correlation (5 batches with 16 constructs, *P*-value < 0.001), indicating that the WST-1 measures, like histological assessment, reflects tissue viability: the high WST-1 measures indicates the high tissue viability.

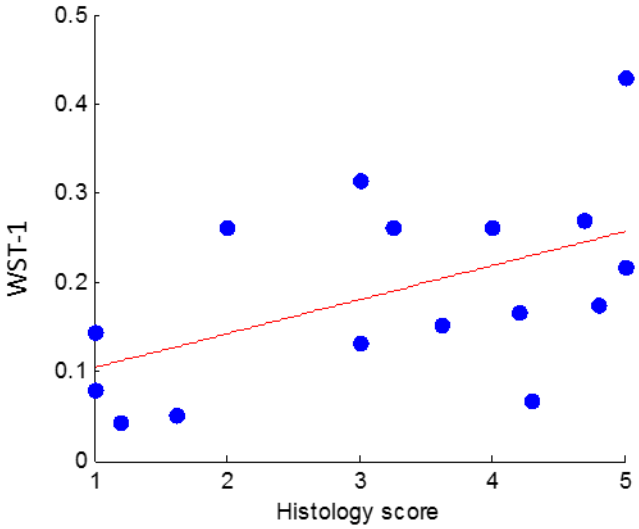

Figure 4.2 Tissue viability was assessed by quantitative histology scoring and WST-1 assay. The plot shows that the two metrics had a significant positive correlation (*P*-value = 0.015 for 5 batches with 16 tissue constructs).

As described in Sec.3.2.1, quantitative histology scoring requires a panel of experts. In contrast, WST-1 assay provides quantitative measures, thus having the advantage of being objective and easy to perform. However, both methods are destructive and the analyzed engineered tissues can no longer be used for implantation.

4.3. Histology assessment of rapamycin-treated tissue-engineered constructs

Quantitative histology scoring was performed to assess rapamycin-treated tissue-engineered constructs. Two groups of cultured cells were identified: well-growing culture and poorly-growing culture. The poorly-growing culture was separated from the well-growing culture because its control tissue-engineered construct, expected to grow well, grew poorly. The well-growing and the poorly-growing cell cultures were defined by their control histology scores. A control score > 3 is defined as well-growing. A control

score <= 3 is defined as poorly growing. The representative control histology sections were shaded in blue as shown in **Figure 4.3**. The two images respectively show a representative well-growing batch and a poorly-growing batch with their corresponding histology scores. In the same two batches, their drug-treated tissue-engineered constructs were shown below their control constructs in the green-shaded region.

For the well growing batch, viable tissue growth was observed from all of the four constructs. There is no obvious difference between constructs and their histology scores are all high (> 3). Alternatively for the poorly-growing batch, the overall tissue viability appears non-viable. The control construct had a broken structure with thin cellular and keratin layers. Poor growth was observed from control, c+rapa, and rapa+rapa constructs (histology score <= 3). However, the rapa+c construct shows high viability with distinct cellular and keratin layers (histology score = 4.7). The result indicates that the rapamycin treatment during the cell culture stage could improve the poor culture.

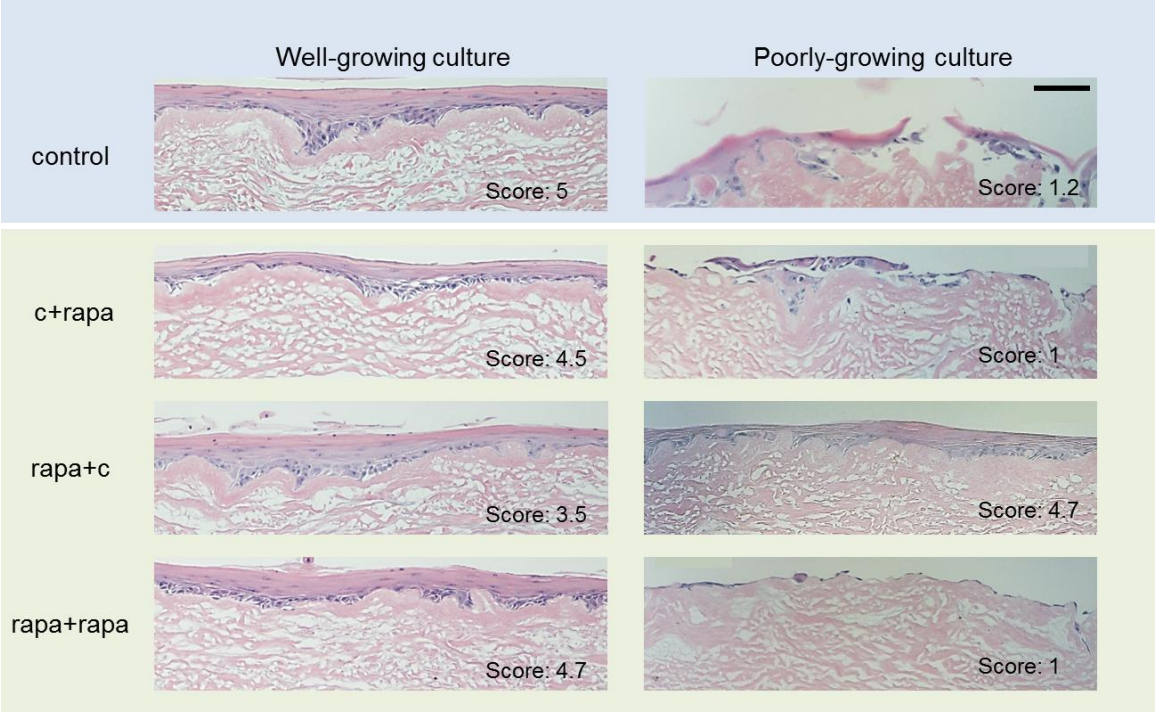

Figure 4.3 Histology of two representative batches of tissue-engineered constructs: one in well-growing culture (left) and one in poorly-growing culture (right). The well-growing and the poorly-growing were defined by their control histology scores. A control score > 3 is defined as well-growing. A control score <= 3 is defined as poorly growing. Scale bar: 100 μm.

4.4. IF histology assessment of rapamycin-treated EVPOME constructs

Histology sections assessed tissue morphology. Ki-67 stained IF histology assessed cellular functionality, similar to WST-1 assay. Ki-67 is a biomarker for tissue proliferative capacity. **Figure 4.4** shows IF histology sections for a well-growing batch and a poorly-growing batch, defined with their control histology scores. The nuclei stained in dark brown in the tissue construct basal layers indicate high Ki-67 expression, thus highly proliferating basal cells from these tissue constructs. The well-growing batch had numerous positive dark brown stained nuclei in all of the four tissue-engineered constructs. Alternatively, the poorly-growing batch had the most Ki-67 expression in the

rapa+c construct. The other constructs in the poorly-growing batch had relatively few dark brown nuclei.

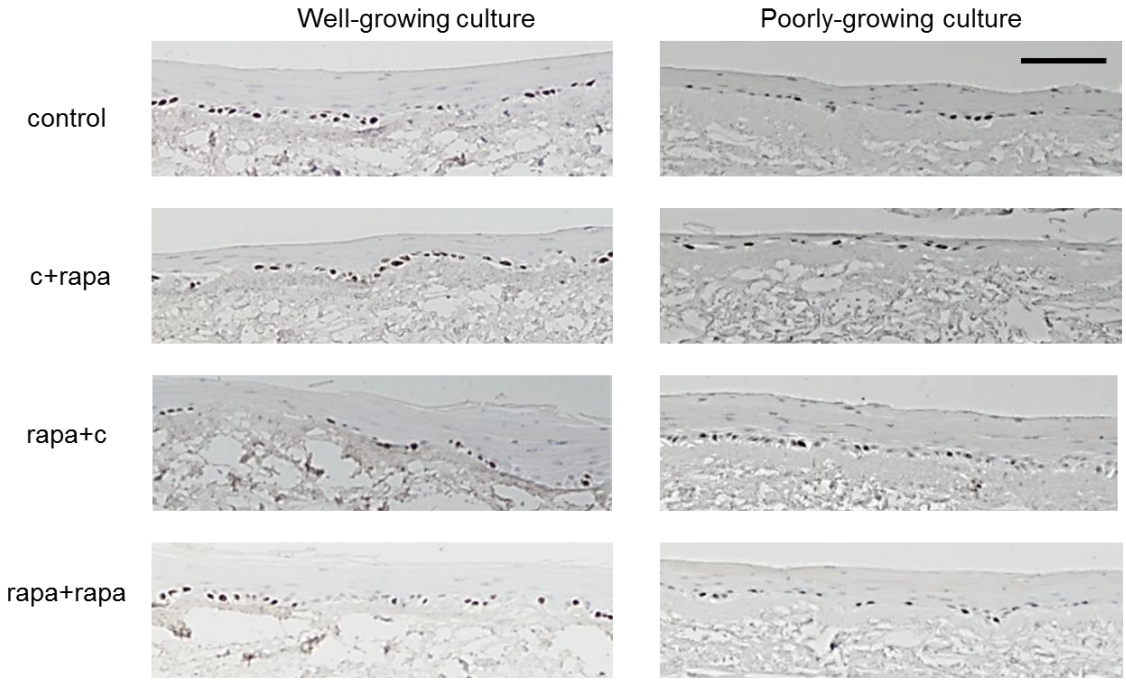

Figure 4.4 Ki-67 immunohistological staining was performed to characterize rapamycin-treated tissue-engineered construct's functionality for one batch in well-growing culture (left) and one batch in poorly-growing culture (right). Scale bar: 100 μm.

4.5. Optical metrics correlated to the WST-1 measures

Label-free optical molecular imaging characterized a construct's functionality by assessing its cellular metabolism with the redox ratio (RR = [FAD]/([NAD(P)H] + [FAD])) metrics. **Figure 4.5a** shows optical images and their corresponding RR maps of one control and one rapa+c construct. The optical images were overlaid with two channels: cyan fluorescence mainly from NAD(P)H and collagen, and SHG solely from collagen. The collagen signals were removed from the fluorescence images to calculate a

RR map. The RR maps demonstrate that the rapa+c construct had a lower RR (greenish) than the control construct (yellowish).

RR metrics monitored cellular metabolism and WST-1 measures monitored mitochondrial activity, both analyzing cellular functionality. The two metrics were compared (**Fig. 4.5b**) and the result indicates that the two metrics significantly correlated. The higher the WST-1 values for absorption, the lower the RR metrics (*P*-value < 0.001 for 5 batches with 16 constructs and 88 optical measurements). The plot was color coded with experimental conditions. There are six categories: two controls separated by their histology scores (score > 3 is the well-growing and score <=3 is the poorly-growing) and four rapamycin treatment experimental conditions. All the control constructs had comparable RRs and WST-1 measures. Some of the control constructs grew weakly, defined as the poorly-growing batches (blue circles). Other control constructs grew well (blue dots). The thermally-stressed constructs (red circles) had the highest RRs and low WST-1 measures, indicating their low tissue viability as expected. Rapamycin treatment improved the tissue viability as shown by higher WST-1 measures and lower RR metrics of the rapamycin treated constructs (green and black dots).

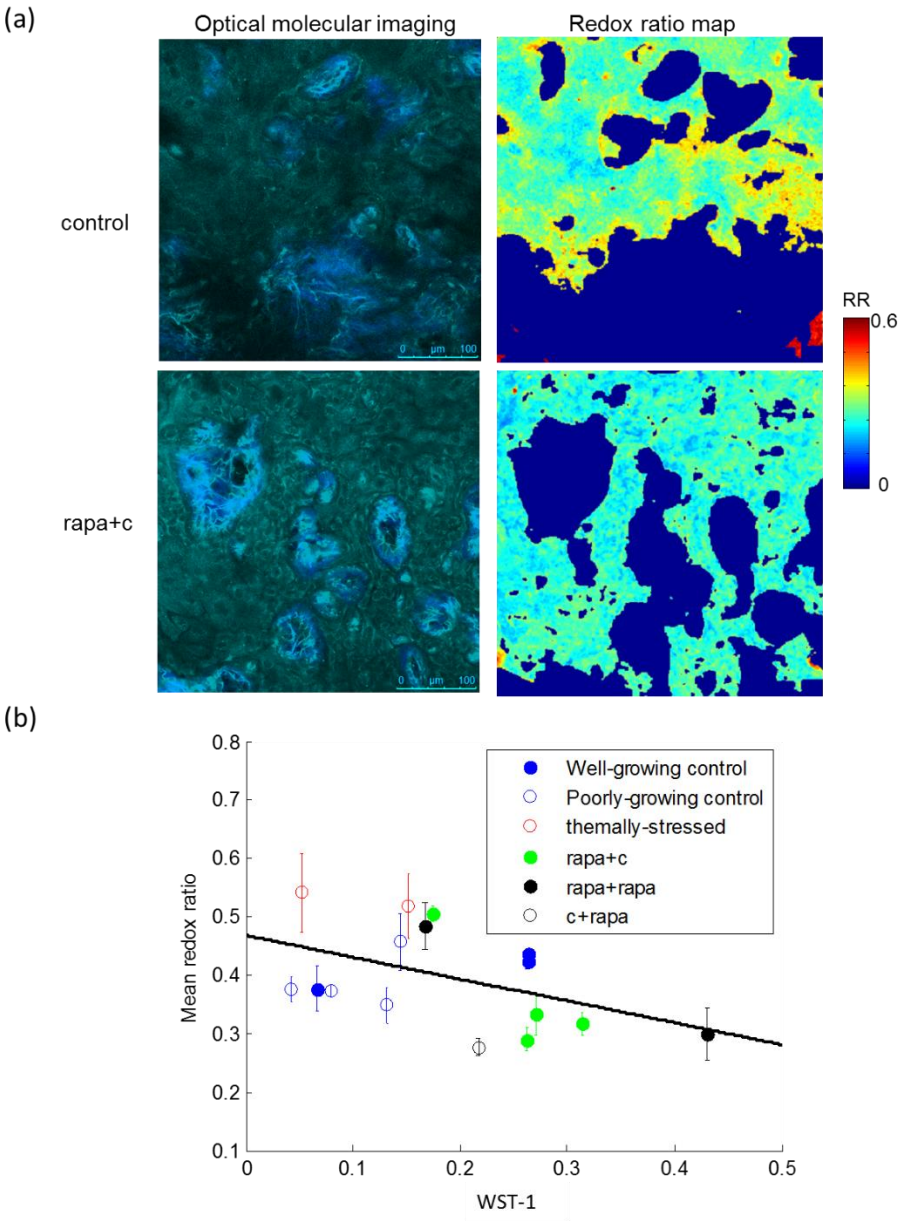

Figure 4.5 Label-free optical molecular imaging non-invasively characterized local engineered tissue viability, correlating to WST-1 assay. (a) The optical images show intracellular NAD(P)H and dermal equivalent fluorescence in cyan, and SHG collagen signals in blue. The RR maps excluded dermal equivalent signals, assessing cellular metabolism by quantifying the relative amount of NAD(P)H and FAD in cells. The rapa+c construct had lower RRs than the control construct, indicating its higher metabolic activity. (b) RR metrics significantly correlated to the WST-1 measures (*P*-value < 0.001 for 5 batches with 16 constructs and 88 optical measurements). The higher the WST-1 measure, the lower the RR metrics. Error bars show standard deviations.

4.6. Assessment of tissue-engineered constructs with rapamycin treatment during the cell culture stage

Rapamycin-treated tissue-engineered constructs (rapa+c, c+rapa, and rapa+rapa) were compared to the control construct. Five batches of tissue-engineered constructs were manufactured. Two batches (the well-growing batches) were excluded from the comparison because all the constructs showed high viability. As shown in **Figures 4.3 & 4.4**, rapamycin treatment did not change the tissue viability of well-growing batches because all the tissue-engineered constructs grew well. Therefore, three poorly-growing batches were examined as shown in **Table 4.2**.

Batch (Patient)	9		10		17	
Experimental Condition	control	rapa+c	control	rapa+c	control	rapa+c
Number of engineered tissues/histology	2	1	2	2	1	1
Number of optical measurements	12	6	5	12	6	6
Number of WST-1 measurements	2	1	2	2	NA	NA

Table 4.2 Batches included for the comparison between control and rapamycin-treated EVPOM constructs and the number of measurements.

Rapamycin treatment during the cell culture stage (before the tissue culture) was found to significantly enhance the construct viability of the poorly-growing batches (**Fig. 4.6**). The box plots show that rapa+c constructs had higher WST-1 measures (*P-value < 0.001 for

2 batches with 4 measurements from the control and 3 measurement from the rapa+c constructs), lower redox ratios (*P-value < 0.001 for 3 batches with 23 measurements from the control and 24 measurements from the rapa+c constructs), and higher histology scores (P-value = 0.002 for 3 batches with 5 measurements from the control and 4 measurement from the rapa+c constructs) than the control constructs. The high WST-1 measures indicate the improved mitochondrial activity. The low redox ratios indicate improved cellular metabolism. The high histology scores indicate improved tissue growth. The three metrics all demonstrate that the rapa+c constructs had better tissue viability than the control constructs in the poorly-growing batches. Therefore, rapamycin treatment during the cell culture stage could improve the viability of tissue-engineered constructs in poor culture. Statistical analysis was performed on the patient level as detailed in Sec. 3.2.4.

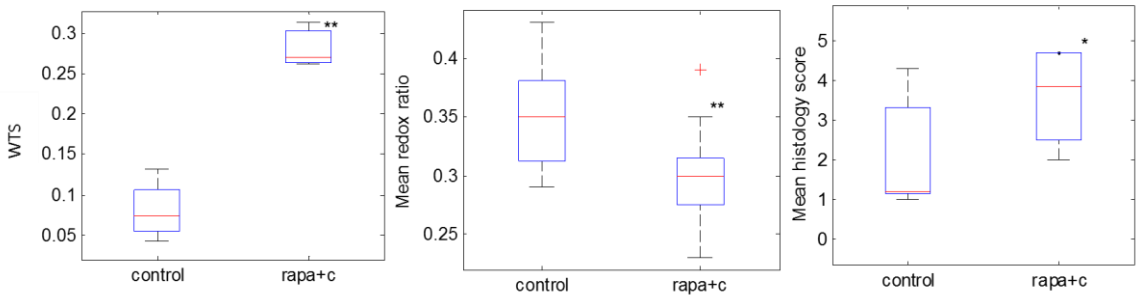

Figure 4.6 Rapamycin treatment during the cell culture stage improved the tissue viability of poorly-growing batches measured by WST-1 (**P-value < 0.001 for 2 batches with 4 measurements from the control and 3 measurement from the rapa+c constructs), optics (**P-value < 0.001 for 3 batches with 23 measurements from the control and 24 measurements from the rapa+c constructs), and histology (*P-value = 0.002 for 3 batches with 5 measurements from the control and 4 measurement from the rapa+c constructs) .

4.7. Spatial selectivity of label-free optical molecular imaging

In addition to viability assessment, label-free optical molecular imaging demonstrated its spatial selectivity. In poorly-growing batches, relatively high variation of tissue growth within one tissue-engineered construct is expected. **Figure 4.7a** (top) shows a histology section with half well-growing site (right) and half poorly-growing site (left). This control engineered tissues was scored 1.2 because of the poorly-growing site. Thus, the batch was defined as a poorly-growing batch.

Label-free optical molecular imaging non-invasively monitored the tissue's viability variation at different spatial sites. In **Figure 4.7a** (bottom), the left optical image shows a thin layer of cells atop the dermal equivalent layer. The right optical image shows the full three layers observed in viable tissues.

The rapa+c construct in the same batch, however, demonstrated a viable tissue construct (**Fig. 4.7b**). The rapamycin treatment during the cell culture stage was observed to improve the cells when grown in tissue culture. Both the rapa+c construct's histology section and optical images exhibit full, uniform, and thick cellular and keratin layers, indicating its good viability. Although histology shows local viability variation, the assessment is limited to the number of sites sectioned due to its invasiveness. In contrast, label-free optical molecular imaging can be non-invasively performed at multiple sites in real time, demonstrating its spatial selectivity.

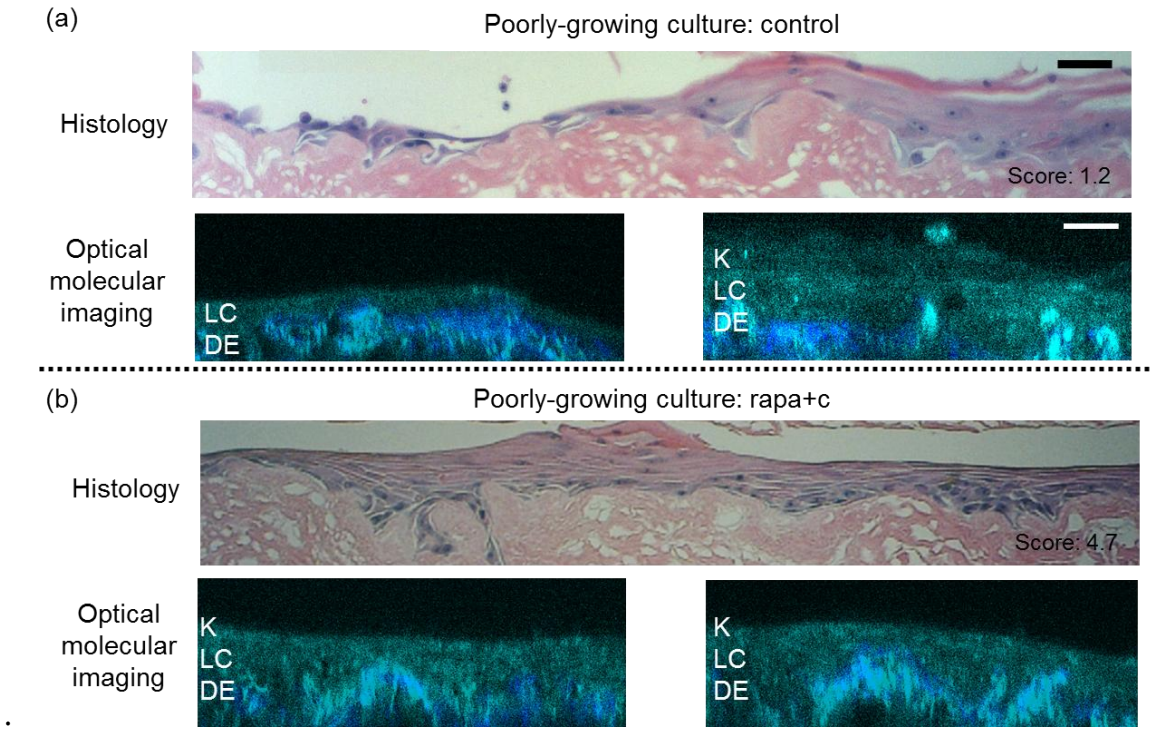

Figure 4.7 Histology and label-free optical molecular imaging characterized tissue morphology, demonstrating their advantage of spatial selectivity. (a) In a poorly-growing culture, a control construct would have inhomogeneous tissue growth. (b) For the same batch, the rapa+c construct shows a well-growing tissue with intact layered structure in the histology section and in the optical images. Two optical channels were overlaid: the cyan channel for tissue fluorescence and the blue channel for dermal equivalent collagen. K: keratin layer; LC: living cellular layer; DE: dermal equivalent layer. Scale bars: 100 μm.

4.8. Conclusions

In Chapter 3, histological assessment was shown to reliably assess engineered tissues. The study design was for the extreme cases, thermal-stressing and metabolic stressing, which compromised the tissue-engineered constructs. In this chapter, a range of states of tissue viability was created with rapamycin treatment. The viability difference between engineered tissues became smaller than the extreme cases, thus more challenging to detect.

Rapamycin-treated engineered tissues were assessed by histology scoring, WST-1 assay, and optics. WST-1 assay was employed because the assay analyzed intracellular mitochondrial activity, similar to the optical RR metrics. Our result shows that WST-1 measures correlated to histology scores, indicating the method could reliably assess engineered tissues.

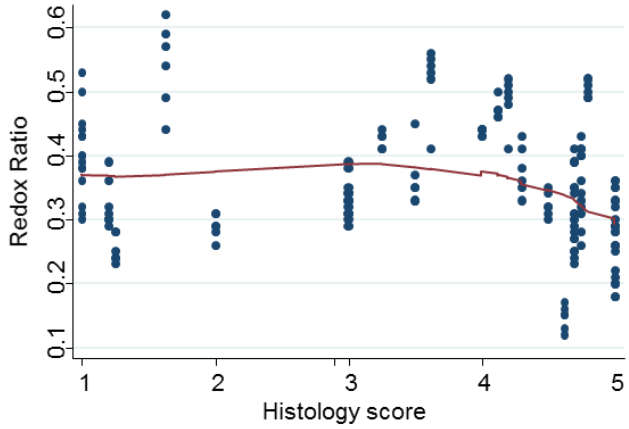

Figure 4.8 Optical metrics were compared to histology scores. The two metrics show a negative correlation (P-value = 0.007 for 10 batches with 30 tissue-engineered constructs and 166 optical measurements). The red line indicates the fitted result of the linear mixed effect model.

WST-1 measures were compared to the optical metrics. The two metrics show high correlation because the two methods monitored the same object, cellular functionality. Histology scores were also compared to optical metrics (**Fig. 4.8**). The plot shows the two metrics correlated in higher ranges of histology score (lower ranges of RR) (*P*-value = 0.007 for 10 batches with 30 tissue-engineered constructs and 166 optical measurements). These results indicate that histology, WST-1 assay, and optics correlated. The sensitivity of optics to tissue viability shown in this study further supports that label-

free optical molecular microscopy could provide manufacturing release criteria of engineered tissues prior to implantation.

In addition, label-free optical molecular imaging demonstrated its spatial selectivity. Histology provides some local spatial information. However, the method is destructive, thus the number of assessments is limited. In contrast, label-free optical molecular imaging can be noninvasively performed for multiple times at multiple sites in tissues. The method is beneficial for engineered tissues manufactured in large scale (10 cm x 10 cm). When manufacturing such engineered tissues, non-uniformity is expected. The center of the tissues is usually more viable than the edge of the tissues.

In this study, the results further demonstrated the sensitivity of label-free optical metrics with the successful assessments of tissue-engineered constructs with a range of states of viability. The assessments correlated to WST-1 assay and histology scoring. Label-free optical molecular imaging noninvasively, quantitatively, and reliably assesses tissue-engineered constructs with spatial information, assisting in selecting the most robust engineered tissues for implantation.

Chapter 5 Error Analysis for Phasor Plot of Time-Domain Label-Free Fluorescence Lifetime Images to Visualize Tissue Constituents

Phasor plot analysis is based on well-established procedures originally developed to analyze dielectric relaxation experiments, *i.e.* a sample's transient responses to repeated perturbations [91]. In fluorescence, this method was applied to analyze frequency-domain fluorescence lifetime imaging microcopy (FLIM) data, as the modulated excitation light is the perturbation and the fluorescence emission is the relaxation. Phasor analysis was further developed to offer a simple, graphical, and rapid algorithm for interpreting frequency-domain FLIM data that were obtained after single excitation frequency from samples exhibiting more than one fluorescence lifetime. In frequency-domain experiments, phasor analysis transforms the modulation, M, and the phase, φ, of the emission with respect to the excitation into

$$g = M\cos\varphi \tag{1}$$

and

$$s = M\sin\varphi. \tag{2}$$

A pair of g and s values represents a phasor vector on the phasor plot. Phasor plot analysis has become a commonly employed tool for interpreting frequency-domain FLIM data [50, 51].

In recent years, phasor plot analysis was adapted to analyze time-domain FLIM images; compared to traditional exponential fitting, advantages include real-time analysis of multiple fluorophores in complex samples, such as biological samples. FLIM-FRET donor and accepter trajectory was visualized on the phasor plot [52]. Cellular metabolism changes [92-94] and differentiation stages [77, 95] were monitored on the phasor plot. It was further developed to analyze steady-state fluorescence spectrum to distinguish multiple species in biological samples [96].

Thorough analysis of such samples requires unbiased, quantitative assessment of contributing fluorophores and outliers. In this chapter, we quantified phasor plot uncertainty through error propagation of noise in time-domain FLIM. Uncertainty of phasor coordinates was calculated by introducing Poisson noise with modeled single exponential decays. Then, phasor analysis was employed with TCSPC-FLIM data of biologically-relevant fluorophores to successfully segment different fluorescent species in tissue-engineered constructs. Furthermore, the method assisted in assessing tissue viability by excluding unwanted signals from extracellular matrices when assessing cellular viability. Such quantitative uncertainty analysis is the first step towards automated visualization and interpretation of phasor plots.

5.1. Phasor plot analysis

FLIM images are 3-dimensional, consisting of spatial (x, y) and temporal (t) information. Traditional analysis method is to employ exponential fitting that is complicated and computational expensive. Phasor plot analysis avoids complicated exponential fitting procedures and does not require prior knowledge of the biological samples such as number of components for the exponential fitting. Time-domain FLIM can be analyzed with phasor analysis because the excitation pulse frequency can be transformed into phasor space similarly to the sinusoidal excitation frequency of frequency domain FLIM. To provide an instantaneous (excluding complex exponential fitting procedures) view of the fluorescence decay in time-domain experiments, the frequency-domain FLIM phasor plot analysis was modified [52]. Fluorescence decays, $F(t)$, at each pixel of an image were transformed into a phasor domain by

$$g = \frac{\int_0^\infty F(t)\cos(\omega t)\,dt}{\int_0^\infty F(t)dt} \tag{3}$$

and

$$s = \frac{\int_0^\infty F(t)\sin(\omega t)\,dt}{\int_0^\infty F(t)dt}, \tag{4}$$

where ω = laser repetition angular frequency. Each pixel of the image is transformed to a point, described by the coordinates g & s on the phasor plot. If the fluorescence decay is single exponential, the coordinates g and s become

$$g = \frac{1}{1+(\omega\tau)^2} \tag{5}$$

and

$$s = \frac{\omega\tau}{1 + (\omega\tau)^2}. \quad (6)$$

These two coordinates lie on a semicircle of a phasor plot (as plotted in **Figs. 5.1-5.5**). If the fluorescence decay is multi-exponential, the phasor point lies inside the semicircle.

The analysis is performed by observing clustering of pixels in specific regions of the phasor plot, providing a graphical view of FLIM images. The method can also be used in a reciprocal mode in which each point of the phasor plot is mapped, and pseudocolored, to a pixel of the image. Since every molecular species has a specific phasor vector, located in specific regions, users can identify molecules by their position on the phasor plot. Therefore, the phasor plots analysis makes the interpretation of FLIM data accessible to the nonexpert.

5.2. Error analysis of phasor plots

Phasor plot analysis was applied to TCSPC-FLIM images to rapidly characterize living cells and engineered tissues (**Fig. 5.1**). Before analyzing, FLIM images were binned to obtain sufficient signals per pixel to analyze. The binned FLIM images were transformed to the 2-dimensional phasor plots. Each binned pixel creates one point on the phasor plot, resulting in a spread of points indicating the lifetime distribution (black dots in **Fig. 5.1**). The phasor plots with black dots are the magnified version of the phasor plots in color to provide a better view of the phasor distribution. The color phasor plot demonstrates the weight of the certain fluorescence lifetime, accumulated by the number of points. The red

color indicates a large number of points and the blue color indicates a small number of points. The semicircle represents single-exponential decays.

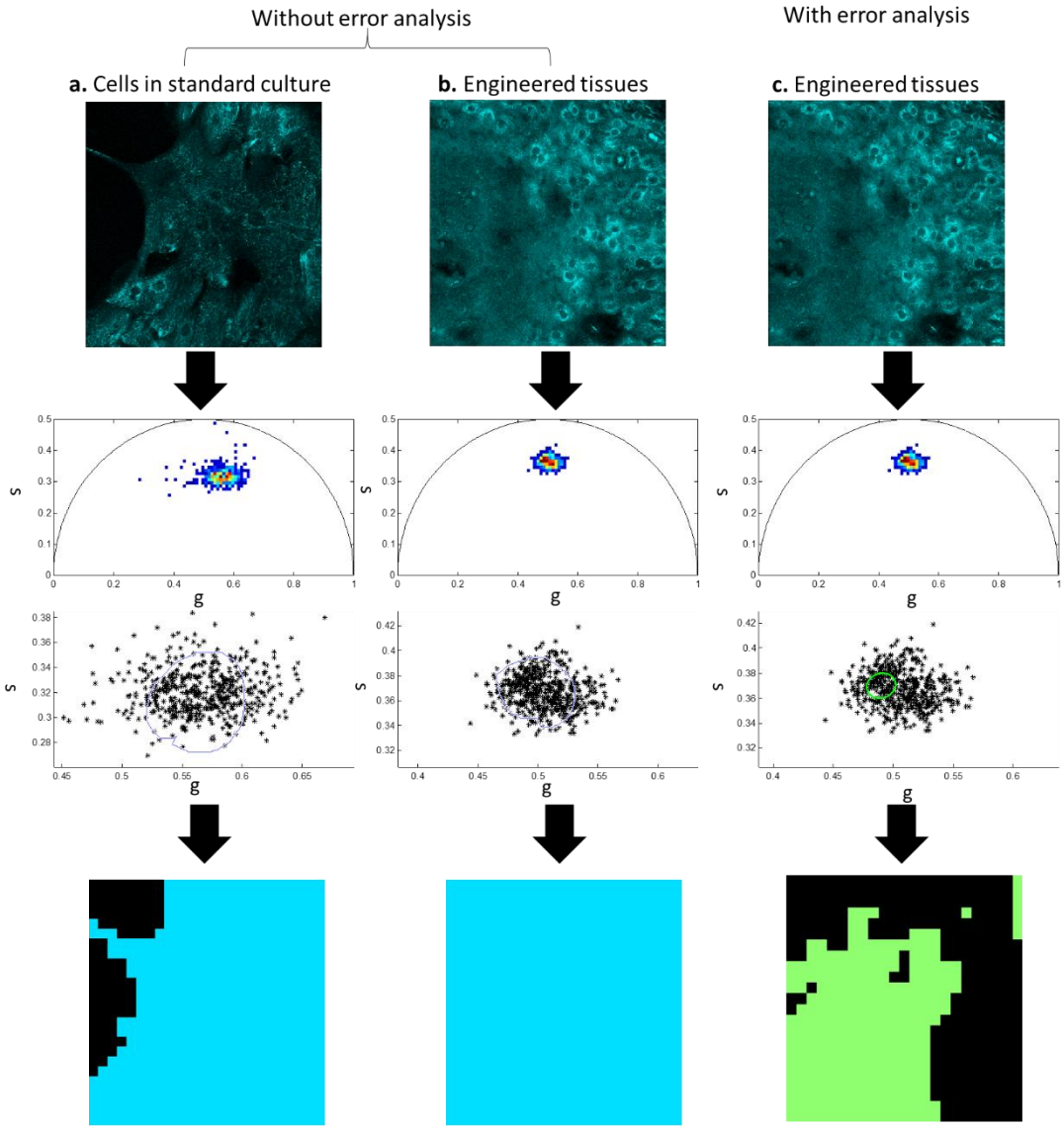

Figure 5.1 Phasor plots (a,b) without and (c) with error analysis characterized TCSPC FLIM images of (a) cells in standard culture and (b,c) engineered tissues.

To pseudocolor the intensity map, regions of interest within the lifetime distribution need to be selected. Currently, no standard procedures with quantitative methods to objectively select regions of interest were reported. Therefore, users usually select analysis regions arbitrarily. For cells in culture, no fluorescent background artifacts are present in the FLIM image. Thus everything clustered into 1 group on the phasor plot. Randomly selecting a region (blue circle) within the lifetime distribution to pseudocolor the spatial image shows that the cells crowded to the right in the image field of view (**Fig. 5.1a**).

For engineered tissues, more than one species such as extracellular keratin and collagen are present. Thus, randomly selecting regions of interest to pseudocolor the intensity map results in a color map without any distinct features (**Fig. 5.1b**).

Alternatively, error analysis assists in quantitatively selecting the regions of interest on the phasor plots (**Fig. 5.1c**). The selected region (green circle) corresponds to certain tissue constituents, which we attributed to keratin, enabling visualization of tissue constituents in the pseudocolored map. As a result, the pseudocolored map demonstrates the keratin component on the left side in the image field of view, which cannot be achieved without error analysis for the phasor plot.

5.2.1. Algorithms

Phasor coordinates, g and s, for time-domain FLIM are defined in eqs. (3) and (4). Error propagation analysis was employed to derive Δg nd Δs on a phasor plot. Since g is a fractional number, error propagation was calculated as

$$\left(\frac{\Delta\frac{A}{B}}{\frac{A}{B}}\right)^2 = \left(\frac{\Delta A}{A}\right)^2 + \left(\frac{\Delta B}{B}\right)^2 - 2\left(\frac{\mathrm{Cov}(A,B)}{A\,B}\right) \quad (7)$$

Thus,

$$A = \text{numerator of } g = \int_0^\infty I(t)\cos(\omega t)dt$$

$$B = \text{denominator of } g = \int_0^\infty I(t)dt$$

In the case in which we have the contribution of multi exponential components,

$$A = \sum_i \int_0^\infty I(t)\cos(\omega t)dt$$

$$B = \sum_i \int_0^\infty I(t)dt$$

Assuming all the components are independent, and only Poisson noise is present in the TCSPC-FLIM data,

$$\Delta A^2 = \sum_i \int_0^\infty \Delta {I_i}^2(t)\cos^2(\omega t)\,dt = \sum_i \int_0^\infty I_i(t)\cos^2(\omega t)\,dt$$

$$\Delta B^2 = \sum_i \int_0^\infty \Delta {I_i}^2(t)dt = \sum_i \int_0^\infty I_i(t)dt$$

$$\mathrm{Cov}(A,B) = \sum_i \int_0^\infty \cos(\omega t)\,\mathrm{var}(I_i(t))\,dt = \sum_i \int_0^\infty I_i(t)\cos(\omega t)\,dt = A$$

Therefore,

$$\Delta g = \sqrt{\left(\frac{\sum_i \int_0^\infty I_i(t)\cos(\omega t)dt}{\sum_i \int_0^\infty I_i(t)dt}\right)^2 \times \left[\left(\frac{\sqrt{\sum_i \int_0^\infty I_i(t)\cos^2(\omega t)dt}}{\sum_i \int_0^\infty I_i(t)\cos(\omega t)dt}\right)^2 + \left(\frac{\sqrt{\sum_i \int_0^\infty I_i(t)dt}}{\sum_i \int_0^\infty I_i(t)dt}\right)^2 - 2\frac{1}{\int_0^\infty I(t)dt}\right]} \quad (8)$$

Δs can be derived with the same procedure,

$$\Delta s = \sqrt{\left(\frac{\sum_i \int_0^\infty I_i(t)\sin(\omega t)dt}{\sum_i \int_0^\infty I_i(t)dt}\right)^2 \times \left[\left(\frac{\sqrt{\sum_i \int_0^\infty I_i(t)\sin^2(\omega t)dt}}{\sum_i \int_0^\infty I_i(t)\sin(\omega t)dt}\right)^2 + \left(\frac{\sqrt{\sum_i \int_0^\infty I_i(t)dt}}{\sum_i \int_0^\infty I_i(t)dt}\right)^2 - 2\frac{1}{\int_0^\infty I(t)dt}\right]} \quad (9)$$

In addition to Δg and Δs, the covariance of g and s was derived. A parameter P is defined as $\frac{g}{s}$,

$$P = \frac{g}{s} = \frac{\sum_i \int_0^\infty I_i(t)\cos(\omega t)dt}{\sum_i \int_0^\infty I_i(t)\sin(\omega t)dt}$$

Therefore, by following eq. (7),

$$\left(\frac{\Delta P}{P}\right)^2 = \frac{\sum_i \int_0^\infty I_i(t)\cos^2(\omega t)dt}{\left(\sum_i \int_0^\infty I_i(t)\cos(\omega t)dt\right)^2} + \frac{\sum_i \int_0^\infty I_i(t)\sin^2(\omega t)dt}{\left(\sum_i \int_0^\infty I_i(t)\sin(\omega t)dt\right)^2} - 2\left(\frac{\cos(\omega t)\sin(\omega t)\sum_i I_i(t)}{\left(\sum_i \int_0^\infty I_i(t)\cos(\omega t)dt\right)\left(\sum_i \int_0^\infty I_i(t)\sin(\omega t)dt\right)}\right) \quad (10)$$

ΔP can also be written as $\Delta\frac{g}{s}$, which can be rewritten in another format,

$$\left(\frac{\Delta P}{P}\right)^2 = \left(\frac{\Delta \frac{g}{s}}{\frac{g}{s}}\right)^2 = \left(\frac{\Delta \mathrm{g}}{\mathrm{g}}\right)^2 + \left(\frac{\Delta \mathrm{s}}{\mathrm{s}}\right)^2 - 2\left(\frac{\mathrm{Cov(g,s)}}{\mathrm{g\,s}}\right)$$

Therefore,

$$\mathrm{Cov(g,s)} = \frac{g\ s}{2}\left[\left(\frac{\Delta \mathrm{g}}{\mathrm{g}}\right)^2 + \left(\frac{\Delta \mathrm{s}}{\mathrm{s}}\right)^2 - \left(\frac{\Delta P}{P}\right)^2\right] \quad (11)$$

Substituting eqs (8), (9), and (10) into eq (11), the covariance of g and s can be derived. Δg, Δs, and Cov(g,s) (tilt) compose a covariance matrix,

$$\begin{bmatrix} \Delta g^2 & Cov(g,s) \\ -Cov(g,s) & \Delta s^2 \end{bmatrix}$$

The matrix was used to transform a circle to a σ ellipse by Cholesky decomposition under the assumption that Δg and Δs approximate to the normal distribution (due to the large number of collected photons).

5.2.2. Phasor error analysis procedures

For a FLIM image with only one species, one cluster of phasor points was generated with points indicating a distribution of lifetimes. A simple linear fitting for those points on the phasor plot extracted two lifetimes. The two lifetimes were extracted by finding the intercepts of the fitted line and the single-exponential semicircle on the phasor plot. With the two lifetimes, error analysis then calculatesΔg,Δs, and Cov(g,s), thus determining an uncertainty area.

For a FLIM image with multiple species, the species of interest were first manually identified in the spatial image. The identification procedure only needs to be performed once for the same sample. The image area with the identified species was transformed to a phasor plot. Then, by following the same procedure of simple fitting and error analysis calculation, an uncertainty area was determined. It is noted that one species of interest was processed at a time. Therefore with N species, N uncertainty areas will be defined. The above procedures were coded and performed with Matlab.

5.3. Phasor error analysis of single fluorophores

Before phasor error analysis, FLIM images were binned to obtain the average peak intensity of 150-200 photons for an image for sufficient signals to analyze. Phasor error analysis was applied to FLIM images acquired from free nicotinamide adenine dinucleotide (NADH) and free flavin adenine dinucleotide (FAD) solutions (**Fig. 5.2**). The points or the lifetime distributions on the phasor plots were quantitatively analyzed with error analysis. Free NADH has a smaller lifetime distribution, tilt to the right (**Fig. 5.2a**). Free FAD has a larger lifetime distribution, tilt to the left (**Fig. 5.2b**). The red circles, indicating the 1-σ uncertainty areas, successfully characterized the size and the shape of the lifetime distributions.

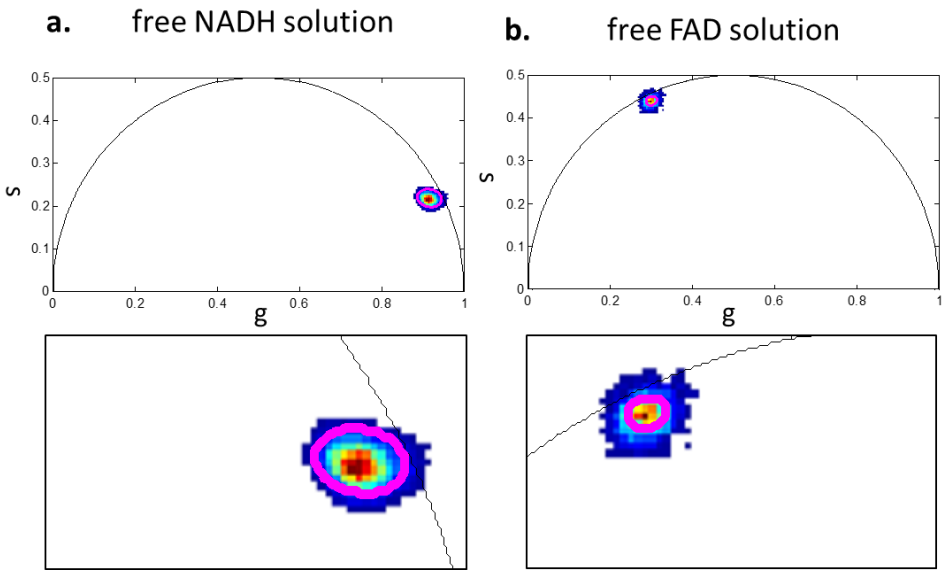

Figure 5.2 Phasor error analysis of FLIM images acquired from (a) free NADH and (b) free FAD solutions. The bottom two panels are magnified from the top two panels.

5.4. Phasor error analysis to distinguish tissue constituents in FLIM images

Figure 5.3 shows 3 channels of optical intensity images and 1 FLIM image acquired from a tissue-engineered construct. The construct had tissue constituents including cells and extracellular matrix keratin and collagen. The channel 1 optical intensity image shows all three tissue constituents. The channel 2 image shows mainly keratin (bottom left) and collagen (top). The second harmonic generation (SHG) channel shows only collagen. Single channel NAD(P)H FLIM image was acquired from the engineered tissues. Also shown in **Figure 5.3a** (right) is a fast FLIM map, post processed with the Markov Random field technique to clump related areas. The fast FLIM map shows some features of collagen in dark blue. However, keratin is indistinguishable. None of these images alone can distinguish multiple species in an image.

Figure 5.3b shows phasor plots of the NAD(P)H FLIM image in color and with black dots (magnified). The color phasor plot shows a distribution of phasor points with their weights. The magnified phasor plot shows the individual phasor points. Phasor error analysis was applied to the FLIM image. Binning was performed to obtain the average peak intensity of 150-200 photons for an image. The magnified phasor plot shows the resulting 1-σ uncertainty areas of keratin (green), collagen (blue), and cells (cyan).

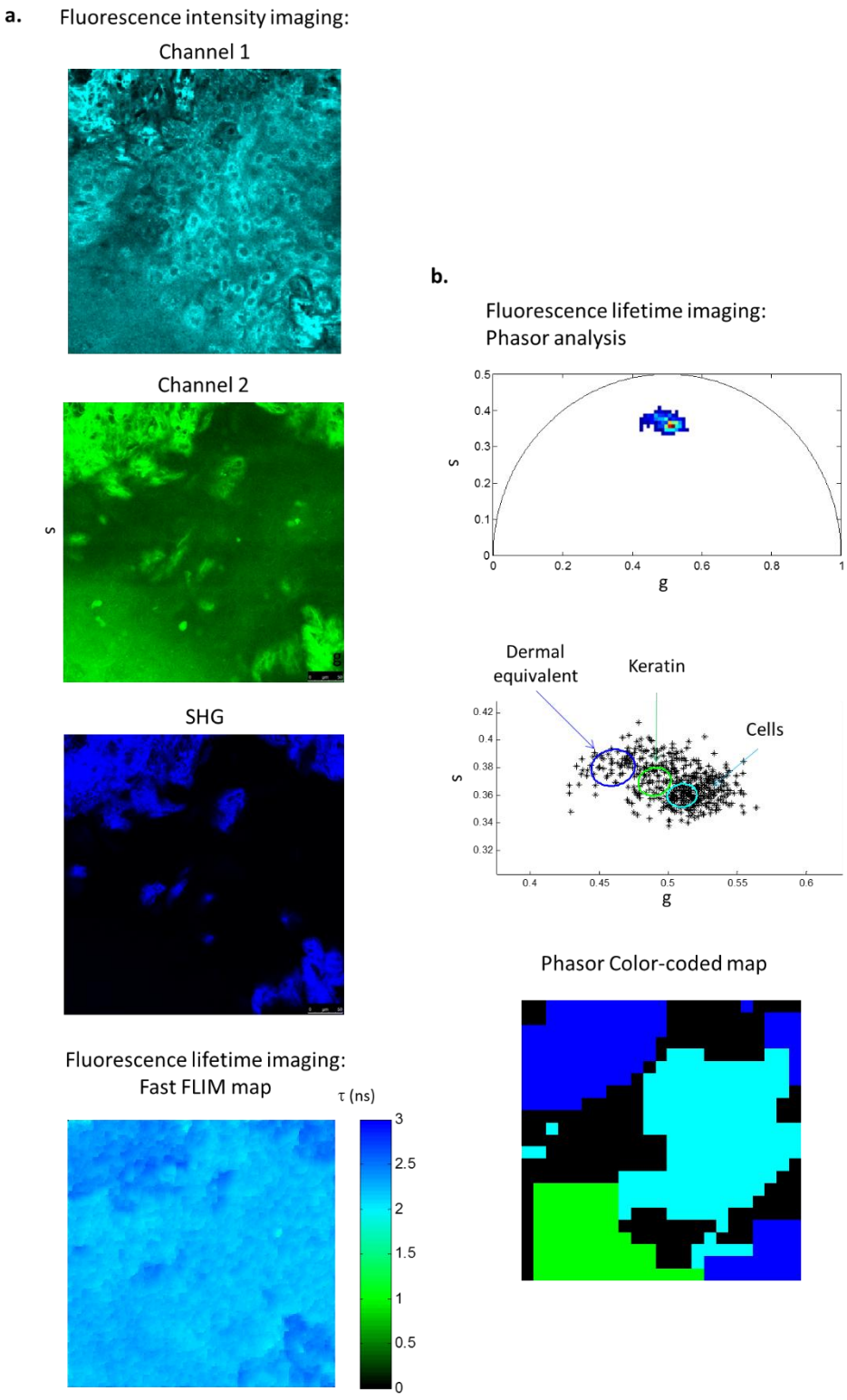

Figure 5.3 (a) Single optical intensity images and the fast FLIM map cannot distinguish different tissue constituents. (b) Phasor error analysis distinguished tissue constituents in the engineered tissues with single-channel NAD(P)H FLIM image.

Figure 5.3c shows the pseudocolored map, generated based on the uncertainty areas and post processed with the same technique applied for the fast FLIM map. The blue color for collagen consistently corresponds to the SHG image in **Figure 5.3a**. The light green color for keratin corresponds to the channels 1&2 images with keratin content in the bottom left corner. The cyan color for cells corresponds to the channel 1 image. Phasor error analysis successfully distinguished the three tissue constituents.

5.5. Phasor error analysis distinguished thermally-stressed from control engineered tissues

NAD(P)H FLIM images acquired from engineered tissues had signals from cells and extracellular matrix, collagen and keratin. When assessing cellular viability, the extracellular matrix usually interfered with the assessments. Thus, phasor error analysis was applied to exclude those unwanted signals.

Phasor error analysis defined the uncertainty areas of collagen and keratin as shown in **Figure 5.4**. Points lying within the purple region were defined as signals from the extracellular matrix. Points lying within the cyan region (outside the purple region) were defined as cellular signals.

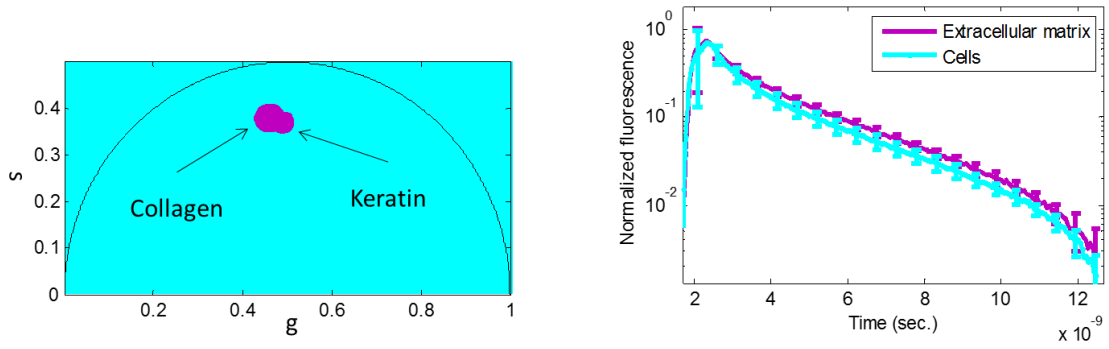

Figure 5.4 Phasor error analysis improved the FLIM assessments of cellular viability. (left) The analysis isolated collagen and keratin signals in the purple region. Signals lying outside the purple region (cyan region) are from cells. (right) 24 phasor points lying inside the purple region were averaged and plotted as extracellular matrix and 31 phasor points lying in the cyan region were averaged and plotted as cells. Error bars represent standard deviations.

Five control tissue-engineered constructs manufactured with primary human cells from 5 batches (30 control FLIM images) were analyzed. One average fluorescence decay of the extracellular matrix, collagen and keratin, and one average fluorescence decay of the cells were plotted (**Fig. 5.4,** right). The plot shows that cells have shorter lifetimes than the extracellular matrix. Phasor error analysis enables automatic separation of extracellular signals from cellular signals without manually selecting regions of interest for each image before cellular viability assessments.

FLIM was employed to characterize the cellular viability of five batches (5 batches) of tissue-engineered constructs. For each batch, one control construct and one thermally-stressed construct were manufactured. FLIM images acquired from the 5 control and the 5 thermally-stressed constructs were processed with phasor error analysis. Extracellular matrix signals were excluded from the cellular viability assessment. Since one FLIM image provides numerous points on the phasor plot, the transformed phasor points were

averaged to one for each FLIM image. The resulting phasor plot shows 30 averaged control (blue) and 18 averaged thermally-stressed (red) points (**Fig. 5.5**). The phasor plot separated the control and the thermally-stressed FLIM images. The bar plots show that the phasor coordinates, g and s, and the parameter g/s significantly distinguished between the control and the thermally-stressed engineered tissues (**P-value < 0.001 for 5 batches with 30 controls and 18 thermally-stressed constructs for all parameters). Statistical analysis was performed on the patient level, detailed in Sec. 3.2.4.

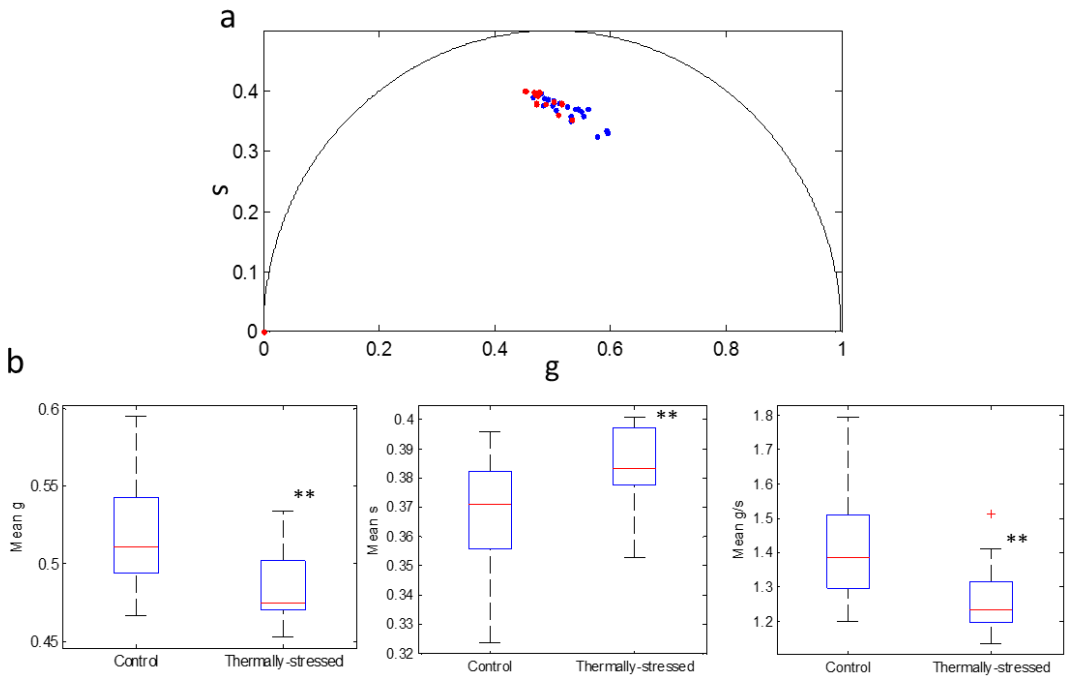

Figure 5.5 Phasor error analysis distinguished between the control and the thermally-stressed constructs shown by (a) the phasor plot and the (b) box plots (**P-value < 0.001 for 5 batches with 30 control (blue) and 18 thermally-stressed for all the three parameters).

5.6. Conclusions

Phasor error analysis was developed to visualize tissue constituents in one-channel FLIM images. Quantitative derivation of the algorithm was detailed in this chapter and verified with biologically relevant fluorophores. Free NADH and FAD solutions were chosen because they are biologically relevant and have a reported lifetime of 0.5 and 3ns [38], which respectively lies on the right and the left side in the phasor plot.

In addition, the method assessed single channel FLIM images acquired from tissue-engineered constructs. Compared to the work in Chapter 3 (Sec. 3.3.6., **Fig. 3.9**), in which extracellular signals were included in the cellular viability assessment, the study shown here provides a more accurate assessment of the cellular viability.

Since the engineered tissues were manufactured with human primary cells, individual tissue growth has high variability, depending on the patient's cell viability. Therefore, images of one group of thermally-stressed constructs have mostly extracellular matrix in an image because cells did not grow. Alternatively, images of another group of thermally-stressed constructs still have cells although with low viability. Interestingly, the first group of tissues assists in the viability assessment because they have high average fluorescence lifetimes due to the extracellular matrix. The extracellular matrix has a fluorescence lifetime longer than cells. Thus, images with more keratin or collagen have longer average fluorescence lifetime. This matches the expectation that thermally-stressed constructs have an average lifetime longer than the control constructs. However, the assessment is not for cells and thus not appropriate for the cellular viability assessment. The resulting phasor plot can only distinguish between the control and the stressed with one parameter (the s coordinate).

The second group of tissues has cells present. Phasor error analysis excluded unwanted extracellular signals and directly assessed cellular viability. The result successfully assessed the cellular viability with all the three parameters (g and s coordinates, and g/s). In conclusion, phasor error analysis provides a useful tool to quantitatively evaluate the points (lifetime distribution) on the phasor plots and to distinguish different species. Thus, in addition to the phasor plot's advantages of direct, rapid interpretation and visualization of the FLIM images, phasor error analysis can quantitatively determine the pseudocolored map and assess species of interest to provide users a useful tool in objectively assessing the acquired FLIM images.

Chapter 6 Phasor Analysis of Time-gated Fluorescence Lifetime Imaging Microscopy

Phasor analysis has the advantage of direct, rapid interpretation of fluorescence lifetime imaging microscopy (FLIM) images without prior knowledge of samples. In this chapter, a phasor analysis algorithm for time-gated FLIM was developed, accounting for various gating schemes (separate, continuous, and overlapping gates). However, the time-gated image acquisition method from living cells results in low fluorescence signals. Therefore, the phasor plot shows big spreads of points, big lifetime distributions. Novel total variation (TV) models were developed to improve the phasor plot analysis of time-gated FLIM images. Artificial and real living-cell time-gated images were analyzed. TV denoising increased precision of fluorescence lifetime determination and globally preserved the magnitude of the lifetimes and amplitudes of the lifetime maps. The denoised time-gated images were analyzed with the phasor plots. The resulting phasor plots exhibit tighter spreads of points, thus tighter lifetime distributions. The improved phasor plots enabled users to pseudocolor the pixels in the intensity images to create color maps, showing intracellular variation with different lifetimes. The analyses provided here can enhance the precision and visualization of low-light and fast video-rate imaging in rapidly emerging new applications of FLIM.

6.1. Time-Gated Fluorescence lifetime imaging microscopy (FLIM)

Time-gated wide-field FLIM, commonly used in high-speed imaging, can be implemented with a gating device, such as an intensified charge-coupled device camera, to record integrated fluorescence signals [97, 98]. The gating parameters include the gate width, g, and the time interval between the starting points of two consecutive gates, Δt. Gating can be performed continuously or separately with the designed instrumentation setup. **Figure 6.1 (**left and center) shows examples of separate gates and continuous gates with the 4-gate setting. Lifetime can be retrieved using intensity images captured over the gate width at several different delays after the excitation pulse [98].

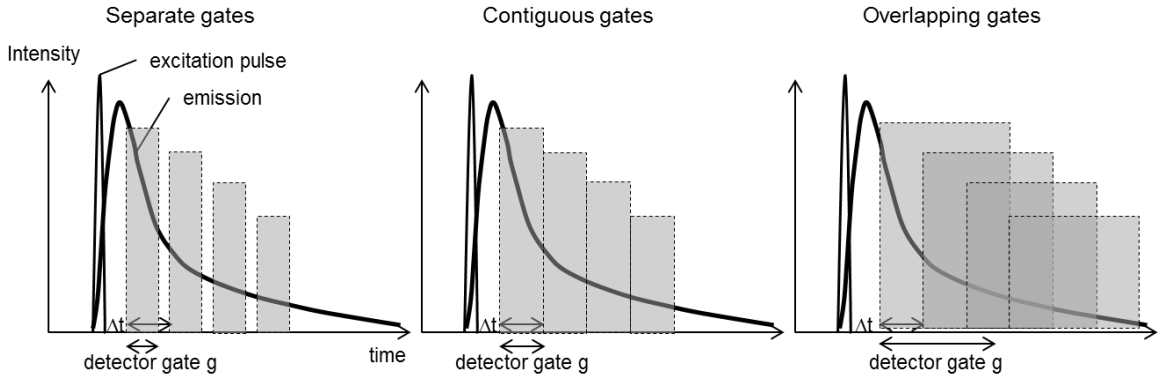

Figure 6.1 Time-gated FLIM concept of (left) separate gating ($g < \Delta t$), (center) continuous gating ($g = \Delta t$), and (right) overlapped gating ($g > \Delta t$).

Alternatively, time-gated FLIM can be performed by virtually gating the time correlated single photon counting (TCSPC)-FLIM images. TCSPC-FLIM is a more common FLIM setup. The technique collects the whole fluorescence decays with high accuracy. However, it requires a long image acquisition time depending on the samples. It was

reported that with the optimal virtual gating, lifetime maps of TCSPC-FLIM has improved precision [99-102]. The optimal virtual gating algorithm can result in the overlapped gating scheme in some cases. The overlapping gates with the 4-gate setting are shown in **Figure 6.1** (right).

6.2. Algorithm for phasor analysis of time-gated FLIM with various gating schemes

Phasor analysis of time-gated FLIM was previously developed for the continuously gating scheme [103]. A phasor is a point resulting from the phasor analysis, transforming 3-dimensitonal FLIM images to the 2-dimensional phasor plots. The modified phasor (R') is reported

$$R'(\tau,\omega)=\frac{\int_0^T[\int_{t-\frac{T}{2K}}^{t+\frac{T}{2K}} e^{-t'/\tau}\,dt']\; e^{j\omega t}\;\sum_{m=-\infty}^{\infty}\delta\left[t-\left(m+\frac{1}{2}\right)\frac{T}{K}\right]dt}{\int_0^T[\int_{t-\frac{T}{2K}}^{t+\frac{T}{2K}} e^{-t'/\tau}\,dt']\;\sum_{m=-\infty}^{\infty}\delta\left[t-\left(m+\frac{1}{2}\right)\frac{T}{K}\right]dt} \qquad (12)$$

where T is the acquisition time frame, K is the number of time bins, i.e. the number of gates, τ is the fluorescence lifetime, $\omega=\frac{2\pi}{T}$ is the angular pulse frequency, and m is the binned index.

To account for the separately gating and the overlapped gating schemes, another modified phasor (P') incorporating g and Δt was developed based on eq. (12),

$$P'(\tau,\omega)=\frac{\int_0^T[\int_{t-\frac{g}{2}}^{t+\frac{g}{2}} e^{-t'/\tau}\,dt']\; e^{j\omega t}\;\sum_{m=-\infty}^{\infty}\delta(t-m\Delta t-{}^{g}/_{2})dt}{\int_0^T[\int_{t-\frac{g}{2}}^{t+\frac{g}{2}} e^{-t'/\tau}\,dt']\;\sum_{m=-\infty}^{\infty}\delta(t-m\Delta t-{}^{g}/_{2})dt} \qquad (13)$$

Substituting $t = m\Delta t + g/2$ into eq. (13), the P' becomes

$$P'(\tau,\omega) = \frac{\sum_{m=0}^{K-1}\left[e^{\frac{-m\Delta t}{\tau}}\left(1-e^{-g/\tau}\right)\right] e^{j\omega(m\Delta t+\frac{g}{2})}\left(1-e^{-\Delta t/\tau}\right)}{\tau(1-e^{-g/\tau})(1-e^{\frac{-\Delta t}{\tau}K})} \tag{14}$$

In a standard phasor plot analyzing the whole fluorescence decays, a semicircle characterized the single-exponential decay phasors as shown by the black semicircle in **Figure 6.2**. Multiexponential fluorescence decay phasors lie inside the semicircle. For the time-gated phasor plot, the semicircle distorted. Single-exponential decays are characterized by $P_{1-exp}{}'$, which was simplified from eq. 14.

$$P_{1-exp}{}'(\tau,\omega) = \frac{\sum_{m=0}^{K-1} e^{\frac{-m\Delta t}{\tau}} e^{j\omega(m\Delta t+\frac{g}{2})}\left(1-e^{-\Delta t/\tau}\right)}{\tau(1-e^{\frac{-\Delta t}{\tau}K})} \tag{15}$$

6.2.1. Time-gated phasor plot

Figure 6.2 shows the phasor plot developed for a four-gate time-gated FLIM setting. The two parameters, $g/\Delta t$ and g/τ, are independent of the gating schemes on the phasor plot. That is, regardless of the gating schemes, experiments with the same $g/\Delta t$ parameter have the same single-exponential phasor curves (the reddish curves). Therefore, the phasor plot can be employed for all the three gating schemes. We plotted only 11 curves due to the limited space. With eq. (15), a whole range of single-exponential phasor curves can be plotted. In addition, eq. (15) can also account for different gating numbers.

The $g/\Delta t$ parameter first assists users in locating the single exponential phasor curves, the g/τ color map on the background assists in determining the lifetime. The g/τ color map was constructed based on the simulation results for eq. (15) with the setting of

- g ranging from 0.1 to 10ns with a step size of 0.5ns,
- $g/\Delta t$ ranging from 10^{-1} to 10 with a step size of $10^{0.01}$, and
- τ ranging from 0.1 to 10ns with a step size of 0.05ns.

It was found the same as $g/\Delta t$, the g/τ parameter is also independent of other parameters.

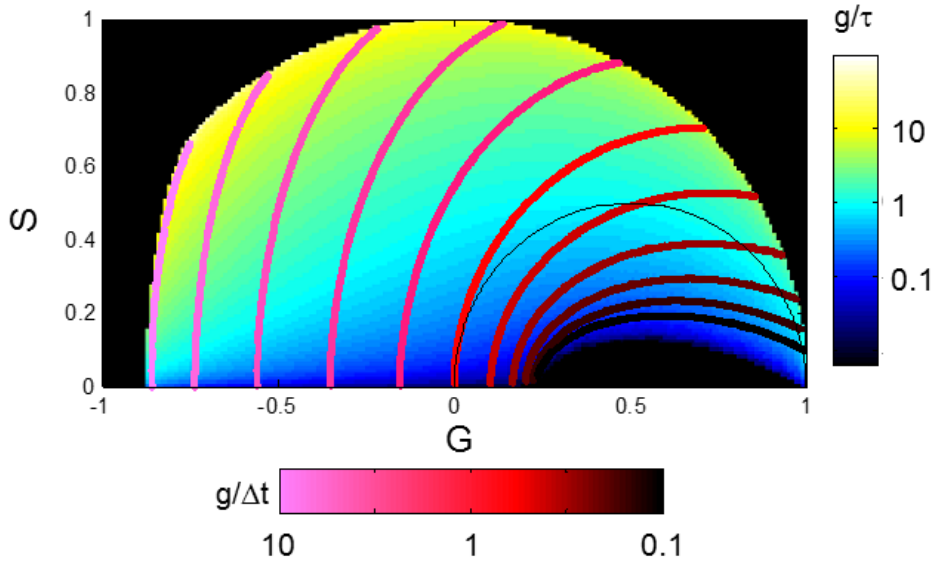

Figure 6.2 Four-gate time-gated phasor plot map. The map demonstrates $g/\Delta t$ (reddish curves) & g/τ (underlying color map) of the single-exponential fluorescence decay model. The black semicircle indicates the phasor plot of the whole single-exponential fluorescence decays with no gating. Color bars are in the logarithm scale.

Therefore, four-gate time-gated FLIM users can directly employ **Figure 6.2** to interpret acquired time-gated FLIM images on the phasor plot. Two procedures are needed: first is to locate the single exponential phasor curve based on the experimental setting *g/dt* on the phasor plot; second is to determine the single exponential lifetimes on the curve according to the color background. For users with gate number different from four, a time-gated phasor plot can be constructed by following eq. (15) and the simulation described above.

6.3. Precise fluorophore lifetime mapping

Precise fluorophore lifetime mapping is vitally important to quantifying the biological microenvironment. One challenge to precise lifetime mapping is that all measurements must be obtained without perturbing living cells – a difficult task. The experimenter may be tempted to use high power and long measurement times to acquire high quality images, but such conditions could damage the cells and fluorophores. The opposite can also be true. Low-light and fast measurements will maintain cell viability, but may not produce images with high signal-to-noise ratio. Temporal optimization and spatial denoising methods were developed to address this problem and enhance the precision of acquired FLIM data.

For time-gated FLIM, optimal temporal gating techniques using either Monte Carlo simulations or analytical error propagation analysis were developed to reduce the illumination light dose, while additionally improving the precision of lifetime analysis [48, 101]. Relative standard deviation (RSD), defined as the standard deviation divided by the mean value, was calculated over a determined FLIM image assuming only Poisson

noise. The optimal gating parameters, the gate width and the time interval between the starting points of two consecutive gates, were determined by minimizing the RSD. In addition to optimal temporal gating, image denoising methods were employed to enhance time-gated and TCSPC-FLIM data for precise lifetime mapping.

Both optimal virtual gating and the total variation (TV) denoising method, commonly used in medical imaging systems for selective smoothing and hence edge preserving, reduced RSD of TCSPC-FLIM data in living cells [100]. In particular, when combining the two methods sequentially, the resulting RSD was lower than when either method was employed alone. One advantage of this newly developed, TV-based spatial denoising method is its versatility: the technique can be employed to denoise intensity images at each gate or it can directly denoise a lifetime map with either Poisson or non-Poisson distributed noise [99-101].

In this study, previously developed unmodified f-weighted total variation (FWTV) and modified FTWV, unmodified u-weighted total variation (UWTV) and modified UWTV, PoissTV, and a constrained Rudin-Osher-Fatemi (conROF) model were employed to improve the precision of FLIM maps.

6.4. Verification: Artificial image

An artificial FLIM image with known parameters (**Fig. 6.3**) was generated to evaluate the combined analysis of the TV denoising and the time-gated phasor plots. For simplicity, single-exponential decay was used: $I(t) = \alpha_1 \exp(-t/\tau_1)$, where $I(t)$ is fluorescence intensity as a function of time, τ_1 is fluorescence lifetime, and α_1 is a pre-exponential term

representing intensity at time zero. Subscription "1" (the first component) was used just to be general for potential multi-exponential decay. The geometry in **Figure 6.3** was used to mimic the geometry we may encounter in living-cell FLIM, with "the inner circle" (the centered solid circle in the left panel), "the ring" (the open circle outside the inner circle in the left panel), and "the satellite" (the small dot to the bottom right of the inner circle). As an example of this geometry, a cell may have fluorophores, or fluorescent molecules, inside it with some interactions taking place in its membrane, while in another smaller cell or organism the same fluorophores at lower concentration are present.

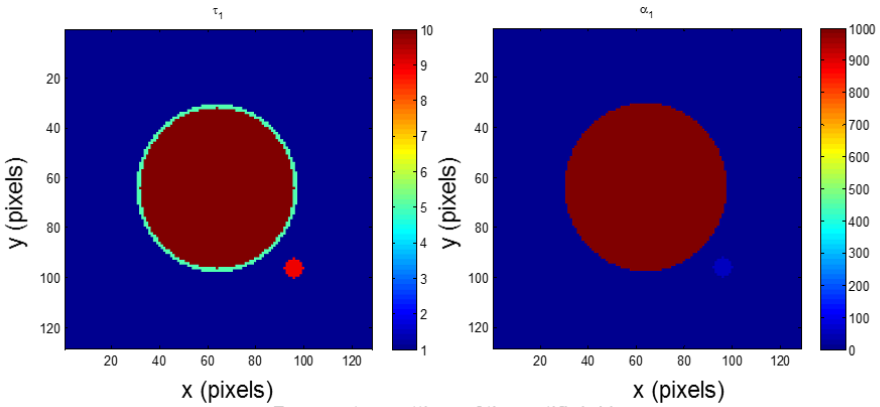

Parameter setting of the artificial images

	Inner circle	Ring	Satellite
center	(m'/2, n'/2)	(m'/2, n'/2)	(3m'/4, 3n'/4)
radius	n'/4	2.1n'/8	n'/32
τ_1	10	5	9
α_1	1000	1000	50

Figure 6.3 Artificial images mimicking the geometry that may be encountered in living-cell FLIM experiments. τ_1 values are in ns; α_1 values are in arbitrary unit. The table shows the parameter setting in the artificial image.

Unmodified FWTV and UWTV along with PoissTV and a constrained ROF model were applied to noise versions of the artificial images. The result shows that all models could improve the lifetime precision for all three objects with decreased RSD. The improvements were greater for the inner circle than the satellite, while the ring had the smallest improvements. The ROF model produced lower RSD in the ring and the satellite. However, it made the RME of the satellite extremely negative and the corresponding lifetime highly inaccurate. PoissTV, FWTV, and UWTV gave similar results and they provided much better lifetime accuracy of the satellite than the ROF model. They also produced lower RSD values of the inner circle due to their better noise magnitude estimation. FWTV produced slightly better results than the other two in terms of the satellite RME.

6.4.1. Time-gated phasor analysis of the artificial images

Figure 6.4 shows the time-gated phasor plots with the g/τ background and the single-exponential fluorescence phasor curve of $g/\Delta t$ = 0.2. In the first phasor plot (shaded in gray), the ten black dots on the curve indicate the single exponential decay lifetimes, ranging from 1 to 10ns. Its magnified phasor plot on the right provides a map to locate the 8, 9, and 10ns single fluorescence decays. Undenoised and denoised artificial FLIM images were transformed to the time-gated phasor plots. Each dot on the phasor plot is a resulting phasor from the transformation. The regions with the black dash boxes (all to the same scale) were magnified and shown on the right. The magnified images are all to the same scale as the first magnified map shaded in gray.

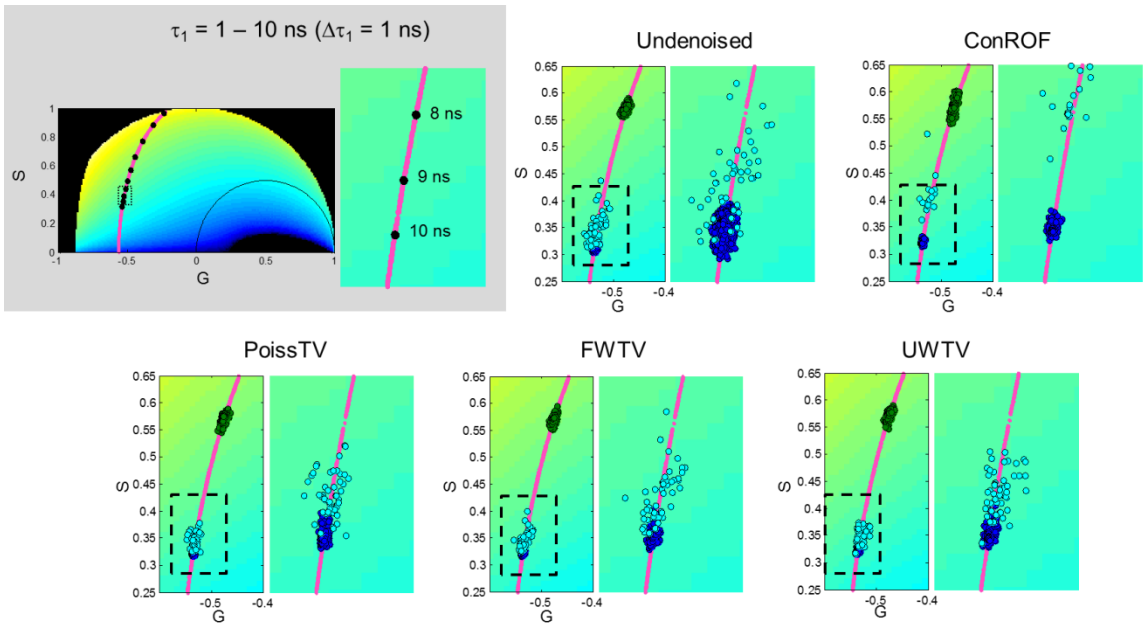

Figure 6.4 Time-gated phasor plots for the undenoised and the denoised FLIM images. The denoised phasor plots show decreased lifetime distributions.

On the time-gated phasor plots, the green dots are from the ring, the light blue dots are from the satellite, and the dark blue dots are from the inner circle of the artificial image. The undenoised phasor plot (**Fig. 6.4**, upper middle) shows the overlap of the blue and the light blue dots. In contrast, the denoised phasor plots show separation between the blue and the light blue dots, lying near the 10ns and 9ns respectively as compared to the gray shaded map. The result matched our experimental setting (**Fig.6.3**, table) of 10ns for the inner circle and 9ns for the satellite. The ConROF model reduced the phasor distribution the most. However, it distorted the result as the light blue dots moved away from the 9ns point.

6.5. Combined time-gated phasor analysis and TV denoising method to provide pseudocolored maps of intracellular lifetime variation

Human colon carcinoma cells (HCT-116 cells, American Type Culture Collection, CCL-247™) were cultured with modified McCoy's 5a medium and incubated under 5% CO_2. When cell confluence reached ~80% in culture dishes, the culture medium was removed and dishes were washed three times with phosphate buffered saline (PBS). The living cells were then incubated with 1μM BCECF [2',7'-bis-(2-carboxyethyl)-5-(and-6)-carboxyfluorescein, acetoxymethyl ester, Invitrogen, CA] in PBS at 37^{o}C for 60 minutes before FLIM imaging [104]. The settings for imaging were as described in section **Error! eference source not found.**, except that four gates were employed with gating parameters Δt = 1ns and g = 0.2ns. For each gate, five images were averaged. Unreasonably high lifetime values (> 5ns) were set to zero. BCECF excited state lifetime is a sensitive indicator of intracellular pH [105, 106], therefore precise fluorescence lifetime determination of BCECF in living cells is of interest to researchers.

To create fluorescence lifetime maps rapidly, a four-gate protocol with an analytical least squares lifetime determination algorithm was used on a pixel-by-pixel basis. It is more precise than the two-gate protocol while still easy to implement [47-49]:

$$\tau_p = -\frac{N(\sum t_i^2) - (\sum t_i)^2}{N\sum t_i \ln I_{i,p} - (\sum t_i)(\sum \ln I_{i,p})}$$

where τ_p is the lifetime of pixel p, $I_{i,p}$ is the intensity of pixel p in image i, t_i is the gate delay of image i, and N is the number of images. All sums are over i.

6.5.1. TV denoising of time-gated living cell images

Time-gated FLIM images were acquire from the living cells. The acquired intensity images from the four gates were processed with TV denoising. The denoised images were employed to calculate lifetime maps according to the lifetime determination algorithm. **Figure 6.5** demonstrates that in the undenoised lifetime map (upper left), lifetime random fluctuations can be observed, obscuring possible live-cell spatial patterns of special interest. After FWTV and UWTV denoising with *gain* (upper right and lower right) the lifetime maps appeared similar, with uncertainties removed but spatial patterns remained. The *gain* prevented over-smoothing vs. the undenoised image. The lifetime map after FWTV, PoissTV, and UWTV denoising was even smoother but the small region on the right disappeared due to improper variance estimation. In this case, conROF denoising did not appear suitable (it produced negative intensity values in some regions of the cells) and hence was excluded from analysis.

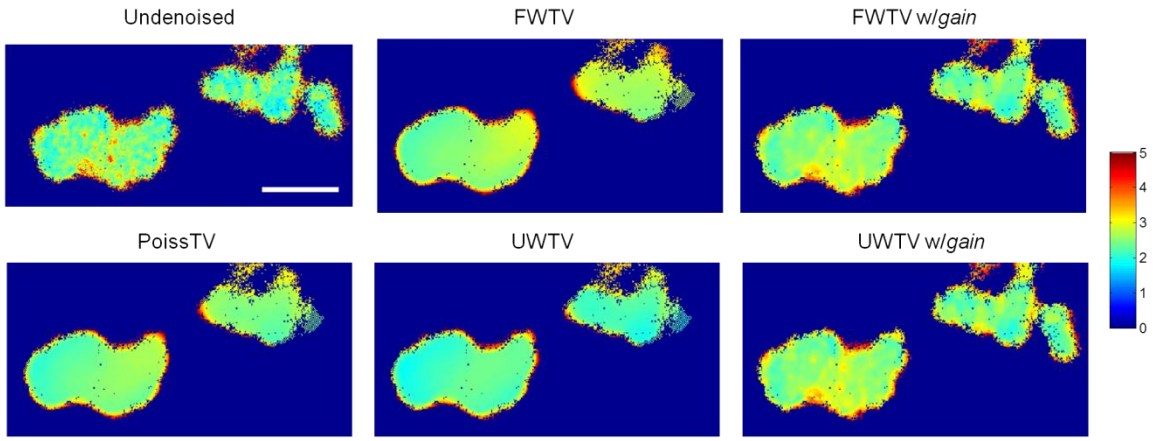

Figure 6.5 Lifetime maps of the undenoised and denoised living cell FLIM images (values in ns). TV denoising was applied to each of the four intensity images before lifetime reconstruction. The images were acquired with living HCT-116 cells stained with BCECF. Scale bar: 40 μm.

6.5.2. Time-gated phasor analysis of living cell images

The denoised FLIM images of living cells were analyzed with time-gated phasor plots (**Fig. 6.6**). The brown curves indicate the single exponential phasor curve of $g/\Delta t = 4$. The ten back points on the curve indicate the single exponential lifetimes, ranging from 1-10ns. The phasor points resulting from the cells lie inside the curves, indicating that cells have multiexponential fluorescence decays.

Figure 6.6 shows that the undenoised phasor plot (upper left) has a big spread of phasor points (lifetime distribution). The FWTV-, PoissTV-, and UWTV phasor plots demonstrate irregular spreads with sharp edges. In contrast, The FWTV w/*gain* and UWTV w/*gain* phasor plots have a spread that is more similar to the undenoised phasor plot. In addition, the phasor plots have one intensive center rather than a sparse spread of phasor points as that in the undenoised phasor plot.

Phasor plots can be employed to color the pixels in an image to create a map. Take the UWTV phasor plot for example (**Fig. 6.6**, bottom). Three regions were manually selected (blue lines). The phasor points lying inside the selected regions were tracked back to their locations in the image. The pixels were then colored in white as shown alongside. The UWTV pseudocolored maps don't show intracellular features. FWTV and PoissTV had similar results in their pseudocolored maps. This is attributed to the improper over-smoothing of the denoising methods.

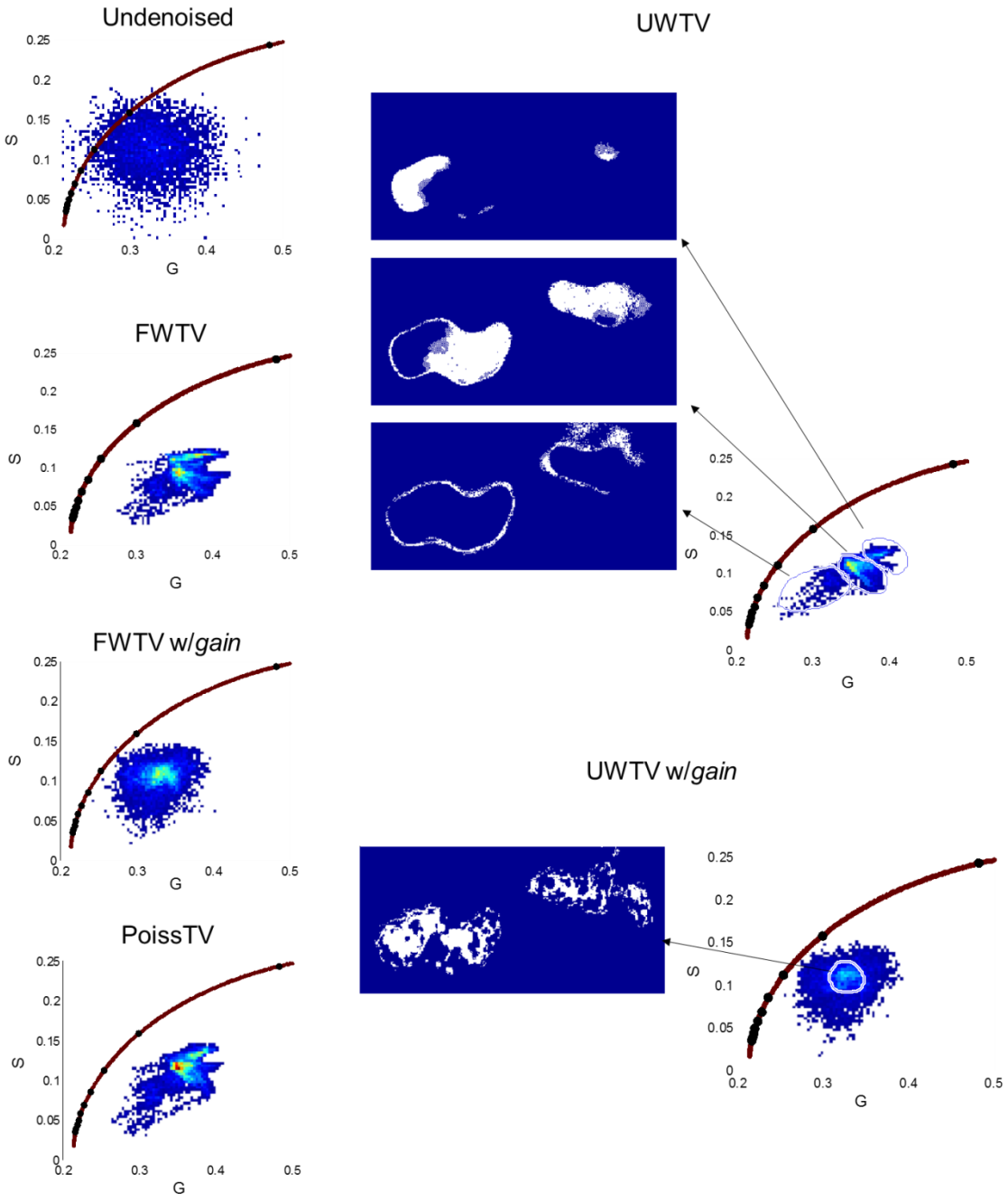

Figure 6.6 Phasor plots of the undenoised and the denoised time-gated FLIM images of living cells. The pseudocolored map of UWTV *w/gain* phasor plots shows intracellular lifetime variation.

The phasor plot of UWTV *w/gain* was employed to create the pseudocolored map (**Fig. 6.6**, bottom right). The intensive center region was manually selected to color the pixels in the image. The pseudocolored map demonstrates the intracellular lifetime variation that is similar to the pattern shown in the undenoised lifetime map (**Fig. 6.5**, upper left) without excess fluctuations. FWTV *w/gain* has a similar result (data not shown). These results suggest that FWTV *w/gain* and UWTV *w/gain* could enable pseudocolored maps of time-gated phasor plot analysis to demonstrate intracellular lifetime variation

6.6. Discussions and conclusions

In this report, we assumed the starting point of the first gate is the peak intensity without any delay from the peak. Therefore, the provided time-gated phasor analysis does not account for the time delay between the peak and the first gate. As we added the time delay variable, the time-gated phasor plots became more complex. Careful characterization will be performed to account for the time delay on the phasor plots in future studies.

The fluorescence lifetime maps shown here were calculated with the analytical least squares lifetime determination algorithm. The algorithm is for the single-exponential decay sample. We employed the algorithm for a simple derivation of the lifetime maps for the comparison of different denoised FLIM images. An algorithm for multi-exponential fluorescence decay can be employed. However, to use the algorithm requires a prior knowledge of how many components are present in the sample.

Phasor analysis does not require any prior knowledge of the sample. FLIM images were directly transformed by the analysis to a phasor plot. The method is direct, rapid, and

providing visualization for users of the lifetime distribution. Time-gated phasor analysis was further developed in this report to analyze time-gated FLIM images. We provided a method for users to construct a time-gated phasor map for various gating schemes. Combined with the TV denoising method, the reported technique demonstrates intracellular lifetime variation. In summary, the analyses provided here can enhance the visualization and precision of low-light and fast video-rate imaging in rapidly emerging new applications of FLIM.

Chapter 7 Conclusions and Future Directions

7.1. Major contributions of this dissertation

Label-free nonlinear optical molecular imaging and quantitative analytic methods were developed to non-invasively assess the viability of primary human cells in standard culture and it tissue-engineered constructs. To the best of our knowledge, this is the first report employing label-free nonlinear optical microscopy to characterize *in vitro* cell-based devices manufactured with primary human cells. The acquired optical signals enabled tissue viability assessment via developed spatial, optical redox ratio, and FLIM analysis. Label-free optical measures of local tissue structure and biochemistry characterized morphologic and functional differences between controls and stressed constructs. Rigorous statistical analysis accounted for variability between human patients. The technique reliably differentiated stressed from control constructs from 10 batches. The sensitivity of the technique was further supported by its significant correlation with the standard cell viability assays. Our results suggest that such optical measures could serve as reliable manufacturing release criteria for cell-based tissue-engineered constructs prior to human implantation, thereby addressing a critical regulatory need in regenerative medicine.

Further quantitative algorithms were developed to assist in direct and rapid interpretation and visualization of fluorescence lifetime imaging microscopy (FLIM) images. The developed phasor error analysis algorithm successfully distinguished tissue constituents with one-channel FLIM images of engineered tissues. It further improved the cellular viability assessments of FLIM in the engineered tissues. The developed time-gated phasor analysis algorithm provides the users a method to directly and rapidly interpret and visualize the time-gated FLIM images. The method was combined with a denoising technique to enable rapid monitoring of intracellular lifetime variations. The two algorithms could provide FLIM users a useful tool to avoid complicated fitting procedures, which require prior knowledge of the samples, and to easily interpret and visualize the FLIM images. In summary, label free nonlinear optical molecular imaging and quantitative algorithms were shown to successfully characterize living biological systems. Beyond characterizing cellular spatial organization and metabolism, in the future, it could be further used to characterize cancer, monitor vascular network, monitor extracellular matrix, localize cells, and so forth.

The major contributions can be summarized as follows:

Chapter 2

- We developed label-free nonlinear optical microscopic imaging including fluorescence intensity, second harmonic generation, and fluorescence lifetime imaging with controlled imaging environment for the cellular viability assessments.

- We developed quantitative algorithms to assess cellular viability, spatial organization, and intracellular microenvironment for the cellular viability assessments.
- We verified the developed techniques by staining intracellular mitochondria, alternating cellular metabolic pathways, analyzing optical spectra acquired from human primary cells in culture and in engineered tissues, and assessing cellular viability of primary human cells in standard culture.

Chapter 3

- We designed experiments, manufactured engineered tissues with primary human cells from multiple patients, and performed multiple stressing mechanisms to create a range of states of tissue viability in the tissues-engineered constructs.
- We non-invasively monitored engineered tissues with label-free nonlinear optical microscopy with multiple channels in real time and performed 3D imaging to visualize the engineered tissues.
- We assessed cellular viability, cellular organization, and intracellular microenvironment of the engineered tissues with the developed metrics to characterize the tissue viability.
- We compared optical measures with standard histology and glucose consumption readings with rigorous statistical testing to account for variability between patients.
- We performed the *in vivo* mouse study to characterize and correlate the pre-implantation tissue viability to post-implantation graft success.

Chapter 4

- We characterized rapamycin-treated engineered tissues with a range of states of tissue viability with optical measures, standard cellular viability assay (WST-1), histology, and immunofluorescence histology.
- We demonstrated the spatial selectivity of label-free nonlinear imaging microscopy that is useful for the monitoring of the large-scale engineered tissues manufacture.
- We quantitatively compared between optical measures, histology scores, and WST-1 measures and performed statistical analysis to correlate these metrics.
- We identified that rapamycin treatment during the cell culture stage could improve tissue growth in the poorly-growing batches.

Chapter 5

- We explored phasor analysis with the advantages of rapid and direct interpretation and visualization of FLIM images without prior knowledge of the samples, and extended the algorithm to develop the phasor error analysis,
- We developed phasor error analysis to quantitatively identify the size and the shape of the uncertainty areas of the fluorescence lifetimes of interest on a phasor plot.
- We verified the developed phasor error analysis algorithm with biological relevant fluorophores.

- We differentiated multiple tissue constituents by assessing one-channel NAD(P)H FLIM images acquired from tissue-engineered constructs with the developed phasor error analysis.
- We improved the viability assessment of FLIM images acquired from tissue-engineered constructs by performing phasor error analysis to exclude extracellular signals from the cellular viability assessments.

Chapter 6

- We developed time-gated phasor plots to analyze time-gated FLIM images acquired with various gating schemes including separate gating, continuous gating, and overlapped gating.
- We proposed algorithms to construct a time-gated phasor plot map to interpret time-gated FLIM images.
- We improved the lifetime determination by combining the developed time-gated phasor plot analysis and the total variation denoising technique, and verified the method with artificial images mimicking cells.
- We created pseudocolored maps, demonstrating intracellular lifetime variation, of living cells by performing the combined time-gated phasor analysis and denoising method.

The work in this dissertation has been presented and documented as cited below:

Chapter 1

Chen, L.-C., Lloyd, W.R., Chang, C.-W., Sud, D., and Mycek, M.-A. Fluorescence Lifetime Imaging Microscopy for Quantitative Biological Imaging. *Digital Microscopy, Edition 4*, (Sluder, G. and Wolf, D.E., Ed.) Elsevier, Ch.20, pp. 457-488 (2013).

Lloyd, W.R., **Chen, L.-C.**, and Mycek, M.-A. Fluorescence spectroscopy in regenerative medicine. *Optical Techniques in Regenerative Medicine*, (Morgan, S.P., Matcher, S.J., Rose, F., Ed.) CRC Press, Ch.7, pp. 171-204 (2013).

Lloyd, W.R., **Chen, L.-C.**, Wilson, R.H., and Mycek, M.-A. Clinical Fluorescence Spectroscopy and Imaging. *Biomedical Technology and Devices Handbook, Edition 2*, (Maitland, D. and Moore, J., Ed.) Taylor & Francis, Ch.11, pp. 267-292 (2013).

Chapters 2 & 3

Chen, L.-C., Lloyd, W.R., Kuo, S., Kim, H.M., Marcelo, C.L., Feinberg, S.E., and Mycek, M.-A. The potential of nonlinear optical molecular microscopy characterizes tissue-engineered constructs and assesses local viability. *Biomaterials* (2014).

Scanlon, C. S., Van Tubergen, E. A., **Chen, L.-C.**, Elahi, S. F., Kuo, S., Feinberg, S., Mycek, M.-A. and D'Silva, N. J. Characterization of squamous cell carcinoma in an organotypic culture via sub-surface nonlinear optical molecular imaging. *Experimental Biology and Medicine* (2013).

Chen, L.-C., Lloyd, W.R., Kuo, S., Kim, H.M., Marcelo, C.L., Feinberg, S.E., and Mycek, M.-A. Label-free optical molecular imaging to assess engineered tissues. *Optical Molecular Probes, Imaging, and Drug Delivery Topical Meeting* (2013).

Chen, L.-C., Lloyd, W.R., Kuo, S., Marcelo, C.L., Feinberg, S.E., and Mycek, M.-A. Label-free multiphoton fluorescence imaging monitors metabolism in living primary human cells used for tissue engineering. *Imaging, Manipulation, and Analysis of Biomolecules, Cells, and Tissues X, Proceedings of SPIE*, paper 8225-18 (2012).

Mycek, M.-A., **Chen, L.-C.**, Lloyd, W.R., Kuo, S., Marcelo, C.L., and Feinberg, S.E. Label-Free Nonlinear Optical Molecular Imaging in Live Cells and Tissues: Applications to Tissue Engineering. *Focus on Microscopy* (2012).

Lloyd, W.R., **Chen, L.-C.**, Kuo, S., Marcelo, C.L., Feinberg, S.E., and Mycek, M.-A. Fluorescence lifetime imaging microscopy (FLIM) studies of living primary human cells for applications in tissue regeneration. *Multiphoton Microscopy in the Biomedical Sciences XII, Proceedings of SPIE*, paper 8226-8 (2012).

Chen, L.-C., Lloyd, W.R., Wilson, R.H., Kuo, S., Marcelo, C.L., Feinberg, S.E., and Mycek, M.-A. Nonlinear Optical Molecular Imaging Enables Metabolic Redox Sensing in Tissue-engineered Constructs., paper 8089-18 (2011).

Chen, L.-C., Lloyd, W.R., Chandra, M., Izumi, K., Kuo, S., Marcelo, C.L., Feinberg, S.E., and Mycek, M.-A. Optical Redox Imaging of Endogenous Contrast for Tissue-engineered Construct Viability. *Optical Molecular Probes, Imaging, and Drug Delivery Topical Meeting* (2011).

Wilson, R.H., **Chen, L.-C.**, Lloyd, W.R., Kuo, S., Marcelo, C.L., Feinberg, S.E., and Mycek, M.-A. Mesh-based Monte Carlo Code for Fluorescence Modeling in Complex Tissues with Irregular Boundaries. Novel Biophotonic Techniques and Applications. *Proceedings of SPIE-OSA Biomedical Optics*, paper 8090-14 (2011).

Chen, **L.-C.,** Mycek, M.-A., Lloyd, W.R., Kuo, S., Feinberg, S.E., Marcelo, C.L., Kim, H.M. Nonlinear optical microscopy for viability assessment of tissue-engineered constructs. United States Patent and Trademark Office, Provisional Patent Application No. 61/585,827 (2012).

Chapter 4

Chen, L.-C., Kuo, S., Lloyd, W.R., Kim, H.M., Marcelo, C.L., Feinberg, S.E., and Mycek, M.-A. Label-Free Optical Metrics Assessed Rapamycin-Treated Tissue-Engineered Oral Mucosa. (In preparation).

Chapter 5

Chen, L.-C., Wilson. R.H. Lloyd, W.R., and Mycek, M.-A. Error Analysis for Phasor Plots. (In preparation).

Chapter 6

Chen, L.-C.*, Chang, C.W., Esedoglu, S., and Mycek, M.-A. Novel Total Variation Image Denoising Improves Phasor Analysis of Time-Gated Fluorescence Lifetime Imaging Microscopy. *Authors contributed equally to this work. (In preparation).

7.2. Future directions

Future directions for further improvements or applications include the following:

1. For the label-free nonlinear optical molecular microscopy to assess tissue-engineered constructs:

Label-free nonlinear optical molecular imaging to assess implanted engineered tissues on animals

In Chapters 2 & 3, we showed that label-free nonlinear optical molecular imaging with quantitative analytic methods successfully differentiated controls from stressed constructs. Label-free nonlinear optical microscopy has the advantages such as high sensitivity, optical sectioning, providing second harmonic generation signals to isolate collagen, and deep tissue imaging, suitable for charactering tissues *in vitro*, *in situ*, and *in vivo*. In future studies, nonlinear optical molecular imaging will be employed to assess the viability of engineered tissues implanted into animals. Furthermore, the technique can be extended to a fiber-based hand-held device, enabling clinicians to select the healthiest engineered constructs pre-implantation and to assess the tissue viability post-implantation.

Tissue Assessments to study other models such as diabetes or cancer based on the tissue engineering model

In Chapter 4, rapamycin-cultured engineered tissues with a range of states of tissue viability were studied. Also performed was an experiment with various concentrations of calcium treatments (**Table 3.1**). The result shows that high calcium concentrations (*e.g.* 4mM) could cause cells to die. No normal cellular shape can be observed. Thus, the result

was not discussed. Other studies with different designed models will be noninvasively assessed by label-free nonlinear optical molecular imaging. A low redox ratio is expected from cancer cells as previously reported [57].

Quantitative comparison between optical measures and standard assays for cellular functionality

In Chapter 4, we showed that optical measures highly correlated to the cellular viability assay. The result was not surprising because optical measures monitored cellular metabolism and the standard viability assay monitored the mitochondrial activity, both assessing the cell functionality. In the future, optical measures will be carefully characterized and compared with standard functional assays. Quantitative immunofluorescence histology will be performed to account for the number of cells associated with the cell viability.

Determine diagnostic thresholds to define the manufacturing release criteria prior to human implantation

The development of label-free nonlinear optical microscopy is for the ultimate goal of defining a manufacture release criteria prior to human implantation. The studies so far have demonstrated its high reliability and high sensitivity, thus high potential of defining the release criteria. Quantitative thresholds will be defined based on these studies and more future studies to select the viable tissue-engineered constructs ready for human implantation.

2. For the extended phasor analysis algorithms:

Phasor uncertainty analysis of other biological samples and FLIM-FRET applications

In Chapter 5, phasor uncertainty analysis was applied for the complex biological system, tissue-engineered constructs. The algorithm will be applied for other biological samples. Furthermore, it will be applied to quantitatively monitor the FLIM-FRET trajectory, returning users with quantitative assessments of the donor-accepter energy transfer process.

Further characterization of the time-gated phasor plot map

In Chapter 6, time-gated phasor plot was developed to directly and rapidly interpret and visualize the time-gated FLIM images. As mentioned in the chapter, the time delay variable was not included in the phasor plot map due to its complexity. Further characterization of the variable will be performed. In addition, a new coordinate based on two axes, $g/\Delta t$ *and* g/τ, will be developed to provide FLIM users a more intuitive tool to interpret the FLIM images.

Phasor plot analysis for optical spectroscopy

Optical fluorescence spectroscopy was performed to assess the viability of engineered tissues implanted in mice. Measurements collected were analyzed by standard exponential fitting procedures. The collected data were analyzed by phasor plot analysis. Quantitative comparison between the results of fitting and phasor plot analysis and

between the *in vitro* and the *in vivo* results will be performed to assess the graft success post-implantation.

References

1. Mertz J. Introduction to optical microscopy: Roberts and Company Publishers, 2010.
2. Rossi AV, He XW, Tubino M. A simple, portable and low cost device for a colorimetric spot-test quantitative analysis. Anal Lett 2000;33(9):1885-1898.
3. Zinter JP, Levene MJ. Maximizing fluorescence collection efficiency in multiphoton microscopy. Optics Express 2011 Aug 1;19(16):15348-15362.
4. Willingham FF, Turner BG, Gee DW, Cizginer S, Sohn DK, Sylla P, et al. Leaks and endoscopic assessment of break of integrity after NOTES gastrotomy: the LEAKING study, a prospective, randomized, controlled trial. Gastrointest Endosc 2010;71(6):1018-1024.
5. Fu HL, Yu B, Lo JY, Palmer GM, Kuech TF, Ramanujam N. A low-cost, portable, and quantitative spectral imaging system for application to biological tissues. Optics Express 2010 Jun 7;18(12):12630-12645.
6. Leblond F, Davis SC, Valdes PA, Pogue BW. Pre-clinical whole-body fluorescence imaging: Review of instruments, methods and applications. J Photochem Photobiol B 2010 Jan 21;98(1):77-94.
7. Sun-Il C, AlAshmouny K, McCormick M, Yu-Chih C, Euisik Y. BioBolt: A minimally-invasive neural interface for wireless epidural recording by intra-skin communication. VLSI Circuits (VLSIC), 2011 Symposium on; 2011 15-17 June 2011; 2011. p. 146-147.
8. Graves EE, Weissleder R, Ntziachristos V. Fluorescence molecular imaging of small animal tumor models. Curr Mol Med 2004;4(4):419-430.
9. Skala MC, Riching KM, Bird DK, Gendron-Fitzpatrick A, Eickhoff J, Eliceiri KW, et al. *In vivo* multiphoton fluorescence lifetime imaging of protein-bound and free nicotinamide adenine dinucleotide in normal and precancerous epithelia. Journal of Biomedical Optics 2007;12(2):024014.
10. Chen LC, Lloyd WR, Kuo S, Kim HM, Marcelo CL, Feinberg SE, et al. Label-free nonlinear optical molecular microscopy non-invasively characterizes viability of engineered human tissue constructs. 2013, to submit.
11. Mulvey CS, Zhang K, Bobby Liu W-H, Waxman DJ, Bigio IJ. Wavelength-dependent backscattering measurements for quantitative monitoring of apoptosis, part 2: early spectral changes during apoptosis are linked to apoptotic volume decrease. Journal of Biomedical Optics 2011;16(11):117002.
12. Fujiwara M, Mizukami T, Suzuki A, Fukamizu H. Sentinel lymph node detection in skin cancer patients using real-time fluorescence navigation with indocyanine green: preliminary experience. Journal of plastic, reconstructive & aesthetic surgery : JPRAS 2009;62(10):e373-378.
13. Khmaladze A, Ganguly A, Kuo S, Raghavan M, Kainkaryam R, Cole JH, et al. Tissue-engineered constructs of human oral mucosa examined by Raman spectroscopy. Tissue engineering Part C, Methods 2013;19(4):299-306.
14. Chang C-W, Sud D, Mycek M-A. Fluorescence lifetime imaging microscopy. In: Sluder G, Wolf D, editors. Methods Cell Biol: Elsevier Inc, 2007.

15. Garlick JA, Taichman LB. Fate of human keratinocytes during reepithelialization in an organotypic culture model. Laboratory investigation; a journal of technical methods and pathology 1994;70(6):916-924.
16. Chang C-W, Wu M, Merajver SD, Mycek M-A. Improving FRET detection in living cells. Proc SPIE 2009;7370:737007.
17. Andriani F, Margulis A, Lin N, Griffey S, Garlick JA. Analysis of microenvironmental factors contributing to basement membrane assembly and normalized epidermal phenotype. Journal of investigative dermatology 2003;120(6):923-931.
18. Teuchner K, Freyer W, Leupold D, Volkmer A, Birch DJS, Altmeyer P, et al. Femtosecond Two-photon Excited Fluorescence of Melanin*. Photochem Photobiol 1999;70(2):146-151.
19. Wu YC, Qu JNY. Two-photon autofluorescence spectroscopy and second-harmonic generation of epithelial tissue. Optics Letters 2005 Nov 15;30(22):3045-3047.
20. Huang S, Heikal AA, Webb WW. Two-photon fluorescence spectroscopy and microscopy of NAD(P)H and flavoprotein. Biophysical journal 2002;82(5):2811-2825.
21. Chen LC, Lloyd WR, Kuo S, Marcelo CL, Feinberg SE, Mycek MA. Nonlinear optical molecular imaging enables metabolic redox sensing in tissue-engineered constructs. Proc Spie 2011;8089.
22. Chen LC, Lloyd WR, Kuo S, Marcelo CL, Feinberg SE, Mycek MA. Label-free multiphoton fluorescence imaging monitors metabolism in living primary human cells used for tissue engineering. Imaging, Manipulation, and Analysis of Biomolecules, Cells, and Tissues X 2012;Proc SPIE.
23. Chen L-C, Lloyd W, Chandra M, Izumi K, Kuo S, Marcelo C, et al. Optical redox imaging of endogenous contrast for tissue-engineered construct viability. 2011: Optical Society of America; 2011. p. OMC1.
24. Gareau DS, Bargo PR, Horton WA, Jacques SL. Confocal fluorescence spectroscopy of subcutaneous cartilage expressing green fluorescent protein versus cutaneous collagen autofluorescence. Journal of Biomedical Optics 2004 Mar-Apr;9(2):254-258.
25. Pena AM, Strupler M, Boulesteix T, Schanne-Klein MC. Spectroscopic analysis of keratin endogenous signal for skin multiphoton microscopy. Optics Express 2005 Aug 8;13(16):6268-6274.
26. Bayan C, Levitt JM, Miller E, Kaplan D, Georgakoudi I. Fully automated, quantitative, noninvasive assessment of collagen fiber content and organization in thick collagen gels. J Appl Phys 2009;105(10).
27. Plotnikov SV, Millard AC, Campagnola PJ, Mohler WA. Characterization of the myosin-based source for second-harmonic generation from muscle sarcomeres. Biophysical Journal 2006 Jan;90(2):693-703.
28. Nadiarnykh O, LaComb R, Campagnola PJ, Mohler WA. Coherent and incoherent SHG in fibrillar cellulose matrices. Optics Express 2007 Mar 19;15(6):3348-3360.
29. Rice WL, Firdous S, Gupta S, Hunter M, Foo CWP, Wang Y, et al. Non-invasive characterization of structure and morphology of silk fibroin biomaterials using non-linear microscopy. Biomaterials 2008 May;29(13):2015-2024.

30. Helmchen F, Denk W. Deep tissue two-photon microscopy. Nat Methods 2005 Dec;2(12):932-940.
31. Wagnieres G, Star W, Wilson B. *In vivo* fluorescence spectroscopy and imaging for oncological applications. Photochem Photobiol 1998;68(5):603-632.
32. Mycek M-A, Pogue BW, editors. Handbook of Biomedical Fluorescence. New York: Marcel Dekker, Inc., 2003.
33. Pena A, Strupler M, Boulesteix T, Godeau G, Schanne-Klein M-C. Spectroscopic analysis of keratin endogenous signal for skin multiphoton microscopy: erratum. Optics express 2005;13(17):6667.
34. Zipfel WR, Williams RM, Webb WW. Nonlinear magic: multiphoton microscopy in the biosciences. Nature Biotechnology 2003 Nov;21(11):1368-1376.
35. Heikal AA. Intracellular coenzymes as natural biomarkers for metabolic activities and mitochondrial anomalies. Biomark Med 2010 Apr;4(2):241-263.
36. Huang S, Heikal AA, Webb WW. Two-photon fluorescence spectroscopy and microscopy of NAD(P)H and flavoprotein. Biophys J 2002 May;82(5):2811-2825.
37. Chen LC, Lloyd WR, Chang CW, Sud D, Mycek MA. Fluorescence Lifetime Imaging Microscopy for Quantitative Biological Imaging. Method Cell Biol 2013;114:457-488.
38. Lakowicz JR. Principles of Fluorescence Spectroscopy. 3rd ed. New York: Springer, 2006.
39. Vishwanath K, Mycek M-A. Do fluorescence decays remitted from tissues accurately reflect intrinsic fluorophore lifetimes? Optics Letters 2004 July, 1, 2004;29(3):1512-1514.
40. Chorvat D, Chorvatova A. Multi-wavelength fluorescence lifetime spectroscopy: a new approach to the study of endogenous fluorescence in living cells and tissues. Laser Phys Lett 2009 Mar;6(3):175-193.
41. Lloyd W, Wilson RH, Chang C-W, Gillispie GD, Mycek M-A. Instrumentation to rapidly acquire fluorescence wavelength-time matrices of biological tissues. Biomedical Optics Express 2010;1(2):574-586.
42. Skala MC, Riching KM, Gendron-Fitzpatrick A, Eickhoff J, Eliceiri KW, White JG, et al. *In vivo* multiphoton microscopy of NADH and FAD redox states, fluorescence lifetimes, and cellular morphology in precancerous epithelia. Proc Natl Acad Sci USA 2007 Dec 4;104(49):19494-19499.
43. Benati E, Bellini V, Borsari S, Dunsby C, Ferrari C, French P, et al. Quantitative evaluation of healthy epidermis by means of multiphoton microscopy and fluorescence lifetime imaging microscopy. Skin Research and Technology 2011 Aug;17(3):295-303.
44. Provenzano PP, Eliceiri KW, Keely PJ. Multiphoton microscopy and fluorescence lifetime imaging microscopy (FLIM) to monitor metastasis and the tumor microenvironment. Clin Exp Metastasis 2009;26(4):357-370.
45. Lloyd WR, Chen L-C, Kuo S, Marcelo CL, Feinberg SE, Mycek M-A. Fluorescence lifetime imaging microscopy (FLIM) studies of living primary human cells for applications in tissue regeneration. In: Periasamy A, Konig K, So PTC, editors. SPIE Photonics West; 2012; San Francisco, California, USA: SPIE; 2012. p. 82260E-82266.
46. Lloyd WR, Chen L-C, Mycek MA. Fluorescence Spectroscopy. In: Morgan SP, Matcher SJ, Rose F, editors. Optical Techniques in Regenerative Medicine. CRC Press, 2013

47. Bugiel I, König K, Wabnitz H. Investigation of cell by fluorescence laser scanning microscopy with subnanosecond time resolution. Lasers in the Life Sciences 1989 1989;3(1):47-53.
48. Sharman KK, Periasamy A, Ashworth H, Demas JN, Snow NH. Error analysis of the rapid lifetime determination method for double-exponential decays and new windowing schemes. Anal Chem 1999;71(5):947-952.
49. Wang XF, Uchida T, Coleman DM, Minami S. A two-dimensional fluorescence lifetime imaging system using a gated image intensifier. Appl Spectrosc 1991;45(3):360-366.
50. Clayton AHA, Hanley QS, Verveer PJ. Graphical representation and multicomponent analysis of single-frequency fluorescence lifetime imaging microscopy data. Journal of microscopy 2004;213(Pt 1):1-5.
51. Redford GI, Clegg RM. Polar plot representation for frequency-domain analysis of fluorescence lifetimes. J Fluoresc 2005 Sep;15(5):805-815.
52. Digman MA, Caiolfa VR, Zamai M, Gratton E. The phasor approach to fluorescence lifetime imaging analysis. Biophysical Journal 2008;94(2):L14-L16
53. Vander Heiden MG, Cantley LC, Thompson CB. Understanding the Warburg effect: the metabolic requirements of cell proliferation. Science (New York, N Y) 2009;324(5930):1029-1033.
54. Avidor Y, Doherty MD, Olson JM, Kaplan NO. Fluorescence of Pyridine Nucleotides in Mitochondria. Journal of Biological Chemistry 1962;237(7):2377-&.
55. Klaidman LK, Leung AC, Adams JD, Jr. High-performance liquid chromatography analysis of oxidized and reduced pyridine dinucleotides in specific brain regions. Anal Biochem 1995 Jul 1;228(2):312-317.
56. Pitts J, Sloboda R, Dragnev K, Dmitrovsky E, Mycek M-A. Autofluorescence characteristics of immortalized and carcinogen-transformed human bronchial epithelial cells. Journal of Biomedical Optics 2001;6(1):31-40.
57. Ostrander JH, McMahon CM, Lem S, Millon SR, Brown JQ, Seewaldt VL, et al. Optical Redox Ratio Differentiates Breast Cancer Cell Lines Based on Estrogen Receptor Status. Cancer Research 2010 Jun 1;70(11):4759-4766.
58. Dela Cruz JM, McMullen JD, Williams RM, Zipfel WR. Feasibility of using multiphoton excited tissue autofluorescence for *in vivo* human histopathology. Biomed Opt Express 2010;1(5):1320-1330.
59. Fischer F, Volkmer B, Puschmann S, Greinert R, Breitbart W, Kiefer J, et al. Risk estimation of skin damage due to ultrashort pulsed, focused near-infrared laser irradiation at 800nm. Journal of Biomedical Optics 2008;13(4):041320-041320.
60. Balu M, Mazhar A, Hayakawa CK, Mittal R, Krasieva TB, Konig K, et al. *In vivo* multiphoton NADH fluorescence reveals depth-dependent keratinocyte metabolism in human skin. Biophysical journal 2013;104(1):258-267.
61. Konig K. Clinical multiphoton FLIM tomography. Multiphoton Microscopy in the Biomedical Sciences Xii 2012;8226.
62. Koehler MJ, Vogel T, Elsner P, Konig K, Buckle R, Kaatz M. *In vivo* measurement of the human epidermal thickness in different localizations by multiphoton laser tomography. Skin Research and Technology 2010 Aug;16(3):259-264.

63. Weinigel M, Breunig HG, Fischer P, Kellner-Hofer M, Buckle R, Konig K. Compact clinical high-NA multiphoton endoscopy. Endoscopic Microscopy Vii 2012;8217.
64. König K. Clinical multiphoton tomography. J Biophotonics 2008;1(1):13-23.
65. Jung T, Hohn A, Grune T. Lipofuscin: detection and quantification by microscopic techniques. Methods in molecular biology (Clifton, N J) 2010;594:173-193.
66. Izumi K, Song J, Feinberg SE. Development of a tissue-engineered human oral mucosa: from the bench to the bed side. Cells Tissues Organs 2004;176(1-3):134-152.
67. Haycock JW. 3D cell culture: a review of current approaches and techniques. Methods in molecular biology (Clifton, N J) 2011;695:1-15.
68. Wang BG, Konig K, Halbhuber KJ. Two-photon microscopy of deep intravital tissues and its merits in clinical research. Journal of microscopy 2010;238(1):1-20.
69. Scanlon CS, Van Tubergen EA, Chen LC, Elahi SF, Kuo SH, Feinberg S, et al. Characterization of squamous cell carcinoma in an organotypic culture via subsurface non-linear optical molecular imaging. Experimental Biology and Medicine 2013 Nov;238(11):1233-1241.
70. Levitt JM, Hunter M, Mujat C, McLaughlin-Drubin M, Munger K, Georgakoudi I. Diagnostic cellular organization features extracted from autofluorescence images. Optics Letters 2007 Nov 15;32(22):3305-3307.
71. Izumi K, Feinberg SE, Iida A, Yoshizawa M. Intraoral grafting of an *ex vivo* produced oral mucosa equivalent: a preliminary report. Int J Oral Maxillofac Surg 2003 Apr;32(2):188-197.
72. Izumi K, Neiva RF, Feinberg SE. Intraoral Grafting of Tissue-Engineered Human Oral Mucosa. Oral & Craniofacial Tissue Engineering 2011(No. 2):9.
73. Fitzmaurice GM, Laird NM, Ware JH. Applied Longitudinal Analysis, 2nd Edition: John Wiley & Sons, 2011.
74. Wu YC, Xi P, Qu JAY, Cheung TH, Yu MY. Depth-resolved fluorescence spectroscopy reveals layered structure of tissue. Optics Express 2004 Jul 12;12(14):3218-3223.
75. Hotta T, Yokoo S, Terashi H, Komori T. Clinical and histopathological analysis of healing process of intraoral reconstruction with ex vivo produced oral mucosa equivalent. Kobe J Med Sci 2007;53(1-2):1-14.
76. Gouyet J-F. Physics and fractal structures. New York, NY, USA: Springer-Verlag, 1996.
77. Stringari C, Nourse JL, Flanagan LA, Gratton E. Phasor Fluorescence Lifetime Microscopy of Free and Protein-Bound NADH Reveals Neural Stem Cell Differentiation Potential. PLoS One 2012 Nov 5;7(11).
78. Berthiaume F, Maguire TJ, Yarmush ML. Tissue engineering and regenerative medicine: history, progress, and challenges. Annu Rev Chem Biomol Eng 2011;2:403-430.
79. Novosel EC, Kleinhans C, Kluger PJ. Vascularization is the key challenge in tissue engineering. Adv Drug Deliv Rev 2011 Apr 30;63(4-5):300-311.
80. Fisher MB, Mauck RL. Tissue engineering and regenerative medicine: recent innovations and the transition to translation. Tissue Eng Part B Rev 2013 Feb;19(1):1-13.

81. Izumi K, Feinberg SE, Terashi H, Marcelo CL. Evaluation of transplanted tissue-engineered oral mucosa equivalents in severe combined immunodeficient mice. Tissue Eng 2003 Feb;9(1):163-174.
82. Lloyd WR, Lee SY, Elahi SF, Chen L-C, Kuo S, Kim HM, et al. Assessment of post-implantation tissue-engineered graft success by diffuse reflectance spectroscopy. in preparation.
83. Chandra M, Vishwanath K, Fichter GD, Liao E, Hollister SJ, Mycek M-A. Quantitative molecular sensing in biological tissues: an approach to non-invasive optical characterization. Optics Express 2006;14(13):6157-6171.
84. Dittmar R, Potier E, van Zandvoort M, Ito K. Assessment of cell viability in three-dimensional scaffolds using cellular auto-fluorescence. Tissue engineering Part C, Methods 2012;18(3):198-204.
85. Georgakoudi I, Rice WL, Hronik-Tupaj M, Kaplan DL. Optical spectroscopy and imaging for the noninvasive evaluation of engineered tissues. Tissue Eng Part B Rev 2008 Dec;14(4):321-340.
86. Lloyd WR, Chen L-C, Wilson RH, Mycek M-A. Biophotonics: Clinical Fluorescence Spectroscopy and Imaging. In: Moore JE, Maitland DJ, editors. Biomedical Technology and Devices Handbook, Second Edition, 2013.
87. Appel AA, Anastasio MA, Larson JC, Brey EM. Imaging challenges in biomaterials and tissue engineering. Biomaterials 2013;34(28):6615-6630.
88. Yang J, Yamato M, Shimizu T, Sekine H, Ohashi K, Kanzaki M, et al. Reconstruction of functional tissues with cell sheet engineering. Biomaterials 2007;28(34):5033-5043.
89. Izumi K, Inoki K, Fujimori Y, Marcelo CL, Feinberg SE. Pharmacological retention of oral mucosa progenitor/stem cells. J Dent Res 2009;88(12):1113-1118.
90. Chen L-C, Lloyd, W.R., Kuo, S., Kim, H.M., Marcelo, C.L., Feinberg, S.E., and Mycek, M.-A. Nonlinear optical molecular microscopy characterizes tissue-engineered constructs and assesses local viability. . (submitted).
91. Hill NE. Dielectric Properties and Molecular Behaviour. London; New York: Van Nostrand Reinhold, 1969.
92. Stringari C, Cinquin A, Cinquin O, Digman MA, Donovan PJ, Gratton E. Phasor approach to fluorescence lifetime microscopy distinguishes different metabolic states of germ cells in a live tissue. P Natl Acad Sci USA 2011;108(33):13582-13587.
93. Stringari C, Edwards RA, Pate KT, Waterman ML, Donovan PJ, Gratton E. Metabolic trajectory of cellular differentiation in small intestine by Phasor Fluorescence Lifetime Microscopy of NADH. Sci Rep-Uk 2012 Aug 10;2.
94. Wright BK, Andrews LM, Markham J, Jones MR, Stringari C, Digman MA, et al. NADH Distribution in Live Progenitor Stem Cells by Phasor-Fluorescence Lifetime Image Microscopy. Biophysical Journal 2012 Jul 3;103(1):L07-L09.
95. Stringari C, Sierra R, Donovan PJ, Grafton E. Label-free separation of human embryonic stem cells and their differentiating progenies by phasor fluorescence lifetime microscopy. Journal of Biomedical Optics 2012 Apr;17(4).
96. Schlachter S, Schwedler S, Esposito A, Schierle GSK, Moggridge GD, Kaminski CF. A method to unmix multiple fluorophores in microscopy images with minimal a priori information. Optics Express 2009 Dec 7;17(25):22747-22760.

97. Xu Z, Raghavan M, Hall TL, Chang CW, Mycek MA, Fowlkes JB, et al. High speed imaging of bubble clouds generated in pulsed ultrasound cavitational therapy-histotripsy. Ieee Transactions on Ultrasonics Ferroelectrics and Frequency Control 2007 Oct;54(10):2091-2101.
98. Zhong W, Wu M, Chang CW, Merrick KA, Merajver SD, Mycek MA. Picosecond-resolution fluorescence lifetime imaging microscopy: a useful tool for sensing molecular interactions *in vivo* via FRET. Optics Express 2007 Dec 24;15(26):18220-18235.
99. Chang CW, Mycek MA. Total variation versus wavelet-based methods for image denoising in fluorescence lifetime imaging microscopy. J Biophotonics 2012 May;5(5-6):449-457.
100. Chang C-W, Mycek M-A. Precise fluorophore lifetime mapping in live-cell, multi-photon excitation microscopy. Optics Express 2010;18(8):8688-8696.
101. Chang CW, Mycek MA. Enhancing precision in time-domain fluorescence lifetime imaging. Journal of Biomedical Optics 2010 Sep-Oct;15(5).
102. Chang C-W, Mycek MA. Enhancing precision in time-domain fluorescence lifetime imaging. J Biomed Opt 2010;15(5):056013.
103. Fereidouni F, Esposito A, Blab GA, Gerritsen HC. A modified phasor approach for analyzing time-gated fluorescence lifetime images. Journal of Microscopy 2011 Dec;244(3):248-258.
104. Urayama P, Zhong W, Beamish JA, Minn FK, Sloboda RD, Dragnev KH, et al. A UV-visible-NIR fluorescence lifetime imaging microscope for laser-based biological sensing with picosecond resolution. Appl Phys B-Lasers O 2003 May;76(5):483-496.
105. Lin HJ, Herman P, Lakowicz JR. Fluorescence lifetime-resolved pH imaging of living cells. Cytometry Part A 2003 Apr;52A(2):77-89.
106. Nakabayashi T, Wang HP, Tsujimoto K, Miyauchi S, Kamo N, Ohta N. A correlation between pH and fluorescence lifetime of 2',7'-Bis(2-carboxyethyl)-5(6)-carboxyfluorescein (BCECF) *in vivo* and *in vitro*. Chemistry Letters 2007 Feb 5;36(2):206-207.